MEMOIRS

OF THE

FACULTY OF ENGINEERING

OSAKA CITY UNIVERSITY

VOL. 62

DECEMBER 2021

This series of Memoirs is issued annually. Selected original works of the members of the Faculty of Engineering are compiled in the first part of the volume. Abstracts of papers presented elsewhere during the current year are compiled in the second part. List of conference presentations delivered during the same period is appended in the last part.

All communications with respect to Memoirs should be addressed to:

MEMOIRS OF THE FACULTY OF ENGINEERING
OSAKA CITY UNIVERSITY

CONTENTS

Abstracts of Papers Published in Other Journals ······· 21

List of Presentations at International Conferences ······· 75

MEMOIRS

OF THE

FACULTY OF ENGINEERING

OSAKA CITY UNIVERSITY

_____

VOL. 62

_____

DECEMBER 2021

Overview of Storage Batteries for Battery Electric Vehicles: Present and Future Beyond Lithium-Ion Batteries

Shota ITO* and Kingo ARIYOSHI**

Synopsis

The battery electric vehicle (BEV), which uses a storage battery as a power source, requires high-performance lithium-ion batteries (LIBs) because the driving characteristics of BEV depend on battery performance. In this study, the theoretical energy density of LIBs was calculated from a scientific point of view. In addition, the energy density of practical LIBs was estimated from an engineering point of view. The dependence of BEV performance with respect to the mileage per charge on the battery energy was discussed based on the specifications of BEVs that are currently available on the market. Finally, next-generation storage batteries that are currently being researched and developed were compared with respect to battery performance required for BEVs.

KEYWORDS: Lithium-ion battery, Battery electric vehicle, Mileage per energy, Next-generation batteries

1. Introduction

In recent years, electric vehicles (EVs) have received considerable attention because they contribute to climate change mitigation when coupled with decarbonized electricity. The EVs can be divided into the following types: 1) hybrid electric vehicles (HEVs), which use two power sources, that is, petroleum fuels and batteries; 2) plug-in hybrid electric vehicles (PHEV), which use two power sources but mainly batteries with larger capacities than HEVs; and 3) battery electric vehicles (BEVs), which exclusively use batteries as power sources.[1,2] Among these different types of EVs, only BEVs, which do not use gasoline, have zero emissions.

Based on the use of high-energy density lithium-ion batteries (LIBs) as power sources, high-performance BEVs could be realized in recent years. The mileage of BEVs, which depends on the energy of the storage battery, can be significantly increased by installing a high-energy density LIB. The use of LIBs also improves the driving performance of the BEV depending on the power capability of the storage battery. However, because the energy density of LIBs is significantly lower than that of gasoline fuel, the mileage of BEVs is smaller than that of gasoline-powered vehicles. In addition, in contrast to an internal combustion engine that can easily supply fuel, charging of LIBs takes a considerable amount of time, resulting in reduction in the daily travel distance. Therefore, the development of BEVs depends on the development of storage batteries.

In this study, we provide an overview of current LIBs from scientific and engineering viewpoints. We calculated the theoretical energy density of LIBs based on the electrochemical properties of the electrode materials and estimated the practical energy density of LIBs by considering inactive battery materials. Subsequently, the correlation between the battery performance and BEV mileage based on the specifications of commercially available EVs was determined. Finally, we briefly surveyed next-generation storage batteries that are currently being researched and developed as power sources for BEVs.

---

* Student, Master Course of Department of Urban Engineering
** Associate Professor, Department of Applied Chemistry and Bioengineering

2. Theoretical Energy Density of Lithium-Ion Batteries

The theoretical energy density of LIBs can be calculated from the electrode potentials and reversible capacities of active materials used for the positive and negative electrodes. Because the theoretical energy density does not consider any components constituting the battery, such as the current collector, separator, or electrolyte solution, it corresponds to the limiting value of the energy density in LIBs. After an overview of the electrochemical properties of active materials that are currently being studied, the theoretical energy densities of various LIBs are discussed.
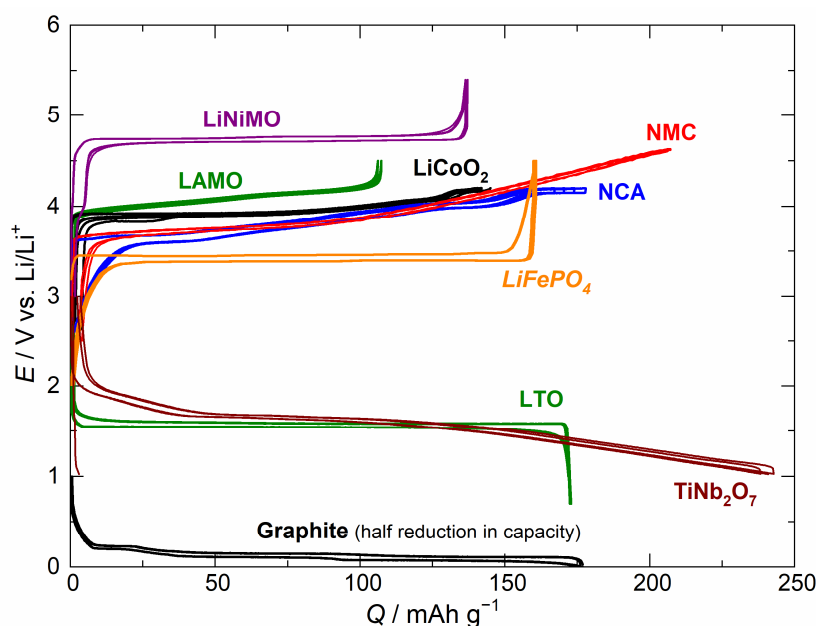
Fig. 1 Charge-discharge curves of electrode materials used for lithium-ion batteries.

Table 1.   Properties of various electrode materials used for lithium-ion batteries.

Electrode Materials	d/g cm^{-3}	E/V	Q_{gra}/mAh g^{-1}	Q_{vol}/mAh cm^{-3}
LiCoO$_2$ (LCO)	5.06	3.8	150	760
LiCo$_{1/3}$Ni$_{1/3}$Mn$_{1/3}$O$_2$ (NMC)	4.78	3.7	160	765
LiNi$_{0.8}$Co$_{0.15}$Al$_{0.05}$O$_2$ (NCA)	4.75	3.7	180	855
Li[Li$_{0.1}$Al$_{0.1}$Mn$_{1.8}$]O$_4$ (LAMO)	4.16	4.0	100	415
Li[Ni$_{1/2}$Mn$_{3/2}$]O$_4$ (LiNiMO)	4.45	4.7	130	580
LiFePO$_4$ (LFP)	3.60	3.6	160	575
Graphite (GR)	2.27	0.1	350	795
Li[Li$_{1/3}$Ti$_{5/3}$]O$_4$ (LTO)	3.48	1.6	170	590
TiNb$_2$O$_7$ (TNO)	4.29	1.5	230	985

Figure 1 shows the charge–discharge curves of various electrode materials, which were examined in an electrochemical cell with a Li metal electrode. The charge–discharge curves were used to estimate the average potential and reversible capacity per weight and volume of each electrode material (Table 1).[3-6)] The reversible capacity per volume was calculated using the following equation:

$$Q_{vol}\ [\text{mAh cm}^{-3}] = Q_{gra}\ [\text{mAh g}^{-1}] \times d\ [\text{g cm}^{-3}],$$

where d is the density estimated from the unit cell volume obtained from the XRD measurements (called XRD density). Among the various types of electrode materials used for LIBs, material with an electrode potential of <3 V and >3 V is generally used as a negative and positive electrode, respectively.

Because the electrode potential of graphite (GR) is the lowest among the materials, most of the current LIBs use graphite as the negative electrode. $Li[Li_{1/3}Ti_{5/3}]O_4$ (LTO) is a material with a long life. It is known as zero-strain material and has a higher electrode potential than GR (1.6 V), which is disadvantageous in terms of the energy density. However, owing to its high electrode potential, Li-metal deposition is not a concern, facilitating high-rate charging and a high safety. $TiNb_2O_7$ (TNO) has a higher capacity than LTO but similar electrode potential.

Lithium cobalt oxide ($LiCoO_2$: LCO) is widely used as a positive electrode in LIBs. However, because Co is expensive, it is not suitable for large-scale LIBs. Lithium nickel oxide ($LiNi_{0.8}Co_{0.15}Al_{0.05}O_2$: NCA) is used in LIBs for BEV applications because it is cheaper and has a higher capacity than LCO. The $LiCo_xNi_yMn_zO_2$ (NCM; $x + y + z = 1$) has an excellent cyclability and thermal stability. Lithium iron phosphate ($LiFePO_4$: LFP) has a low potential, which is disadvantageous in terms of energy density, but it has excellent thermal stability. Lithium manganese oxide ($Li[Li_{0.1}Al_{0.1}Mn_{1.8}]O_4$; LAMO) has a spinel structure with a three-dimensional framework, resulting in an excellent structural and thermal stability. $Li[Ni_{1/2}Mn_{3/2}]O_4$ (LiNiMO) in which a part of Mn is replaced with Ni is a 5 V positive electrode material.

The energy density of LIBs depends on the product of operating voltage and reversible capacity. The operating voltage of LIBs can be calculated from the potential difference between the positive and negative electrodes. Therefore, the electrode potential of high-voltage LIBs should be high and low for positive and negative electrodes, respectively. The GR/LiNiMO, which is a combination of the GR negative electrode with the lowest electrode potential and the LiNiMO positive electrode with the highest electrode potential, exhibits the highest operating voltage of 5 V, which is 1 V higher than that of the current GR/LCO. LIBs with LTO or TNO have low operating voltages because of the high electrode potentials of these materials (~1.5 V). Even when these negative electrodes are combined with LiNiMO, which is the positive electrode with the highest electrode potential, the battery voltage is only 3 V, that is, 1 V lower than that of GR/LCO.

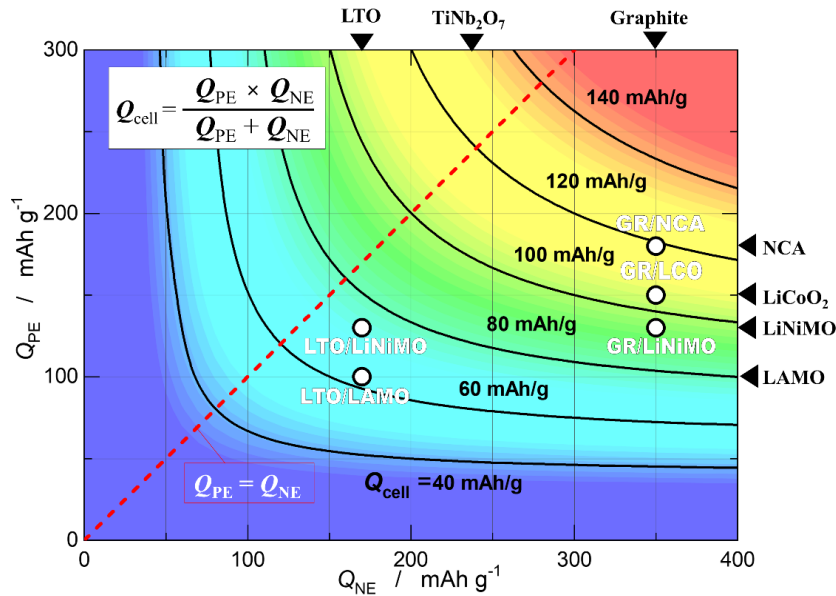Fig. 2 Cell capacity (Q_{cell}) calculated from the capacities of the positive and negative electrode materials (Q_{PE} and Q_{NE}). The Q_{cell} was calculated using the following equation: $Q_{cell} = Q_{PE} \times Q_{NE}/(Q_{PE} + Q_{NE})$.

The capacity of the LIB (Q_{cell}) was calculated using the following equation:

$$1/Q_{cell} = 1/Q_{PE} + 1/Q_{NE},$$

where Q_{PE} and Q_{NE} are the reversible capacities of the positive and negative electrodes, respectively. Figure 2 shows the capacities of various LIBs and the dependence of Q_{cell} on Q_{PE} and Q_{NE}. The capacity of LIBs increases with the reversible capacity of the electrode material. The GR/NCA has the largest capacity, which is ~10% larger than that of the current GR/LCO. When an LTO negative electrode is used, the battery capacity decreases. The capacity of LTO/LAMO is 50% that of GR/LCO.

Based on the capacity dependence of Q_{cell}, the capacity ratio between the positive and negative electrodes is optimal for the same values of Q_{PE} and Q_{NE}. This means that Q_{cell} will increase insignificantly even if the capacity of either electrode becomes extremely large. For example, the battery capacities of LTO/LAMO and GR/LAMO differ by only 30%, although the capacities of the negative electrodes differ by two fold (350 mAh g^{-1} for GR vs. 170 mAh g^{-1} for LTO). An increase in the Q_{PE} leads to an increase in the capacity of the LIB with a GR negative electrode because the reversible capacity of the GR negative electrode is two-fold higher than that of the positive electrode. Based on the capacity ratio of Q_{PE} and Q_{NE}, the application of a silicon negative electrode with an extremely large capacity (>3000 mAh g^{-1}) slightly improves the battery capacity.
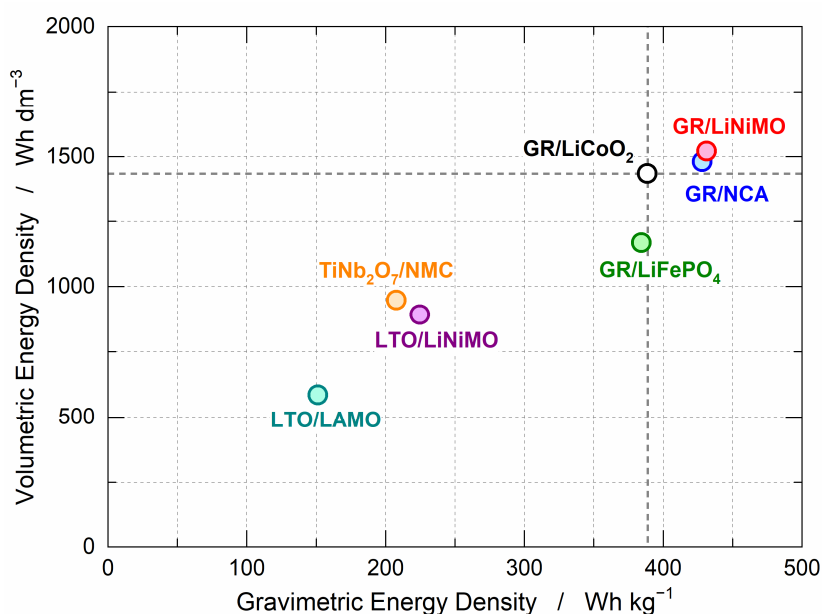
Fig. 3 Gravimetric and volumetric energy densities of lithium-ion batteries. Both energy densities were calculated from the parameters of the electrode materials listed in Table 1.

Figure 3 shows the theoretical energy densities per weight and volume, that is, ε_{gra} [Wh kg^{-1}] and ε_{vol} [Wh dm^{-1}], of various LIBs. To design high-energy density LIBs, electrode materials with high capacities and large potential differences must be combined. For example, the combination of a GR negative electrode with high-voltage LiNiMO or high-capacity NCA leads to high-voltage or high-capacity LIBs, which have a higher energy density than the current GR/LCO. Because the oxide negative electrodes of LTO and TNO have higher potentials and smaller capacities than the GR negative electrodes, LIBs using an oxide negative electrode are not very attractive from the viewpoint of the energy density. However, the oxide negative electrode has several advantages such as an excellent cyclability, no risk of Li metal deposition, and high-rate charging. Therefore, LIBs with a high power capability, long life, and high reliability could potentially be used in applications other than high-energy density batteries.

3. Practical Energy Density of Lithium-Ion Batteries and Mileage of Battery Electric Vehicles

The practical energy density of LIBs is much lower than the theoretical energy density because practical LIBs consist of components other than active materials such as the current collector, separator, electrolyte, and outer case (Fig. 4a).[7] Aluminum and copper foils are used as the current collector on the positive and negative electrodes, respectively. Copper metal is stable, with no alloying reaction with Li^+, which is why heavy Cu metal is used as a current collector for the GR negative electrode. Placing the separator between the positive and negative electrodes prevents a short circuit. The electrolyte is impregnated into the pores of the electrodes and separator. Metal plates or laminated films are used for the outer case to prevent moisture from entering the cell.
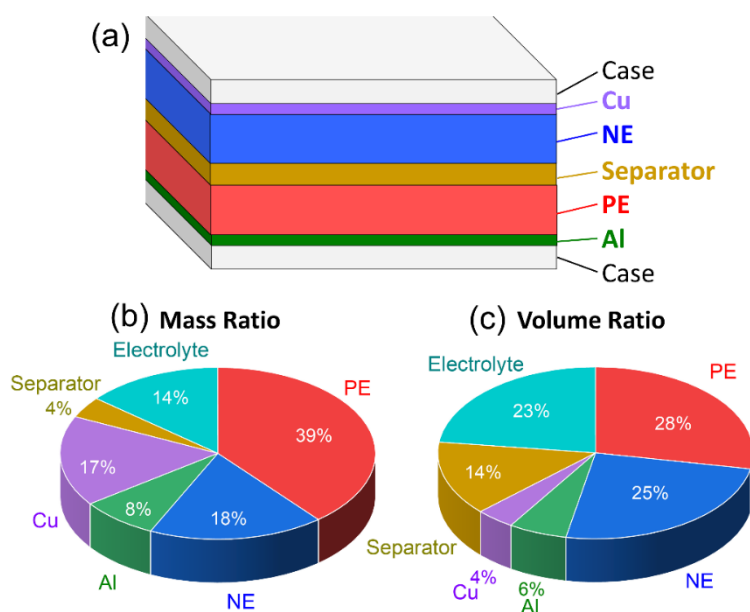

Fig. 4 (a) Schematic illustration of lithium-ion batteries consisting of a positive electrode (PE), negative electrode (NE), separator, Al and Cu current collectors, and outer case. (b) Mass and (c) volume ratio of each component of lithium-ion batteries.

The pie charts in Figs 4b and c show examples of the mass and volume ratios of each component in the LIB. The Cu and electrolytes account for a large proportion of the battery weight. The combined volume of the separator and electrolyte is 40% of the battery volume, although the amount of electrolyte in LIBs can be minimized. The weight and volume ratio of the active material in the practical LIBs is 50-60%, which results in the reduction of the practical energy density of LIBs to half of the theoretical energy density. In LIBs for high-power applications, the electrode is thinner and sparser. Therefore, the amounts of the current collector and the separator further increases, leading to a reduction in the practical energy density of the battery. For LIBs for BEV applications, which require energy density rather than power density, thicker and denser electrodes are more appropriate because of the increased practical energy density.[8]

Figure 5 illustrates the cell capacity and energy density per volume of commercially available LIBs. The energy density of coin-type batteries with a cell capacity below 0.1 Ah is ~200 Wh dm^{-3}. The energy density increases with the increase in cell capacity based on the increased battery size because increasing the battery size reduces the relative proportion of the outer case. The LIBs with a cell capacity of ~3 Ah reach the highest energy density of 600 Wh dm^{-3}. These LIBs are used in smartphones and laptop computers. When the cell capacity increases further (>10 Ah), the energy density decreases drastically. Because it is difficult to increase

the single-cell capacity by simply increasing the single-cell size, large-capacity LIBs contain a large number of small-capacity single cells that are connected in series and in parallel. To avoid heat generation issues, the practical energy density is reduced by using a cooling system inside the battery module.[9] This means that it is important to develop a battery system from an engineering point of view and optimize the cell design and size to improve the practical energy density of LIBs rather than developing electrode materials.
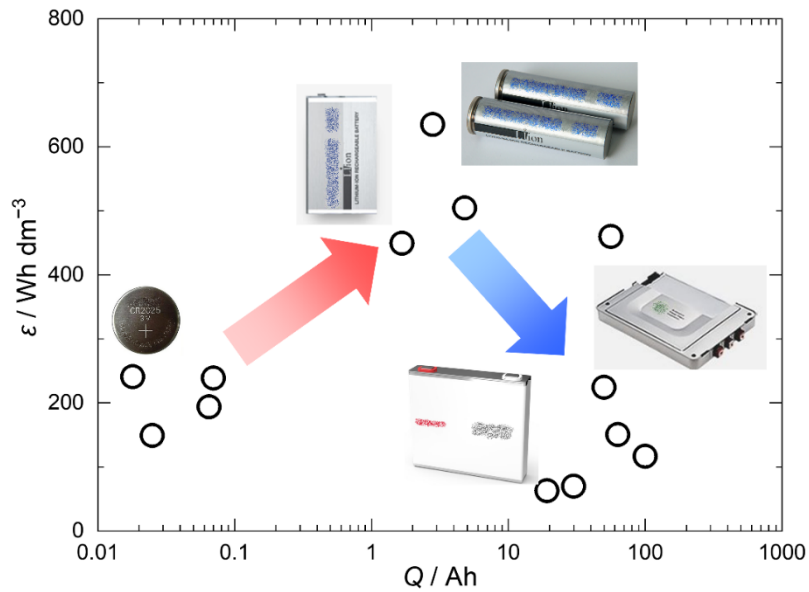

Fig. 5 Volumetric energy density of commercial lithium-ion batteries as a function of the battery capacity.
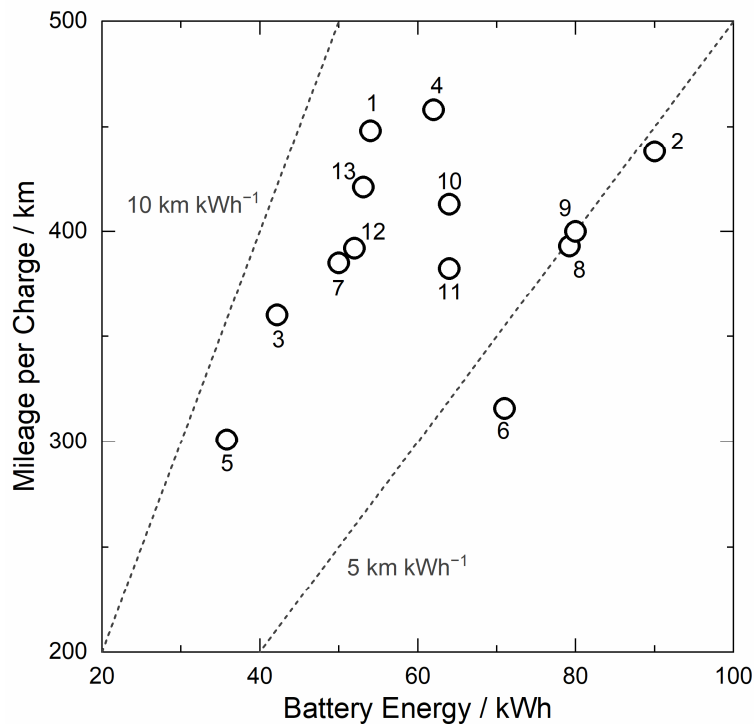
Fig. 6 Plots of the mileage per charge of battery electric vehicles versus the energy of the battery installed in the electric vehicle. The numbers indicate the electric vehicles listed in Table 2.

Table 2. Battery electric vehicles available on global markets.

No.	Manufacturer	Model	Mileage/km	Battery Energy/kWh
1	Tesla	Model 3	448	54
2	Jaguar	I-PACE	438	90
3	BMW	I3	360	42
4	Nissan	Leaf	458	62
5	VW	E-Golf	164	16
6	Audi	e-tron	301	36
7	Peugeot	e-208	316	71
8	Porsche	Taycan	385	50
9	Mercedes-Benz	EQC 400	393	79
10	Hyundai	Kona	400	80
11	Kia	Niro	413	64
12	Renault	ZOE	382	64
13	BYD	Qin Pro	392	52

Figure 6 shows the correlation between the mileage per charge that can be traveled on a single charge of the BEVs and the energy of the installed LIB. Most BEVs can travel more than 300 km on a single charge and the mileage of some vehicles exceeds 400 km. The energy efficiency of BEVs, which is defined as the mileage in kilometers per 1 kWh of the battery energy, is 5 to 10 km kWh^{-1}. The smaller the vehicle weight is, the higher is the energy efficiency of the BEV (Fig. 7). The energy consumption of BEVs is inversely proportional to the vehicle weight, which is slightly larger than 10 km kWh^{-1} t^{-1}. Therefore, the reduction in BEV weight is an important and effective way to improve the energy efficiency.

Fig. 7 Mileage per battery energy for electric vehicles as a function of the vehicle weight. The numbers indicate the electric vehicles listed in Table 2.

During the past decade, BEVs have been developed to extend the mileage to the same level as that of gasoline-powered vehicles. However, BEVs are more suitable for the use in urban areas with heavy traffic,

characterized by frequent acceleration and deceleration. Therefore, BEVs will mainly be used for small transportation in the city based on ride and car sharing, rather than long-distance transportation, which gasoline vehicles 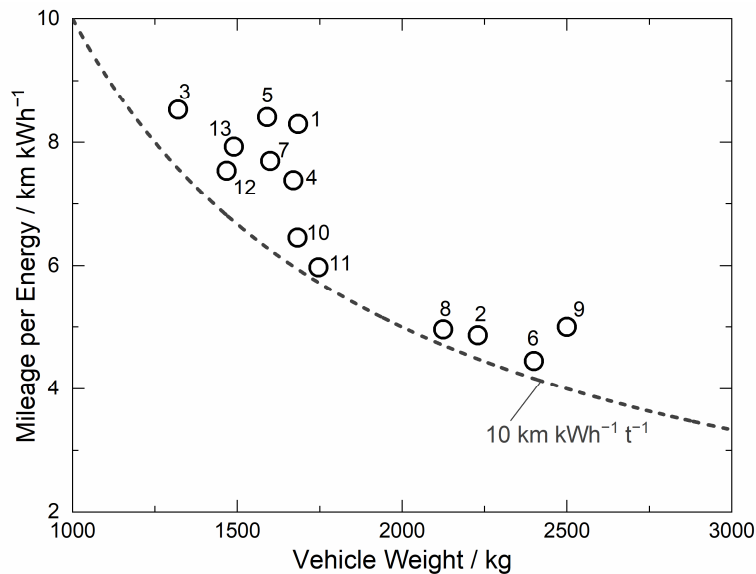are used for. Taxis and minibuses, for example, are considered to be suitable applications for BEVs. Because the daily mileage of taxis in Japan is ~140 km,[10] current BEVs with a mileage of 300 km can be operated as taxis. Therefore, it is important to develop BEVs and focus on shortening the charging time, lifespan, and price rather than increasing the mileage.

4. Next-Generation Storage Batteries for Battery Electric Vehicles

Table 3 shows the target values for the battery performance of BEVs in each country/region in 2015.[11] There are few differences in the storage battery performances of BEVs in each country/region. Below, we discuss the correlations between each target value and BEV performance.

Table 3.　Target values of battery performances for BEVs.

	Japan	USA	EU	China
ε_{gra}/Wh kg^{-1}	250	235	200–300	200
ε_{vol}/Wh dm^{-3}	300	500	300–500	-
P_{gra}/W kg^{-1}	1,500	2,000	-	2,000
P_{vol}/W dm^{-3}	1,800	1,000	-	-
Calendar Life/year	10–15	15	10	10–15
Cycle Life	1,000–1,500	1,000	3,000	2,000–3,000
Cost/¥ kWh^{-1}	15,000	13,500	20,000	26,000

-**Gravimetric energy density (ε_{gra})**: The value of ε_{gra} is closely related to the mileage per charge. Batteries with a large ε_{gra} value lead to the extension of the mileage without increasing the weight of the battery installed in the BEV. If the ε_{gra} value is small, the energy efficiency of the BEV is low because heavy LIBs must be installed in the BEV.

-**Volumetric energy density (ε_{vol})**: The ε_{vol} value determines the volume occupied by the storage battery in the BEV and does not affect the mileage per charge. However, a small ε_{vol} value results in limited space in the BEV; therefore, a high ε_{vol} value is required for the BEV application.

-**Power density (P_{gra} & P_{vol})**: The output power density controls the acceleration performance of the BEV, whereas the input power density affects the charging time and efficiency of the regenerative energy. Because the battery energy of a BEV is very large, the power density does not need to be as high as that of an HEV. Therefore, the rate capability of storage batteries for BEVs is thought to be sufficient in a 2 C-rate on discharging and 4 C-rate on charging.

-**Life**: The BEVs are expected to be used for at least ten years. The number of cycles should be ~1,000. If the vehicle is operated every day, the battery life will be reached in three years. Therefore, the lifespan of ten years represents the calendar life, assuming a light user who drives only on weekends.

-**Cost**: Based on battery cost of 15,000 ¥ kWh^{-1}, it costs ¥ 750,000 for a 50 kWh battery, which is one of the reasons why BEVs are more expensive than gasoline-powered vehicles. Therefore, each country has introduced subsidies to popularize BEVs.

-**Safety/reliability**: The safety/reliability of the battery performance is not listed in the table because it is difficult to quantitatively evaluate it. However, storage batteries for BEVs require a high safety and reliability. Because BEVs are equipped with many batteries, it is necessary to avoid situations in which the battery energy

is released at once (short-circuit conditions). In addition, because the BEV requires a high voltage (~200 V), several cells are connected in series. This means that when a single cell becomes unusable, the entire battery system cannot be used.
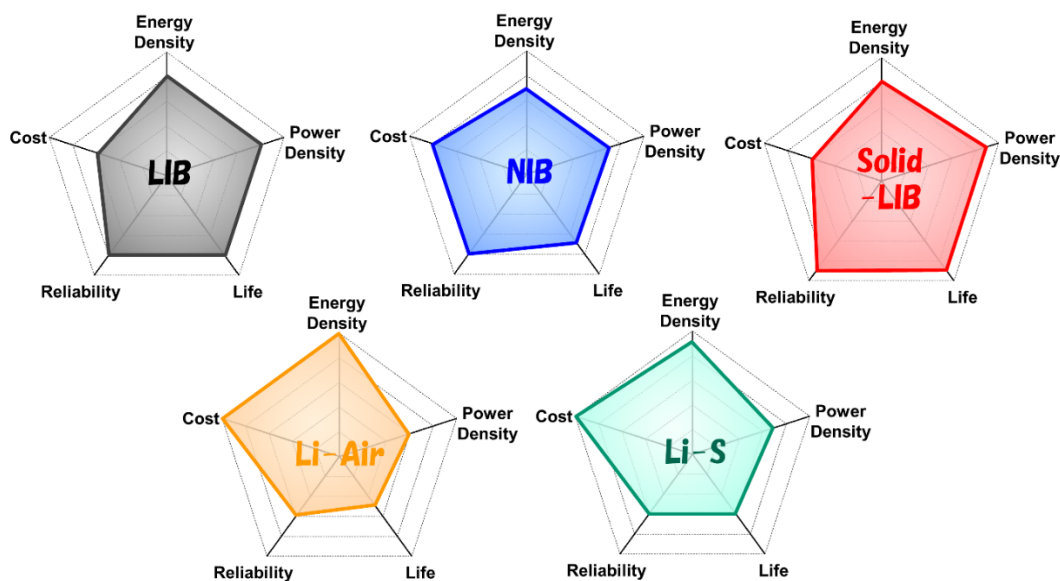

Fig. 8 Various performances of storage batteries used for BEVs; lithium-ion batteries (LIB), sodium-ion batteries (NIB), all-solid-state lithium-ion batteries (Solid-LIB), Li–air batteries (Li-Air), and Li–sulfur batteries (Li-S).

To assess whether next-generation storage batteries can achieve the battery performance required for BEVs, the energy density, power density, life, reliability, cost, and performances of storage batteries that are currently being researched and developed are shown in Fig. 8. The shape of the chart represents the characteristics of each battery, as discussed below.

LIB:[12] The LIBs are currently the most widely used high-energy density storage batteries. The LIBs have been developed and improved for 30 years and are now reaching high levels from a technological viewpoint. In other words, the space for improvement of the performance of LIBs is insufficient unless a dramatic breakthrough is made. Consequently, a dramatic improvement in the performance of LIBs in the near future cannot be expected.

-Sodium-ion battery (NIB):[13] The NIBs are based on the same principle as LIBs because Li ions in LIBs are replaced with Na ions in NIBs. Because Na ions have a larger atomic weight and larger ionic radius than Li ions, the energy density of NIBs does not exceed that of LIBs. The advantage of NIBs is their costs; they are cheaper than LIBs. In addition, Na is very abundant compared with Li, which is advantageous for BEVs that require a large capacity.

-Lithium–air battery (Li-Air):[14,15] The Li metal has a high capacity (3860 mAh g^{-1}) and the lowest potential among metal electrodes. In Li-Air batteries, oxygen is used as the active material of the positive electrode and the capacity of the positive electrode in unlimited because it can be replenished by the atmosphere. Consequently, the theoretical energy density of Li-Air is high, that is, >10,000 Wh kg^{-1} based on the theoretical battery voltage of 2.96 V. Li-Air batteries have to overcome crucial problems; the Li metal electrode must be used safely and the cathode electrode of the fuel cell must be reversible.

-Lithium–sulfur battery (Li-S):[16] The Li-S batteries in which the positive electrode in Li-Air is replaced with sulfur have an operating voltage of 2 V, which is ~50% lower than that of LIBs. However, the theoretical

energy density of Li-S is very high because the theoretical capacity of the sulfur positive electrode is very large (1675 mAh g^{-1}). The costs of Li-S batteries are very low because sulfur is inexpensive. The crucial problem is that the lifetime is limited by the dissolution of sulfur during cycling.

-All-solid-state battery (Solid-LIB):[17,18] The Solid-LIBs employ a solid electrolyte instead of a liquid electrolyte. In conventional LIBs, a Li salt is dissolved in an organic solvent. Although the ionic conductivity of the solid electrolyte is lower than that of the liquid electrolyte, the power density of Solid-LIBs is superior to that of liquid-LIBs. One of the most important advantages of Solid-LIBs is the safety. The Solid-LIBs are expected to be safer than liquid-LIBs because they do not use a flammable organic electrolyte. In addition, the life cycle of Solid-LIBs is not limited because of the high chemical and electrochemical stability of the solid electrolyte, given the stability issue of the interface in the active material/solid electrolyte is solved.

Based on the overview of these next-generation storage batteries, batteries have been extensively studied due to their low cost and high abundance, except for Solid-LIBs. The results suggest that the material cost and abundance are the most important factors affecting BEV applications. In addition, the fact that the use of Li-S and Li-Air can dramatically improve the energy density also led to numerous studies. However, these two storage batteries still have many technical problems and the demonstration stage has not been reached. Compared with Li-Air and Li-S batteries, the battery technology of NIBs is established because they are based on the same principle as LIBs. Although several NIBs are being considered for practical use, a battery performance similar to that of LIBs has not yet been achieved. The Solid-LIB is considered to be the most suitable storage battery for BEVs because it is safe; however, it requires the development of novel technology for the application of solid electrolytes, which is completely different from conventional liquid-LIBs. Therefore, LIBs will still account for the majority of BEV power sources for the next decade and research and development regarding the safety and longevity of LIBs will continue.

5. Conclusion

In this paper, we provide an overview of storage batteries (particularly LIBs), which are the main devices of BEVs, from theoretical and practical viewpoints. The theoretical energy density of LIBs was calculated from the electrochemical properties of the electrode materials. The results indicate that progress with respect to new materials is indispensable for improving the theoretical energy density of LIBs. The practical energy density of LIBs estimated based on considering battery components other than the electrode materials is much lower than the theoretical one and greatly varies depending on the battery size. Particularly, in large LIBs for BEVs, the actual energy density is significantly decreased to ensure safety. This indicates that applied research and technological development from an engineering point of view are important for improving the practical energy density of LIBs.

The mileage of BEVs that are currently on the market is closely related to the battery energy and exceeds 300 km. The mileage per energy corresponding to the energy efficiency of BEVs ranges from to 5–10 km kWh^{-1} and depends on the vehicle weight, that is, ~10 km Wh^{-1} t^{-1}. The performance of current BEVs is sufficient for urban transportation. If BEVs are limited to the use in urban transportation, the battery performance required for LIBs will be more important in terms of the life characteristics and cost than the energy density.

Finally, we compared the battery performance of next-generation storage batteries that are currently being researched and discussed their adaptability as a power source for BEVs. Although most of the batteries are superior to LIBs in terms of the energy density and cost, the lifetime and safety remain concerns because of the lack of reliable data obtained from practical battery systems. To move the next-generation storage batteries from the research stage to the development stage, it is necessary to develop battery designs and technologies that provide high safety and long life. The verification of the battery system for BEVs requires a long time;

therefore, it is important to improve the current LIBs of BEVs with respect to extending the lifetime and reducing the cost, including the recycling process.

References

1) A. Emadi, Y. J. Lee, and K. Rajashekara, Power electronics and motor drives in electric, hybrid electric, and plug-in hybrid electric vehicles, *IEEE Trans. Ind. Electron*., **55**, 2237-2245 (2008).

2) M. Ehsani, Y. Gao, S. Longo, and K. M. Ebrahimi, Modern electric, hybrid electric, and fuel cell vehicles, *CRC Press* (2018).

3) M. S. Whittingham, Lithium batteries and cathode materials, *Chem. Rev*., **104**, 4271-4301 (2004).

4) J. B. Goodenough and Y. Kim, Challenges for rechargeable Li batteries, *Chem. Mater*., **22**, 587-603 (2010).

5) T. Ohzuku, K. Ariyoshi, Y. Makimura, N. Yabuuchi, and K. Sawai, Materials strategy for advanced lithium-ion (shuttlecock) batteries: lithium nickel manganese oxides with or without cobalt, *Electrochemistry*, **73**, 2-11 (2005).

6) J. M. Tarascon, and M. Armand, Issues and challenges facing rechargeable lithium batteries, *Nature*, **414**, 359-367 (2001).

7) J. Betz, G. Bieker, P. Meister, T. Placke, M. Winter, and R. Schmuch, Theoretical versus practical energy: A plea for more transparency in the energy calculation of different rechargeable battery systems, *Adv. Energy Mater*., **9**, 1803170 (2019).

8) Y. Kuang, C. Chen, D. Kirsch, and L. Hu, Thick electrode batteries: Principles, opportunities, and challenges, *Adv. Energy Mater*., **9**, 1901457 (2019).

9) J. Deng, C. Bae, J. Marcicki, A. Masias, and T. Miller, Safety modelling and testing of lithium-ion batteries in electrified vehicles, *Nat. Energy*, **3**, 261-266 (2018).

10) Annual statistical report on motor vehicle transport, Ministry of Land, Infrastructure, Transport and Tourism (2019).

11) TSC foresights, vol. 5, NEDO, Japan (2015).

12) G. E. Blomgren, The development and future of lithium ion batteries, *J. Electrochem. Soc*., **164**, A5019-A5025 (2017).

13) N. Yabuuchi, K. Kubota, M. Dahbi, and S. Komaba, Research development on sodium-ion batteries, *Chem. Rev*., **114**, 11636-11682 (2014).

14) W. J. Kwak, Rosy, D. Sharon, C. Xia, H. Kim, L. R. Johnson, P. G. Bruce, L. F. Nazar, Y. K. Sun, A. A. Frimer, M. Noked, S. A. Freunberger, and D. Aurbach, Lithium-oxygen batteries and related systems: Potential, status, and future, *Chem. Rev*., **120**, 6626-6683 (2020).

15) T. Liu, J. P. Vivek, E. W. Zhao, J. Lei, N. Garcia-Araez, and C. P. Grey, Current challenges and routes forward for nonaqueous lithium-air batteries, *Chem. Rev*., **120**, 6558-6625 (2020).

16) A. Rosenman, E. Markevich, G. Salitra, D. Aurbach, A. Garsuch, and F. F. Chesneau, Review on Li-sulfur battery systems: an integral perspective, *Adv. Energy Mater*., **5**, 1500212 (2015).

17) K. Takada, Progress and prospective of solid-state lithium batteries, *Acta Mater*., **61**, 759-770 (2013).

18) C. Sun, J. Liu, Y. Gong, D. P. Wilkinson, and J. Zhang, Recent advances in all-solid-state rechargeable lithium batteries, *Nano Energy*, **33**, 363-386 (2017).

Changes in Commuting Travel Behavior Focusing on the Role of Shared Transportation in the Wake of the COVID-19 Pandemic and the Tokyo Olympics

Weilin YE* and Nagahiro YOSHIDA**

Abstract

In order to sustain life in the face of coronavirus infection 2019 (COVID-19), people's lifestyles and travel behaviors have to change. Accordingly, such changes are occurring in travel behavior for commuting purposes, especially during periods of heavy congestion. In addition, with the recent development of the sharing economy, the introduction of shared transportation is rapidly expanding in the transportation sector, which may contribute to alleviating traffic congestion and other problems under COVID-19 conditions. In this study, we focused on the changes in travel behavior for commuting purposes during COVID-19, which includes the period of the Tokyo Olympics when traffic congestion is expected. The survey was conducted using a web-based questionnaire. In order to further promote changes in travel behavior during COVID-19, we also analyzed the possibility of changes in the use of passenger transportation resulting from the nudge effect of information provision and incentives.

KEYWORDS: COVID-19, shared transportation, nudge, public benefit

1. Research Background and Objectives

In response to the COVID-19 pandemic, four states of emergency were declared between April 2020 and July 2021, three Cs "closed spaces, crowded places, and close-contact settings" infection control measures were announced, and new work styles (telework, telecommuting, and staggered work hours) were implemented. In addition, the Tokyo Olympics held in August 2021 and the traffic congestion caused by the implementation of transportation demand management measures had a significant impact on people's daily travel behavior especially for commuting purposes. Thus, under the situation where three C's avoidance behavior is required, shared transportation is rapidly introduced as one of the new transportation modes, and its use has been increasing in recent years. Thus, although the use of shared transportation is increasing, its role in transportation planning remains unclear.

Regarding research related to transportation behavior, on top of the mobility management strategies, the use of nudges is advancing not only in the research area of human behavior change, but also in the consideration of concrete proposals in public policy. Nudge is a theory postulated by Richard H. Thaler, who was awarded the Nobel Prize in Economics in 2017, and it is defined as "a policy approach that helps people to voluntarily make better choices for themselves" using behavioral science findings (behavioral insights) [1]. In the field of transportation behavior, there is a need for policies that help people to voluntarily make better choices while avoiding infection and congestion, and it is necessary to focus on the role of shared transportation as a new transportation option and to examine the possibility of promoting its use.

Commuting traffic behavior is generally influenced by time (morning rush hour), space (work location, residence, etc.), and personal attributes, but is said to be more difficult to transform than other trips. In other words, the transformation of commuting transportation behavior is considered to be a long-term change. Therefore, the purpose of this study is to focus on the changes in transportation behavior for commuting purposes during the COVID-19 period and the Tokyo Olympics, when traffic congestion on roads or overcrowding in public transportation systems was expected. We conducted a survey using a web-based questionnaire. In addition, to further promote the change in transportation behavior during the COVID-19 period, this research is novel in that it examines the intention to use and recommend the public, environmental, and financial incentives of shared transportation, and the change in transportation behavior using nudges. The novelty lies in the point of transformation (promotion of use) using nudges. In the field of urban transportation planning, clarifying the role of shared transportation in sanitation and traffic congestion situations is significant toward reducing traffic congestion in future transportation planning.

The shared transportation considered in this study includes car share, bike share, and kickboard share.

---

* Student, Master Course of Department of Civil Engineering
** Associate Professor, Department of Civil Engineering

2. Research methodology
2.1. Situation of the target site

The Tokyo Metropolitan Government declared a state of emergencies on April 7, 2020; January 7, 2021; April 23, 2021; July 12, 2021; and August 2, 2021; to prevent the spread of COVID-19 [2].The number of infected people in Tokyo peaked around January 2021, and it spread again in May. By July, the number of infected people increased daily.

Regarding the status of shared transportation in Tokyo, there are several companies providing bike-sharing services, all of which are private companies [3] and receive parking space support from different departments of local government. Of these, only one company operates in the city center, and mutual use is possible in 11 wards. As of the end of March 2021, approximately 870 site ports and 9,200 bicycles have been installed. As for car share [4], as of the end of March 2021, the six major companies (Times Car, Careco, ORIX CarShare, Cariteco, Honda Every Go, and Earth Car) had 17,987 stations and 34,887 vehicles. Among them, the number of stations in Tokyo was 6,741, and the number of vehicles was 12,778. Kickboard Sharing system [43] is a new type of shared transportation, which will be introduced in Tokyo and Osaka in April 2021, in which 200 ports are ready for kickboard use.

During COVID-19, to combat infection and reduce congestion, public transportation adjusted its weekday schedule through telework and staggered work hours, road transportation promoted the use of bicycles, and shared transportation suspended some ports. To reduce congestion during the Olympic Games, public transportation will be operated safely and smoothly as in COVID-19, and road transportation were asked to reduce and disperse travel demand during the Games period through Traffic Demand Management (TDM) including measures providing dedicated lanes or priority lanes for the Games and tolling measures (toll surcharges, half-price discounts at night, etc.). [5] [6]

2.2 Survey overview

The questionnaire survey was conducted through a web-based survey to understand the actual status of changes in commuter transportation behavior and the attitudes and behaviors of commuters. As shown in Table 1, we asked about transportation mode, cost, and time; for the risks and perceptions of COVID-19, we asked about risk avoidance measures and attitudes, and for shared transportation, we asked about awareness, usage, and evaluation.

The plan with nudges consisted of four questions on the intention to use and recommendation (Table 2). Among them, Plan 4 was set only for financial incentives and was a required item. Plans 1, 2, and 3 were combined plans for financial incentives, public benefits, and environmental awareness, and subjects were randomly asked about them.

Table 1. Survey overview

Survey method	Web-based questionnaire survey
Survey Period	July 28, 2021 - August 1, 2021
Survey target	Workers in their 20s to 60s in central Tokyo (1000 samples)
Target area	Chiyoda, Chuo, Minato, Shinjuku, Bunkyo, Shinagawa, Meguro, Koto, Shibuya, and Nakano wards
Main survey items	Personal attributes: gender/age/household composition/ownership of means of transportation and license status/commuting allowance/annual income/place of residence/area of work/occupation/industry Commuting transportation behavior: content of change and reason for change/ mode of transportation and its commuting time before and after change/ transportation cost before and after change/frequency of going out for commuting purposes Covid-19: Awareness of Covid-19 (possibility of infection) / Behavior with Covid-19 (implementation of countermeasures) Shared transportation: Awareness /Time spent using transportation / Frequency of use / Reasons for not using transportation / Evaluation

Table 2. Nudge Plan Contents

Plan	Contents
Plan 1	Environmental awareness: Points awarded based on CO2 reduction (financial incentive)
Plan 2	Public benefit: Points awarded based on the degree of congestion avoidance (financial incentive)
Plan 3	Environmental awareness: Points awarded based on CO2 reduction (financial incentive)
	Public benefit: Points awarded based on the degree of congestion avoidance (financial incentive)
Plan 4	Points awarded based on distance used (financial incentive)

3. Analysis of survey results
3.1 Actual changes in transportation behavior for commuting purposes

The percentage increase and decrease before and after the change in means of transportation by reason are shown in Figure 1. The means of transportation that increased during the "Olympic only" change were buses, cars (with passengers), and bicycles, in that order, and it is thought that the means of transportation changed due to the traffic restrictions on the roads during the Olympic Games. On the other hand, the means of transportation that increased during the "COVID-19 only" change were bicycles, bike share, and cabs. In the case of "COVID-19 only," the increased means of transportation were bicycles, bike share, and taxis, while the decreased means of transportation whose use decreased were public transportation such as "rail/train" and "bus."

Figure 2 shows the changes before and after the combination of transportation modes. The combination of public transportation only and walking + public transportation decreased. The combination of public transportation and individual transportation has increased. The use of shared transportation has increased. Note that (2) public transportation is represented by rail/train and bus (3) individual transportation is represented by car (private car), car (passenger), cab, Motorcycle e and bicycle (private car) (4) shared transportation is represented by Bike Share, Car Share and Kickboard Share.
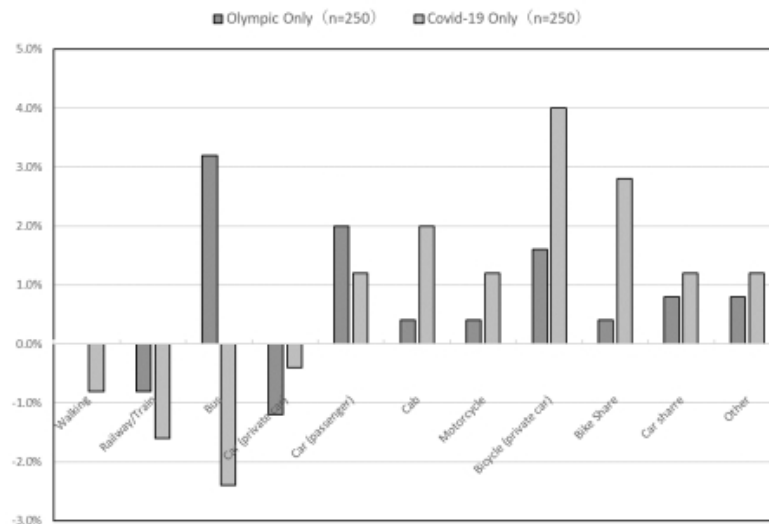

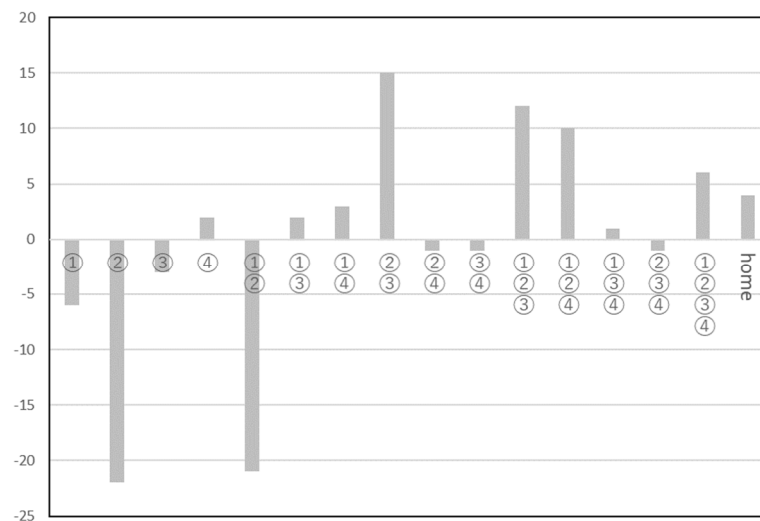Fig.1.Percentage increase or decrease before and after change in means of transportation by reason

Fig.2.Change before and after combining transportation methods (n=750)

Table 4 shows the results of the regression analysis on the main factors affecting commuting time. Case 1 shows the results of the analysis on the impact of the reason for the change and the details of the change on

the commuting time. As for Changed reason the commuting time for "Olympic only" became shorter, and " Olympic+COVID-19" became longer. As for the place of residence, it can be seen that commuting time becomes longer for those who live farther away. In terms of changes, changes in the means of transportation have the greatest impact on commuting time. As for the contents of changed behavior, all have an impact on commuting time, with transportation means having the greatest impact. Case 2 shows the impact on commuting time for those whose means of transportation has changed. As for the means of transportation, commuting time is longer for "Car (Driver) " and " Motorcycle ", and for Shared transportation, " Bike Share" has no effect on commute times, while" Car Share" affects commuting times, and using" Car Share" increases commute times. And "Kickboard Share" will make the commute less time consuming.

Table 4. Results of multiple regression analysis on factors affecting commuting time

		Case 1 (Pooled)				Case 2(where only the means of transportation was changed)			
		coefficient	Std. error	t -value		coefficient	Std. error	t -value	
Constants		4.609	0.123	37.534	**	1.997	0.340	5.873	**
Changed reason (dummy)	Not changed (Reference)	-							
	Olympic	-0.535	0.221	-2.424	*				
	COVID-19	0.320	0.218	1.468					
	Olympic+COVID-19	0.624	0.221	2.819	**				
Residence (dummy)	Tokyo (Reference)	-				-			
	Saitama Prefecture	1.828	0.321	5.691	**	1.110	0.592	1.874	
	Chiba Prefecture	0.829	0.310	2.676	**	-0.234	0.646	-0.363	
	Kanagawa Prefecture	1.811	0.261	6.940	**	1.252	0.450	2.782	**
Contents of changed behavior (dummy)	Not Changed	-							
	Origin or Destination	0.527	0.160	3.285	**				
	Means of Transportation	1.268	0.177	7.161	**				
	Routes	0.469	0.200	2.341	*				
Means of transportation (dummy)	Walking					1.913	0.279	6.852	**
	Train/train					2.034	0.331	6.150	**
	Bus					1.876	0.317	5.922	**
	Car (Driver)					2.420	0.361	6.712	**
	Car (Passenger)					0.875	0.564	1.551	
	Cab					1.037	0.481	2.158	*
	Motorcycle					2.271	0.622	3.649	**
	Bicycle					1.517	0.388	3.908	**
	Bike Share					0.763	0.485	1.574	
	Car Share					1.528	0.666	2.294	*
	Kickboard Share					-3.177	0.867	-3.665	**
R				0.308				0.719	
Adjusted R2				0.090				0.501	
F-value				20.307	**			32.364	**
Sample number				1750				438	

*p<.05 **p<.01

Table 5 shows the results of multiple regression analysis on factors affecting transportation costs. Case 1 shows the results of the analysis on the impact of the reason for the change and the details of the change on the change on the transportation cost. As for the reason for the change, the transportation cost was relatively higher for those who chose " Olympic only". As for the place of residence, the transportation cost was higher for those who lived farther away. Regarding the Contents of changed behavior, the transportation cost was relatively higher for all the behavior. Case 2 shows the results of the impact on transportation costs due to changes in the means of transportation of those who changed. As can be seen, transportation cost increases for those who chose "Bus ", " Car (Driver)", " Motorcycle ", and " Bicycle". In Shared transportation, those who chose "Car Share" spent the most on transportation, and " Bike Share" has no effect on transportation costs.

Table 5. Results of Multiple Regression Analysis on Factors Affecting Transportation Costs

		Case 1 (Pooled)				Case 2(where only the means of transportation was changed)			
		coefficient	Std. error	t -value		coefficient	Std. error	t -value	
Constants		1.957	0.071	27.743	**	2.052	0.226	9.074	**
Changed reason (dummy)	Not changed (Reference)	-							
	Olympic	0.406	0.127	3.204	**				
	COVID-19	-0.210	0.125	-1.675					
	Olympic+COVID-19	0.099	0.127	0.776					
Residence (dummy)	Tokyo (Reference)	-				-			
	Saitama Prefecture	0.748	0.184	4.057	**	0.967	0.394	2.455	*
	Chiba Prefecture	0.883	0.178	4.962	**	-0.101	0.429	-0.235	
	Kanagawa Prefecture	1.083	0.150	7.231	**	1.128	0.299	3.768	**
Contents of changed behavior (dummy)	Not Changed	-							
	Origin or Destination	0.546	0.092	5.923	**				
	Means of Transportation	0.406	0.102	3.998	**				
	Routes	0.253	0.115	2.200	*				
Means of transportation (dummy)	Walking					0.006	0.186	0.030	
	Train/train					0.225	0.220	1.023	
	Bus					0.515	0.211	2.445	*
	Car (Driver)					1.083	0.240	4.514	**
	Car (Passenger)					0.375	0.375	1.001	
	Cab					0.058	0.320	0.182	
	Motorcycle					1.294	0.414	3.126	**
	Bicycle					-0.701	0.258	-2.715	**
	Bike Share					-0.329	0.322	-1.021	
	Car Share					2.027	0.443	4.579	**
	Kickboard Share					-0.096	0.577	-0.167	
R				0.288				0.507	
Adjusted R2				0.078				0.232	
F-value				17.469	**			10.440	**
Sample number				1750				438	

*p<.05 **p<.01

3.2 Awareness of risk and the impact of travel behavior on commuting purposes

This section discusses the impact of risk avoidance measures and attitudes on travel behavior for commuting purposes on the risk perception of COVID-19. Figure 3 shows Situations where people avoid crowded places. The left section shows the percentage of places avoided in the "with change" category was slightly higher than in the "no change" category. One of the more significant differences is that the "with change" places more emphasis on the environment in which they are moving: indoor pathways and outdoor sidewalks. This may be one of the reasons for the changes in behavior. The right section shows "COVID-19 only" placed more importance on the crowdedness of indoor places such as restaurants and shopping malls, which may be the reason for the change in behavior.
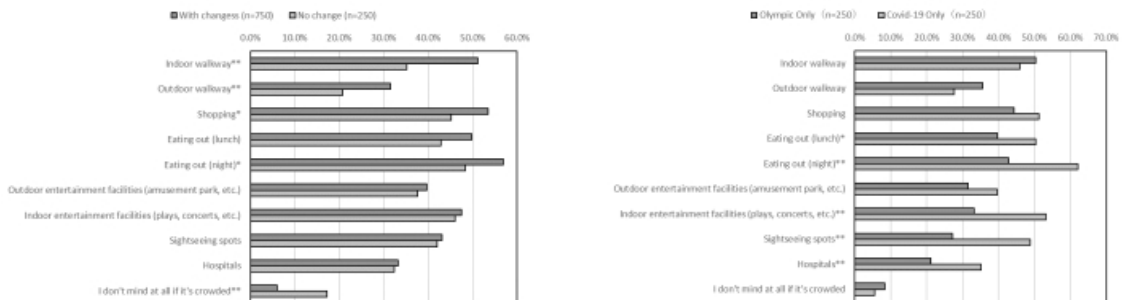
*p<.05 **p<.01

Fig.3. Situations where people avoid crowded places: Left; Change or not, Right; By reason for change

As can be seen from the table 6, there is a difference in the perception of risk depending on the mode of transportation. There was a large difference in risk perception between rail/train users and shared transportation users.

Table 6. Risk perception aggregation results: shared transportation and other modes (*p<.05 **p<.01)

Transportation	Bike Share(n=48)		Car share(n=23)		Kickboard share(n=16)	
	t-value		t-value		t-value	
Rail / Train(n=794)	3.088	**	2.983	**	0.036	
Bus(n=132)	1.207		1.978		-0.324	
Car (private) (n=86)	0.043		1.214		-0.608	
Car (passenger) (n=44)	-0.293		0.792		-0.71	
Cab(n=42)	-1.633		-0.04		-1.145	
Motorcycle(n=31)	-0.034		0.937		-0.605	
Bicycle (private) (n=98)	2.139	*	2.577	*	-0.022	

3.3 Shared transportation perceptions and roles for commuting purposes

In terms of frequency of use, car share users were most likely to use it 3-4 days a week (52%), while bike share users were most likely to use it for "10-30 minutes or less" (52%). A comparison of awareness of shared transportation and experience of changing transportation behavior showed that awareness of shared transportation was high, with a difference of about 40%.

Figure 4 compares the differences in evaluations between bike share and car share. The evaluation of bike share was better than that of car share in terms of convenience of use (ports, time of use, etc.), public nature (easing traffic congestion), and environmental friendliness. There are fewer traffic restrictions and congestion related to bike share, and they can be used more freely. On the other hand, car share was rated better than bike share in terms of economic efficiency (purchase cost, maintenance cost, and pricing plans). This could be because the cost of a car is higher than that of a bike.
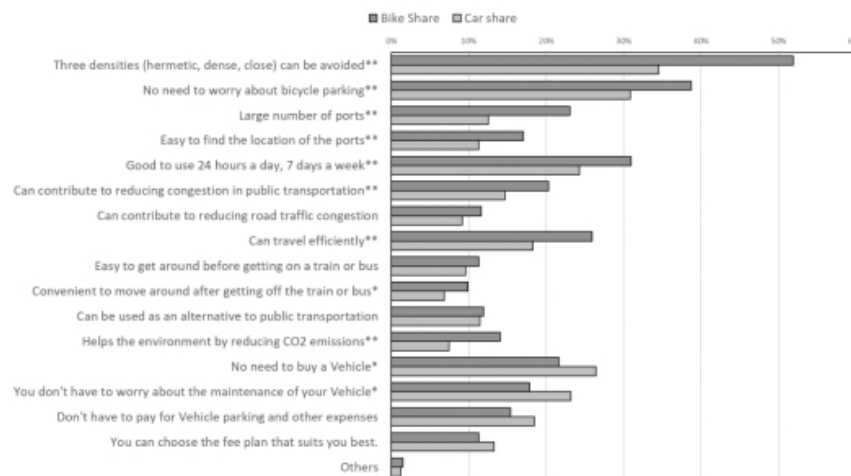

Fig.4. Evaluation of bike share and car share (multiple responses) (*p<.05 **p<.01)

3.4 Plan Considerations with Nudges

Figure 5 shows the intention to use and recommendation of the shared transportation type according to whether they have experienced it. There is a significant difference between the intention to use and the intention to recommend between experienced and inexperienced users. The presentation of financial incentives in the form of versatile points will also be effective in promoting the use of shared transportation. For inexperienced users, use should be encouraged after increasing the penetration rate. For example, information such as the fact that using shared transportation in COVID-19 can be avoided to "Three Cs" and that it can be avoided in traffic congestion situations during commuting can be given to inexperienced users.

Figure 6 shows the results of intention to use and recommendation between those with high-risk perception and those with low-risk perception. It shows that there is a significant difference between the intention to use and recommend shared transportation between those with high and low awareness of Plan 1

and Plan3. There is no significant difference between the four plans for high-risk perception people, suggesting that they are more responsive to the incentives offered. Those with low-risk perception have a clear intention to use Plan 1, and Plan 3 having the lowest intention to use.
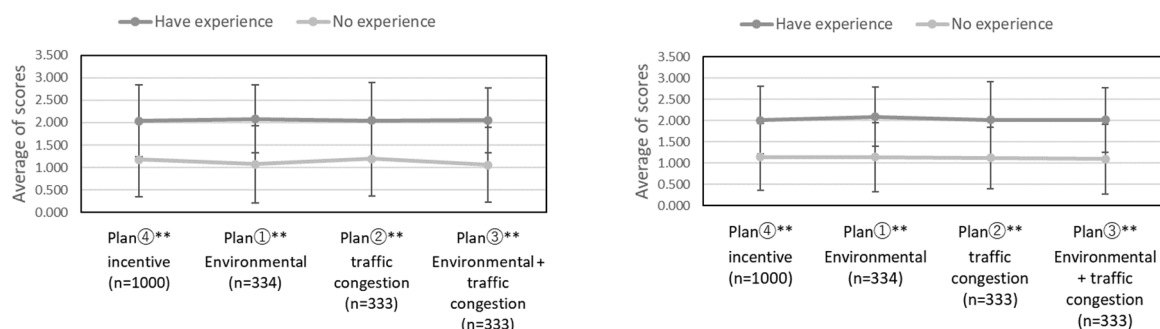

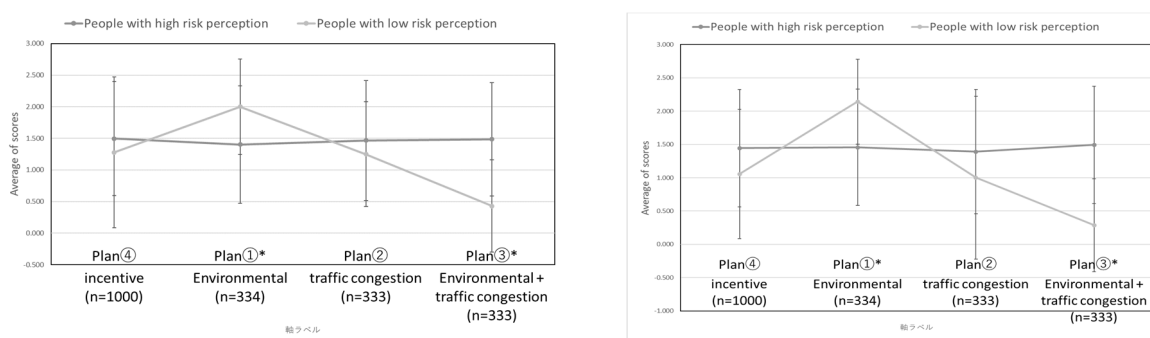Fig.5. Experienced or not: Left; Intention to use, Right; Intention to recommend (*p<.05 **p<.01)

Fig.6. Risk perception: Left; Intention to use, Right; Intention to recommend (*p<.05 **p<.01)

4. Conclusions

Change or not lead to a change between different means of transportation; the use of public transportation tends to decrease, and the commuting time tends to change to longer. Differences in risk perception lead to changes in commuter transportation behavior. There is a difference in the perception of shared transportation depending on whether the user has used it before or not, and it was found that there are still issues of dissemination and convenience. The role of shared transportation for commuting purposes can be considered in terms of safety, economy, environment, and public nature. People respond to the provision of financial incentives, and it is possible to encourage the use of shared transportation by providing them appropriately.

Further study needs to consider changes in attitudes depending on the vaccination status and changes in Covid-19 after the Olympics. As for the plan using nudges, a plan for those who have not experienced shared transportation is necessary due to the decreasing popularity. Plans for shared transportation publicity (traffic congestion reduction) need to be more specific.

References

1) Japanese version of Nudge Unit (BEST): http://www.env.go.jp/earth/ondanka/nudge.html, (Viewed on May 24, 2021). HP.
2) N.H.K. COVID, 19 Special site HP: https://www3.nhk.or.jp/news/special/coronavirus/, (Viewed on May 24, 2021).
3) Bureau of Environment. Tokyo Metropolitan Government., Bicycle sharing HP: https://www.kankyo.metro.tokyo.lg.jp/vehicle/management/bycicle_sharing/index.html, (Viewed on May 24, 2021).
4) Car sharing comparison 360°: https://www.carsharing360.com/, (Viewed on May 24, 2021). HP.
5) Ministry of Land, Infrastructure, Transport and Tourism, Immediate Road Measures to Cope with the New Normal HP: https://www.mlit.go.jp/report/press/road01_hh_001332.html(Viewed on July 20, 2021).
6) Tokyo 2020, Organizing Committee: Traffic Measures During the Games HP: https://olympics.com/tokyo-2020/ja/games/transportation-management/ (Viewed on July 20, 2021).

Abstracts of Papers

Published in Other Journals

Mechanical Engineering

Enzymatic Starch Hydrolysis Performance of Taylor-Couette Flow Reactor with Ribbed Inner Cylinder
Masahiro MATSUMOTO (University of Shizuoka), Hayato MASUDA, Robert HUBACZ (Warsaw University of Technology), Takafumi HORIE (Kobe University), Hiroyuki IYOTA, Makoto SHIMOYAMDA (University of Shizuoka) and Naoto OHMURA (Kobe University)
Chemical Engineering Science, Vol. 231, 116270 (2021).
In this study, a Taylor–Couette flow reactor (TCFR) was applied to starch hydrolysis accompanied with an intricate viscosity change during reaction for the purpose of process intensification. In industries, several reactors are used in starch hydrolysis, namely gelatinization, liquefaction, and saccharification. It was possible to conduct a continuous starch hydrolysis with one TCFR. In addition, a sufficient reducing sugar yield was obtained in the Taylor vortex flow regime. However, the yield decreased at a higher effective Reynolds number (Re_{eff}) due to axial dispersion through a bypass flow generated by the wavy motion of Taylor cells. In order to immobilize Taylor vortex flow at this condition, a ribbed inner cylinder was employed which suppressed axial dispersion at the higher Re_{eff}. As a result, a higher reducing sugar yield was successfully obtained than that by using a standard cylinder, demonstrating that the optimization of TCFR geometry has the potential for process intensification.

Melting Characteristics of Ice Cream Prepared with Various Agitation Speeds in Batch Freezer
Momoko SAWANO (University of Shizuoka), Hayato MASUDA, Hiroyuki IYOTA and Makoto SHIMOYAMADA (University of Shizuoka)
Chemical Engineering Transactions, Vol. 87, pp. 337-342 (2021).
Ice cream consists of air bubbles, fat globules, ice crystals and unfrozen solution phase. The physical and chemical property of ice cream such as flavor or texture depends on its microstructure. Mainly, the microstructure is formed during freezing process. In this study, the effect of agitation speed during the freezing process on the melting characteristics was investigated. Samples prepared with various agitation speeds were used for melting tests. The melting rate of sample was quantified by measuring the mass that drips from the hardened ice cream through a mesh screen as a function of time. It was found that the melting rate increased with the increase in the agitation speed. This result means that the control of melting characteristics based on the agitation speed is possible. In addition, the increase in the amount of air cells and the size of fat globule aggregates led to the increase in the melting rate. In order to completely understand the thermal property of ice cream, the complex interaction between air cells and fat globules including ice crystal should be investigated.

Effect of Rheological Property on Leidenfrost Droplet Motion
Shinichiro OKUMURA, Hayato MASUDA and Hiroyuki IYOTA
Proc. of the 2nd Asian Conference on Thermal Sciences, on-line, Oct. 3-7, No. 20621 (2021).
The effect of rheological properties on the Leidenfrost droplet motion was investigated experimentally. It was revealed that the Leidenfrost point for polymeric liquid droplets was lower than that of the water droplet. In addition, the lifetime of polymeric liquid droplet was prolonged owing to the static levitation at a relatively low surface temperature.

Degree of Supercooling of Sugar Aqueous Solution in Freezing Process with Agitation
Tomohiro RYUZAKI, Hayato MASUDA and Hiroyuki IYOTA
Proc. of the 2nd Asian Conference on Thermal Sciences, on-line, Oct. 3-7, No. 50523 (2021).
The effect of agitation speed on the freezing process of the sucrose aqueous solution was investigated. It was found that the degree of supercooling and the time scale for nucleation and growth of ice crystals were affected by the agitation speed.

Estimation of Wide-range Humidity in High Temperature Airflow in Oven for Food Industry
Naoto YUJI, Koki MINAMI, Hayato MASUDA and Hiroyuki IYOTA
Proc. of the 2nd Asian Conference on Thermal Sciences, on-line, Oct. 3-7, No. 50524 (2021).
Herein, a simple model for heat/mass transfer accompanying condensation and evaporation was proposed and confirmed to accurately estimate the temperature change of a duralumin plate in an airflow with high

temperature and humidity. This model can also be applied to measurements in the case of dynamic environments involving stepwise changes in humidity.

Development of Color and Gloss Measurement System with Wide range Temperature and Humidity Control Unit
Shimpei FUKAGAWA, Hiroyuki IYOTA, Hideki SAKAI and Mai ISOMI
Proc. of International Colour Association (AIC) 14th Congress, on-line, pp. 137-142 (2021).
We have developed equipment for measuring the color and glossiness of objects in a wide range of temperature and humidity conditions. This equipment can control temperatures up to 100 °C and 5%-100% humidity ranges and measure the color and glossiness of objects using a well-calibrated digital camera. We verified the measurement accuracy and found that the color difference is quite small and that we can obtain accurate glossiness data in the of dark color range. We demonstrated the results of the measurement of silica gel (whose color changes with humidity) and black beans (Japanese traditional food, whose glossiness changed with temperature). We obtained important experimental data on the relationship among temperature/humidity, weight of the materials, and color/glossiness.

Proposal of Non-Contact Colorimetric Measurement of Materials in a Closed Space
Mai ISOME, Hideki SAKAI and Hiroyuki IYOTA
AIJ J. Technol. Des., Vol. 27, No. 67, pp. 1166-1170 (2021).
It was shown that the color of materials in a closed space can be measured from the outside of space under diffuse illuminations by using a concave glass as a partition. The measurement accuracy is $\Delta E^*_{ab} = 0.9$ in average for 24 colors of the standard color chart, where ΔE^*_{ab} is the color difference in $L^*a^*b^*$(D65/ 2-deg.) color space of JIS Z8781- 4. It is lower than that of the conventional colorimetry without a glass partition, in which the measurement accuracy is $\Delta E^*_{ab} = 0.7$ in average; it is, however, high enough compared to that of visual colorimetry.

Development New Cooking System in Mass Food-serviced Institutions - Analysis of Palatability of Cooked Foods Processed by High Pressure Treatment -
Seiko AKITA, Ayumi SAWADA, Miho KAKUI, Tadashi AKAO, Satoshi ITO, Hiroyuki IYOTA, Tatsuo KAI, Koichi TANABE and Yuya ASAMI
Prepared Foods and Technology, Vol. 27, No. 1, pp.1-8 (2021).
The present study was conducted to analyze palatability of cooked foods processed by high pressure treatment. Mechanical analysis of conducted cooked chicken steak processed by high pressure treatment showed that changed breaking and textural characteristics. In addition, changes in color characteristics of chicken steak were found. The present study showed that changes in mechanical and color characteristics were clarified as palatability of chicken steak processed by high pressure treatment The present findings suggests that high pressure treatment can utilized in mass food-serviced institutions.

Simultaneous Control of Speed and Thrust of Hydraulic Actuator with Magnetorheological Fluids Valve Using Rectangular Pulse Wave Control
Nobuo OSHIMA, Masaya FUKUDA and Yuhei SHIMIZU
Journal of the Japan Fluid Power System Society, Vol. 52, No. 2, pp.32-38 (2020) (in Japanese).
Magnetorheological fluids (MR Fluids) are suspensions which consist of soft magnetic particles and base liquid. By applying magnetic field, the particles make chain-like structure and rheological properties of the MR fluids show remarkable change. This characteristic is suitable for constructing control devises. In those devices, a MR fluids valve is one of promising devises. Because, the MR fluids valve can be controlled without mechanical mechanism, so the MR fluids valve has excellent reliability. In case of applying the MR fluids valve to controlling a hydraulic actuator, pressure (thrust) control is easy, but speed control is difficult. Because, the MR fluids have Bingham plastic characteristics, so pressure drop due to flow velocity is small compared to that due to yield shear stress. So, a rectangular pulse wave control based on pulse width modulation (PWM) control method taking account of yield shear stress of MR fluids and time constant of MR fluids valve is proposed and simultaneous control of speed and thrust of the hydraulic actuator with MR fluids valve is performed.

Localization method using planar LiDAR for mobile robots to support bridge inspection
Hyunwoo SONG, Jun NAKAHAMA and Yogo TAKADA
Transactions of the JSME, Vol. 87, No. 896, 15 pages (2021) (in Japanese).

In recent years, the deterioration of infrastructure facilities such as bridges has become a problem. Precautionary measures such as visual inspections and repair by humans are in place as countermeasures for aging, but there are problems with cost and safety in such inspections. If inspection by robots becomes possible, both will be improved, which will greatly contribute to the maintenance of infrastructure facilities. In this paper, we propose a localizational position specifying system for a robot supporting bridge inspection of the moving robot under the bridge to support inspection of the bridge. Since the robot must travel on the steel structures at the bottom of the bridge, strong permanent magnets need to be installed on the edge parts in the wheels. Also, it is not possible to receive the coordinate information from the satellite as it travels at the bottom of the bridge. Therefore, a 1-dimensional low-cost LiDAR sensor and a stepping motor are used to implement as a planar LiDAR sensor which rotates 360 degrees, specify the position of the current robot by obtaining distance and direction data from fixed feature points. The localizational position specification through the planar LiDAR are examined by the experiment. As a result, it was possible to estimate the localizational position of the robot.

Localization Method Based on Image Processing for Autonomous Driving of Mobile Robot in the Linear Infrastructure
Hyunwoo SONG, Jun NAKAHAMA and Yogo TAKADA
Proc. the 13th Conference of the International Sports Engineering Association, Online, June 22-26, 49, 115, 7 pages (2020). *Automation, Control and Intelligent Systems*, Vol. 9, No.1, pp.34-45 (2021).
In recent years, the deterioration of infrastructure facilities such as bridges has become a problem. Precautionary measures such as visual inspection and repair by humans are in place as countermeasures for aging; however, there are issues with cost and safety in such inspections. If inspection by robots becomes possible, both these aspects will be improved, which will significantly contribute to the maintenance of infrastructure facilities. In this paper, we propose a complex image processing technique to specify the location of feature points as coordinates through smartphone cameras to obtain the location information of feature points needed for positioning BIREM-IV-P developed to support bridge inspection. The corners located in the bridge inspection environment are used as feature points, and the corners are specified using Harris corner detection, which is a conventional corner detection method, to obtain the position of the feature points. In addition, to compensate for the shortcomings of Harris corner detection, a line segment in the image is detected using the Hough transform, and the intersection points of the line segments are recognized as corners. By combining the results of the two detection methods in this manner, the target feature points can be accurately specified. Then, the position of the feature points of the specified image coordinate system can be changed to the world coordinate system. As a result, it was possible to detect the location of the target feature points in a three-dimensional coordinate system.

Effects of Centroid Position on Running Performance of Bridge Inspection Robot BIREM-IV
Hyunwoo SONG, Ryota HATANAKA and Yogo TAKADA
IOSR Journal of Mechanical and Civil Engineering, Vol. 18, No. 2, pp. 41-49 (2021).
Since the period of high economic growth, the deterioration of social infrastructure, such as bridges and tunnels, has become increasingly serious. To prevent ageing, this infrastructure requires periodic inspection and repair; however, inspection is costly and time-consuming and, hence, there is a strong demand for practical bridge inspection robots to reduce the associated cost and time of inspections. The bridge inspection robot BIREM-IV, as developed in a previous study, uses magnetic rimless wheel and is capable of free movement in steel structures, exhibiting a high running performance. However, because autonomous driving is desired for the practical bridge inspection robot BIREM-IV, it is necessary to install inspection devices - such as sensors and cameras - for localization, as well as determine the allowable weight and appropriate mounting positions. In this study, we examined how driving performance changes with changing weight and center of gravity via simulations, using a mechanical model of BIREM-IV. The simulation was developed based on the parameters of BIREM-IV, confirming that the simulation matches the actual machine. In addition, it was possible to determine the unstable positions of the robot's center of gravity - which resulted in falling or being unable to drive - via the mechanical model by changing the position of the center of gravity and the weight of the BIREM-IV.

Establishment of a Method for Correcting the Image Coordinates of a Target Captured by a Robotic Fish with Rolling Motion
Naoki KAWASAKI, Takuya ARITANI and Yogo TAKADA
Transactions of the JSME, Vol.87, No.901, p. 21-00104 (15 pages) (2021) (in Japanese).
A robotic fish is ideal for an ecological survey of underwater life, because underwater animals cannot easily

notice the robot. However, when a robotic fish swings its body to swim, it makes a rolling motion due to movements of the center of gravity and this rolling motion has a bad influence on the coordinate calculation of the tracking target, therefore it is necessary to correct the image. The robot has FPGA (Field Programmable Gate Array) and it is suitable for real-time image processing because FPGA has excellent performance with its parallel processing. In this study, we create a program to calculate the roll angle of the robot by using the gyro and acceleration sensor mounted on the robot and to correct the image by rotating it by that angle. Then, we conduct an evaluation of this rotation correction method with rotation tester that reproduces the rolling motion of the robotic fish and determine synchronization timing of image data and angle data because the CMOS camera used for the robot adopts rolling shutter method. Furthermore, we investigate the effect on coordinate calculation by the fish robot with created program. We have confirmed that this robot can perform real-time correction of rotated image and reduce the influence on the coordinate calculation of the target.

Effect of Acid on the Decrease in Antibacterial properties of Oxygen-Free Copper by Wiping with an Ethanol Aqueous Solution

Shuhei NISHIDA, Yuzo TODA and Hiroshi KAWAKAMI
J. Jap. Inst. Copper, Vol. 60, pp. 241-245 (2021) (in Japanese).
Bacterial and viral infections spread as bacteria and viruses propagate through the surface of the environment. It is expected that the introduction of antibacterial metal materials such as copper and copper alloys on the environmental surface will sterilize the environmental surface and prevent the spread of infection. When copper and copper alloys are actually used, there is a concern that the copper surface may be soiled due to human contact. It is necessary to clean the copper surface because the antibacterial property is reduced due to surface contamination. Although cleaning removes contaminations on the surface, the detergent used for cleaning may corrode the copper surface and lose antibacterial properties. In medical facilities, sodium hypochlorite aqueous solution or alcohol is often used for cleaning. For aqueous sodium hypochlorite solution, adding anti-rust can prevent the deterioration of antibacterial properties and the deterioration of surface properties due to wiping. Therefore, in this study, we investigate a cleaning method using alcohol that maintains surface texture and antibacterial properties. Oxygen-free copper was used as the test material. Alcohol added acid was used for cleaning. The effect of the detergent used for cleaning on the surface of oxygen-free copper was investigated. The operation of immersing the test piece in the drug for 15 seconds and drying it for 1 hour was repeated 168 times. The surface of the test piece was observed, the antibacterial property was evaluated, and the surface was analyzed by X-ray photoelectric spectroscopy. The antibacterial properties of oxygen-free copper were maintained after W-D cycle with alcohol added acid. The surface texture of oxygen-free copper was maintained after W-D cycle alcohol added citric acid. However, after W-D cycle with alcohol added hydrochloric acid, sulfuric acid, oxalic acid, and acetic acid, the surface properties of oxygen-free copper deteriorated. As a result, it was found that the deterioration of the surface properties and antibacterial properties of oxygen-free copper can be prevented by wiping with alcohol added citric acid.

Fatigue Crack Growth Behavior of Adhesively-Bonded Unidirectional and Woven CFRP/Aluminum Joints with Acrylic Adhesive

Keisuke HARA, Hayato NAKATANI, Makoto IMANAKA, Yousuke KOUNO and Toru IKEDA
Journal of the Society of Materials Science, Japan, Vol. 70, No. 7, pp. 567-572 (2021) (in Japanese).
Structural acrylic adhesives have been attracted special interest because theses adhesives can be cured at room temperature and can be bonded to oily substrates. To use adhesively bonded joints more widely for structural use, it is necessary to clarify fatigue crack propagation characteristics. In this study, fatigue crack growth rate was measured using adhesively bonded unidirectional and woven CFRP/aluminum double cantilever beam (DCB) joints with an acrylic adhesive. To elucidate the difference of fatigue crack growth rates between adhesive joints with unidirectional and woven CFRP adherends, finite element analysis was conducted for these joints, wherein Gurson's model was applied to the adhesive layer. The differences of fatigue crack growth rate can be elucidated from the distributions of void fraction in front of the crack tip for the both joints.

Layer-Thickness Dependence of Hardness and Local Buckling Behavior in Electrodeposited Ni-Co-Cu/Cu Multilayered Films

Yoshihisa KANEKO, Tomohiro KUBOMAE, Naoki KAWAKAMI, Hiroyuki HAGIWARA and Makoto UCHIDA
Mater. Sci. Forum, Vol.1016, pp.170-176 (2021).
The effect of layer thickness on hardness and buckling behavior was investigated on Ni-Co-Cu/Cu multilayered films. The Ni-Co-Cu/Cu multilayered films were grown on annealed copper substrates by

electrodeposition. We fabricated the multilayered films with various layer thicknesses ranging from 10 nm to 1000 nm. First, dependence of Vickers hardness on the Cu layer thickness was investigated. When the Ni-Co-Cu layer had the constant thickness of 75 nm and the Cu layer thickness was smaller than 75 nm, the hardness increased rapidly with decreasing Cu layer thickness. Subsequently, compressive tests were conducted on the multilayered films having the component layers ranging from 100 nm to 1000 nm, where the hardness values did not change rapidly with layer thickness. The copper substrates coated with the multilayered films were compressed until 20% strain. From SEM surface observations after the compressive tests, formations of band-like structures having a certain thickness were recognized. Cross-sectional observation revealed that some band-like structures were formed as a result of local buckling of the multilayered film. The vertical thickness of the bank-like structures increased linearly with increasing component layer thickness.

Characterization of Size-Affected Non-Uniform Deformation of Polycrystalline Copper
Makoto UCHIDA, Kensho TSUTSUMI, Masashi SAKAMOTO and Yoshihisa KANEKO
Int. J. Mech. Sci., Vol. 211, 106760 (2021).
In polycrystalline materials, with the increase in grain size relative to the macrostructure, the collective behavior of crystal grains affects their macroscopic deformation field. To investigate the effect of relative size on the mechanical behavior of polycrystalline materials, the interaction between the microstructure-induced non-uniform deformation and the specimen shape-induced non-uniform deformation was evaluated based on experimental and numerical studies of uniaxial tensile tests of polycrystalline copper specimens with a curved gauge section. The effects of the macroscopic stress gradient and grain size on the strain field of the specimen were evaluated using specimens with different curvature radii obtained from different thermal treatment conditions. The development of strain distribution was measured using the digital image correlation method. A high strain concentration was observed at the minimum cross-section region in the specimen with smaller grains, whereas such strain concentration was relaxed in the specimen with larger grains because a random strain distribution occurred owing to the polycrystalline structure. A full-scale crystalline plasticity finite element method simulation, under conditions similar to those in the experiment, was then performed. Deformation concentrated zone, in which the length and width depended on the grain size, occurred in the polycrystalline specimen. The cross- section of the specimen was locally reduced when the deformation concentrated zone reached the free surface, and the tensile force became smaller for the specimen with larger grains. To discuss the relative specimen size effect, the plastic strain was divided into local and nonlocal plastic strains. Both the experimental and simulation results clarified that the nonlocal plastic strain gradient evaluated in the finite volume region increased with the region-averaged stress. From these results, we proposed a constitutive equation for the plastic strain as a function of local stress and finite volume averaged stress. The nonlocal plastic work for the evaluation region, which is estimated using the nonlocal strain gradient, increased with the stress during the strain-hardening stage in both the simulation and experimental results.

Applied Physics and Electronics

Fabrication of p⁺-Si/p-diamond heterojunction diodes and effects of thermal annealing on their electrical properties

Yota UEHIGASHI, Shinya OHMAGARI (National Institute of Advanced Industrial Science and Technology (AIST)), Hitoshi UMEZAWA (National Institute of Advanced Industrial Science and Technology (AIST)), Hideaki YAMADA (National Institute of Advanced Industrial Science and Technology (AIST)), Jianbo LIANG, and Naoteru SHIGEKAWA
Diamond and Related Materials, in press. DOI: 10.1016/j.diamond.2021.108665

We fabricate p^+-Si/p-diamond heterojunction diodes by using surface-activated bonding and examine the electrical properties of Si/diamond interfaces by measuring current-voltage and current-voltage-temperature characteristics. We find that the electrical properties of heterojunction diodes are improved by post-bonding annealing at temperatures up to 873 K in terms of the ideality factor and reverse-bias current. Additionally, fabricated diodes also reveal thermal stability better than that of Cu/diamond Schottky diodes in terms of the rectification factor. The barrier height at Si/diamond bonding interfaces annealed at 873 K is estimated to be 0.55 and 0.66 eV by analyzing the relationship between the saturation current density and temperature and the reverse bias characteristics at room temperature, respectively. These values are close to that obtained by assuming that no offset is formed in the vacuum level across the Si/diamond bonding interfaces (0.36 eV).

Fabrication of GaN/Diamond Heterointerface and Interfacial Chemical Bonding State for Highly Efficient Device Design

Jianbo LIANG, Ayaka KOBAYASHI, Yasuo SHIMIZU (Institute for Materials Research (IMR), Tohoku University), Yutaka OHNO (Institute for Materials Research (IMR), Tohoku University), Seong-Woo KIM (Adamant Namiki Precision Jewel. Co., Ltd), Koji KOYAMA (Adamant Namiki Precision Jewel. Co., Ltd), Makoto KASU (Saga University), Yasuyoshi NAGAI (Institute for Materials Research (IMR), Tohoku University), and Naoteru SHIGEKAWA
Adv. Mater. Vol. 33, 2104564 (2021).

The direct integration of GaN and diamond holds much promise for high-power devices. However, it is a big challenge to grow GaN on diamond due to a large thermal expansion coefficient mismatch between GaN and diamond. In this work, the fabrication of a GaN/diamond heterointerface is successfully achieved by a surface activated bonding (SAB) method at room temperature. A small compressive stress exists in a GaN/diamond heterointerface, which is significantly smaller than that of the GaN-on-diamond structure with a transition layer formed by crystal growth. A 5.3-nm-thick intermediate layer composed of amorphous carbon and diamond is formed at the as-bonded heterointerface. Ga and N atoms are distributed in the intermediate layer by diffusion during the bonding process. Both the thickness and the sp^2 ratio of the intermediate layer decrease as the annealing temperature increases, which indicates that the amorphous carbon is directly converted into diamond after annealing. The diamond of the intermediate layer acts as a seed crystal. After annealing at 1000 °C, the thickness of the intermediate layer is decreased to approximately 1.5 nm, where lattice fringes of the diamond (220) plane are observed. The intensity gradients for C, Ga, and N atoms become more abrupt with the reduction of the intermediate layer thickness. Diffusion of the C atom into the GaN adjacent to the heterointerface is observed, with the C atom acting as a dopant that compensates for the nitrogen vacancies in the GaN to increase the breakdown voltage. These results indicate that the GaN/diamond heterointerface has a high thermal and high mechanical stability, thus making it very suitable for application to improve the thermal management of the power devices and develop new functional devices.

Room Temperature Direct Bonding of Diamond and Semiconductor Layer in Atmospheric Air

Jianbo LIANG, Yuji NAKAMURA, Yutaka OHNO (Institute for Materials Research (IMR), Tohoku University), Yasuo SHIMIZU (Institute for Materials Research (IMR), Tohoku University), Yasuyoshi NAGAI (Institute for Materials Research (IMR), Tohoku University), Hongxing WANG (Xian Jiaotong University, China), Makoto KASU (Saga University), and Naoteru SHIGEKAWA
Funct. Diam. Vol. 1, 110 (2021).

The direct bonding of diamond and InGaP is achieved in atmospheric air at room temperature. The surface of the bonding materials is treated only by chemicals. Although, the averaged roughness (Ra) value of the InGaP surface is larger than 1 nm, a steady bonded interface is obtained that is free from interfacial voids and mechanical cracks. An atomic intermixing layer with a thickness of about 8 nm is formed at the bonding

interface before annealing, which is composed of C, In, Ga, P, and O atoms. After annealing at 400 °C, no exfoliation happened along the bonding interface is observed, and an increase of about 2 nm in the thickness of the atomic intermixing layer is observed. The increased thickness of the atomic intermixing layer plays a role in alleviating the thermal stress caused by the difference of thermal expansion coefficient between the bonding materials. The bonding interface demonstrates an excellent applicability to device fabrication processes. This bonding method has a large potential for direct bonding of large diameter diamond and semiconductor materials.

Modulation of Characteristics of Si Solar Cells by Luminescence-Downshifting Zn-Based Nanoparticles with Mn doped

Yuki IDUTSU, Jianbo LIANG, Hisaaki NISHIMURA, DaeGwi KIM, and Naoteru SHIGEKAWA
Proc. 2020 47th IEEE Photovoltaic Specialists Conference (PVSC). DOI: 10.1109/PVSC45281.2020.9300637
We deposit Mn-doped Zn-based nanoparticles (NPs) on Si solar cells using the drop casting and layer-by-layer methods and measure their current-voltage and spectral response characteristics. The solar cells covered by the NPs show higher conversion efficiencies due to the interference of the layered NPs. We also observe enhancement of internal quantum efficiency (IQE) of Si cells, which is due to the luminescence downshifting (LDS) of deposited NPs. A model for describing effects of LDS on IQE is also provided.

Fabrication of high-quality GaAs/diamond heterointerface for thermal management applications

Jianbo LIANG, Yuji NAKAMURA, Tianzhuo ZHANG (Waseda University), Yutaka OHNO (Institute for Materials Research (IMR), Tohoku University), Yasuo SHIMIZU (Institute for Materials Research (IMR), Tohoku University), Kazu KATAYAMA (Waseda University), Takanobu WATABABE (Waseda University), Hideto YOSHIDA (The Institute of Scientific and Industrial Research (ISIR), Osaka University), Yasuyoshi NAGAI (Institute for Materials Research (IMR), Tohoku University), Hongxing WANG (Xian Jiaotong University, China), Makoto KASU (Saga University), and Naoteru SHIGEKAWA
Diam. Relat. Mater. Vol. 111, 108207 (2021).
The direct integrating of GaAs and diamond is achieved at room temperature via a surface activated bonding method. An ultrathin crystal defect layer composed of GaAs and diamond was formed at the bonding interface. The thickness of the GaAs and diamond crystal defect layers was determined to be 0.4 and 1.6 nm, respectively. The thermal characterization of the transmission line model (TLM) patterns formed on the GaAs layer bonded to diamond and sapphire substrates is demonstrated. The thermal resistance of the GaAs TLM patterns formed on the diamond and sapphire substrates was determined to be 6 and 34.9 K/W, respectively. The GaAs TLM patterns formed on the diamond showed an excellent heat dissipation property due to the high thermal conductivity of diamond.

Nanostructural Investigation on GaAs//Indium Tin Oxide/Si Junctions for III-V-on-Si Hybrid Multijunction Cells

Tomoya HARA, Jianbo LIANG, Kenji ARAKI (Toyota Technological Institute) Takefumi KAMIOKA (Toyota Technological Institute), Hassanet SODABANLU (The University of Tokyo, Tokyo), Kentaroh WATANABE (The University of Tokyo, Tokyo), Masakazu SUGIYAMA (The University of Tokyo, Tokyo), and Naoteru SHIGEKAWA
ECS Transactions, Vol. 98 (4) pp. 125-133 (2020).
We investigate nanostructural properties of GaAs//indium tin oxide (ITO)/Si junctions fabricated by surface-activated bonding with emphasis on impacts of thermal process. Both of the Ga 2p3/2 and As 2p3/2 core-level spectra obtained by hard X-ray photoemission spectroscopy show that the GaAs layers are oxidized by annealing at 400 °C. This finding is consistent with the formation of amorphous-like layers at 400 °C annealed GaAs//ITO interfaces. Concentration depth profiles of O, Ga, and As suggest that the oxidation markedly occurs at GaAs//ITO interfaces annealed at temperatures higher than 200 °C, which is consistent with the dependence of resistance in GaAs//ITO/Si junctions on annealing temperature. These results suggest that annealing brings about the reaction between GaAs and ITO layers and causes the degradation of the electrical properties of GaAs//ITO interfaces. Low temperature process technologies are essential so as to make a full use of ITO as intermediate layers in III-V-on-Si multijunction cells.

III-V Thin-Film Solar Cells Bonded to Si Substrates via Metal Grids

Takashi HISHIDA, Jiabo LIANG, and Naoteru SHIGEKAWA
ECS Transactions, Vol. 98 (4) pp. 117-123 (2020).
Using surface-activated bonding technologies, we bond InGaP/GaAs double-junction (2J) solar-cell structures

invertedly-grown on GaAs substrates to metal grids formed on conductive Si substrates. The metal grids are made of 170-nm SiO2 layers and 310-nm Ti/Au metal layers. 2J cells are fabricated by eliminating the GaAs substrates and forming emitter and base contacts. The emitter contacts are aligned to the metal grids. The fabricated 2J cells reveal a lower series resistance in comparison with cells directly bonded to Si substrates, which is likely to be due to a lower resistance across GaAs//metal grid junctions than that across GaAs//Si junctions. A higher open-circuit voltage and a larger internal quantum efficiency are also observed for the 2J cells on metal grids. These features as well as the oscillation in reflectance spectrum suggest that the 2J cells work as optically-isolated thin-film cells

Fabrication of GaN/SiC/diamond Structure for Efficient Thermal Management of Power Device
Ryo KAGAWA, Keisuke KAWAMURA (Air Water Inc.), Yoshiki SAKAIDA (Air Water Inc.), Sumito OUCHI (Air Water Inc.), Hiroki URATANI (Air Water Inc.), Yasuo SHIMIZU (Institute for Materials Research (IMR), Tohoku University), Yutaka OHNO (Institute for Materials Research (IMR), Tohoku University), Yasuyoshi NAGAI (Institute for Materials Research (IMR), Tohoku University), Naoteru SHIGEKAWA and Jianbo LIANG
Extended Abstracts of 2021 IEEE International Workshop on Low Temperature Bonding for 3D Integration (LTB-3D), Online, October 5-11, pp.15 (2021).

Structural Analysis of Diamond/Silicon Heterointerfaces Fabricated by Surface Activated Bonding at Room Temperature
Yutaka OHNO (Institute for Materials Research (IMR), Tohoku University), Jianbo LIANG, Hideto YOSHIDA (The Institute of Scientific and Industrial Research (ISIR), Osaka University), Yasuo SHIMIZU (Institute for Materials Research (IMR), Tohoku University), Yasuyoshi NAGAI (Institute for Materials Research (IMR), and Naoteru SHIGEKAWA
Extended Abstracts of 2021 IEEE International Workshop on Low Temperature Bonding for 3D Integration (LTB-3D), Online, October 5-11, pp.12 (2021).

Fabrication of Ga$_2$O$_3$/Si Direct Bonding Interface for High Power Device Applications
Jianbo LIANG, Daiki TAKATSUKI, Yasuo SHIMIZU (Institute for Materials Research (IMR), Tohoku University), Masataka HIGASHIWAKI (National Institute of Information and Communications Technology), Yutaka OHNO (Institute for Materials Research (IMR), Tohoku University), Yasuyoshi NAGAI (Institute for Materials Research (IMR), and Naoteru SHIGEKAWA
Extended Abstracts of 2021 IEEE International Workshop on Low Temperature Bonding for 3D Integration (LTB-3D), Online, October 5-11, pp.19 (2021).

Fabrication and Characterization of GaN/Diamond Boding Interface
Ayaka KOBAYASHI, Yasuo SHIMIZU (Institute for Materials Research (IMR), Tohoku University), Yutaka OHNO (Institute for Materials Research (IMR), Tohoku University), Seong-Woo KIM (Adamant Namiki Precision Jewel. Co., Ltd.), Koji KOYAMA (Adamant Namiki Precision Jewel. Co., Ltd.), Makoto KASU (Saga University), Yasuyoshi NAGAI (Institute for Materials Research (IMR), Tohoku University), Naoteru SHIGEKAWA, and Jianbo LIANG
Extended Abstracts of 2021 IEEE International Workshop on Low Temperature Bonding for 3D Integration (LTB-3D), Online, October 5-11, pp.41 (2021).

Fabrication of Ga$_2$O$_3$/3C-SiC Direct Bonding for Efficient Surface Heat Dissipation
Hiromu NAGAI, Keisuke KAWAMURA (Air Water Inc.), Yoshiki SAKAIDA (Air Water Inc.), Hiroki URATANI (Air Water Inc.), Yasuo SHIMIZU (Institute for Materials Research (IMR), Tohoku University), Yutaka OHNO (Institute for Materials Research (IMR), Tohoku University), Yasuyoshi NAGAI (Institute for Materials Research (IMR), Tohoku University), Naoteru SHIGEKAWA, and Jianbo LIANG
Extended Abstracts of 2021 IEEE International Workshop on Low Temperature Bonding for 3D Integration (LTB-3D), Online, October 5-11, pp.41 (2021).

High Temperature Stability of p$^+$-Si/p-Diamond Heterojunction diodes
Yota UEHIGASHI, Shinya OHMAGARI (National Institute of Advanced Industrial Science and Technology), Hitoshi UMEZAWA (National Institute of Advanced Industrial Science and Technology), Hideaki YAMADA (National Institute of Advanced Industrial Science and Technology), Jianbo LIANG, and Naoteru SHIGEKAWA

Extended Abstracts of 2021 IEEE International Workshop on Low Temperature Bonding for 3D Integration (LTB-3D), Online, October 5-11, pp.13 (2021).

Polarization Inverted GaN/GaN Junctions Fabricated by Surface-Activated Bonding
Kazuki SAWAI, Jianbo LIANG, Yasuo SHIMIZU (Institute for Materials Research (IMR), Tohoku University), Yutaka OHNO (Institute for Materials Research (IMR), Tohoku University), Yasuyoshi NAGAI (Institute for Materials Research (IMR), Tohoku University), and Naoteru SHIGEKAWA
Extended Abstracts of 2021 IEEE International Workshop on Low Temperature Bonding for 3D Integration (LTB-3D), Online, October 5-11, pp.21 (2021).

Nanostructural Analysis of Al/β-Ga$_2$O$_3$ Interface Fabricated Using Surface Activated Bonding
Zexin WAN, Jianbo LIANG, Yasuo SHIMIZU (Institute for Materials Research (IMR), Tohoku University), Yutaka OHNO (Institute for Materials Research (IMR), Tohoku University), Yasuyoshi NAGAI (Institute for Materials Research (IMR), Tohoku University), and Naoteru SHIGEKAWA
Extended Abstracts of 2021 IEEE International Workshop on Low Temperature Bonding for 3D Integration (LTB-3D), Online, October 5-11, pp.27 (2021).

Coplanar Waveguides Fabricated by Directly Bonding Metal Foils to High-Resistivity Si Substrates
Kenya YONEKURA, Tasuku KAWAMOTO, Jianbo LIANG, Eiji SHIKOH, Koichi MAEWAWA (University of Toyama), and Naoteru SHIGEKAWA
Extended Abstracts of 2021 IEEE International Workshop on Low Temperature Bonding for 3D Integration (LTB-3D), Online, October 5-11, pp.47 (2021).

Direct bonding of diamond to semiconductors and metals for low thermal resistance modules (Invited)
Naoteru SHIGEKAWA and Jianbo LIANG
31st International Conference on Diamond and Carbon Materials (ICDCM 2021), Online, September 6-9 (2021).

Low-temperature direct wafer bonding innovating CS device technologies (Plenary)
Naoteru SHIGEKAWA and Jianbo LIANG
International Conference on Compound Semiconductor Manufacturing Technology (CS-MANTECH 2021), Online, May 27-June 27 (2021).

Effect of high-energy heavy-ion irradiation on electromechanical coupling factor of piezoelectric lead zirconate titanate
Seiji TAKECHI, Shogo FUJITA, Naoki KONISHI, Takashi MIYACHI(Chiba Institute of Technology), Masanori KOBAYASHI(Chiba Institute of Technology), Osamu OKUDAIRA(Chiba Institute of Technology), Nagaya OKADA(Honda Electronics Co., Ltd.), Masayuki FUJII(Famscience Co., Ltd.), Hiromi SHIBATA(Osaka University), Takeshi MURAKAMI(National Institutes for Quantum and Radiological Science and Technology) and Yukio UCHIHORI(National Institutes for Quantum and Radiological Science and Technology)
Jpn. J. Appl. Phys., Vol. 60, pp. 038003-1-038003-3 (2021)
The variation of the electromechanical coupling factor of lead zirconate titanate (PZT) was studied using a piezoelectric PZT disk exposed to a 400 MeV/n xenon beam. The resonant and antiresonant frequencies were measured in pairs by an impedance analyzer in situ manner. A systematic behavior of the pairs resulted in a decrease of the coupling factor. It was found that the coupling factor linearly decreased with increasing integrated beam energy incident on the PZT disk while its surface temperature was equilibrium at room temperature. We discuss a possible PZT-based radiation detector for practical use in a high-radiation field.

Materials Synthesis Using Plasma in Contact with Liquid Phase ~Toward Efficient Utilization of the Plasma/Liquid Interface~
Tatsuru SHIRAFUJI
Mater. Sci. Technol. Jpn., Vol. 58, pp. 168-171 (2021) (in Japanese)
In the material process that proceeds in the liquid phase in contact with the plasma, the plasma/liquid interface, which is directly affected by the plasma, is important. This paper describes a three-dimensional integrated micro solution plasma aiming at high efficiency and large capacity by forming a large number of plasma/liquid interfaces in the liquid. We also describe the one-pot synthesis of a free-standing film on the liquid surface,

which was carried out based on the idea of using only the plasma/liquid interface.

Polymerization of EDOT by a Gas-Liquid Interfacial Process Using Dielectric-Barrier-Discharge Plasma of He Gas Plasma
Tatsuru SHIRAFUJI, Shyunta HIRANO, Jun-Seok OH
J. Inst. Electrostat. Jpn. Vol. 44, 259 (2 pages) (2020)
3,4-ethylenedioxythiophene (EDOT) liquid was irradiated with dielectric-barrier-discharge plasma of He for 10 min. This gas-liquid interfacial process converted the transparent EDOT to brown colored liquid. Results of infrared absorption spectroscopy on the product indicated that EDOT was partially converted to poly-3,4-ethylene dioxythiophene.
DOI: https://doi.org/10.35848/1347-4065/abcbd1

Rapid Measurement of Yeast Status Using the Phase Angles of Harmonics in the Electrical Response Waveform
Keita TAMURA, Naoto HIGASHIHARA, Daichi TANAKA, Masafumi MURAJI, Kenji TANAKA, Tatsuru SHIRAFUJI
IEEJ. Trans. Fundament. Mater., Vol. 141, pp. 239-244 (2021)
We assessed the time dependence of the difference between living and dead yeast suspensions, in terms of the amplitudes and phase angles of their harmonics, when an alternating current (AC) voltage was applied to a yeast suspension. The measurements were repeatable, and it was possible to accurately and quickly determine yeast status (living or dead) even within 1 s by reference to the phase angles of the 3rd harmonic. We found that measuring the phase angle of a dead yeast suspension in the system in advance permits us to distinguish between living and dead yeast without the need to calculate their relation to fundamental components such as the amplitude. This method based on the phase angles of harmonics is a powerful and convenient technique for quickly determining the status of yeast. These nonlinear responses change due to the presence of yeast itself and the collection of data on them including phase angles helps us to understand the electrical properties of cells.

***In Vivo* Study on the Healing of Bone Defect Treated with Non-thermal Atmospheric Pressure Gas Discharge Plasma**
Akiyoshi SHIMATANI, Hiromitsu TOYODA, Kumi ORITA, Yoshihiro HIRAKAWA, Kodai AOKI, Jun-Seok OH, Tatsuru SHIRAFUJI, and Hiroaki NAKAMURA
PLOS ONE 0255861 (15 pages) (2021)
Medical treatment using non-thermal atmospheric pressure plasma (NTAPP) is rapidly gaining recognition. NTAPP is thought to be a new therapeutic method because it could generate highly reactive species in an ambient atmosphere which could be exposed to biological targets (e.g., cells and tissues). If plasma-generated reactive species could stimulate bone regeneration, NTAPP can provide a new treatment opportunity in regenerative medicine. Here, we investigated the impact of NTAPP on bone regeneration using a large bone defect in New Zealand White rabbits and a simple atmospheric pressure plasma (helium microplasma jet). We observed the recovery progress of the large bone defects by X-ray imaging over eight weeks after surgery. The X-ray results showed a clear difference in the occupancy of the new bone of the large bone defect among groups with different plasma treatment times, whereas the new bone occupancy was not substantial in the untreated control group. According to the results of micro-computed tomography analysis at eight weeks, the most successful bone regeneration was achieved using a plasma treatment time of 10 min, wherein the new bone volume was 1.51 times larger than that in the plasma untreated control group. Using H&E and Masson trichrome stains, nucleated cells were uniformly observed, and no inclusion was confirmed, respectively, in the groups of plasma treatment. We concluded the critical large bone defect were filled with new bone. Overall, these results suggest that NTAPP is promising for fracture treatment.
DOI: https://doi.org/10.1371/journal.pone.0255861

Total reflection X-ray fluorescence analysis with a glass substrate treated with a He atmospheric pressure plasma jet
Kouichi TSUJI, Tsugufumi MATSUYAMA, Tsuneo FUKUDA, Soichiro SHIMA (Suntory MONOZUKURI Expert), Mayuko TOBA (Suntory MONOZUKURI Expert), Jun-Seok OH, and Tatsuru SHIRAFUJI
J. Anal. At. Spectrom. Vol. 36, 1873 (6 pages) (2021)
Total reflection X-ray fluorescence (TXRF) is a powerful technique for trace elemental analysis of various liquid samples. A small volume of the liquid sample is dropped onto a flat substrate, and the dried residue is

measured using TXRF. Usually, the substrate surface is treated with a silicone solution to make it hydrophobic. Such hydrophobic substrates are useful to concentrate the analyte at a small point, leading to a dot-type residue. However, the solution sample will provide a residue with a height of several tens of mm depending on the matrix of the solution, in which self-absorption is a serious problem. In this paper, the authors applied a He atmospheric pressure plasma jet (APPJ) treatment to a glass substrate to obtain a hydrophilic surface. The chemical properties of the glass substrate surface were drastically changed by the application of the He APPJ. The contact angle of the liquid droplet was 5.2º on the APPJ-treated glass, while it was 88.8º on the glass with a silicone layer. A droplet of the liquid solution smoothly spread over the APPJ-treated glass substrate, leading to a thin film-like residue. The recovery and detection limits for TXRF analysis of a standard solution sample were improved especially for low-Z elements by using the APPJ-treated glass substrates. This new sample preparation technique was also applied for TXRF analysis of a red wine sample. We found that this hydrophilic glass substrate gave a film-like residue from a small droplet of the red wine. Reasonable TXRF quantitative results were obtained by the Ga internal standard method. The preliminary experimental results suggested that the film-type residue produced on the APPJ-treated substrate was effective in decreasing the matrix effect especially for low-Z elements.
(This is identical to the abstract that appears in the section of Applied Chemistry and Bioengineering)
DOI: https://doi.org/10.1039/D1JA00164G

Identification of Key Neutral Species in Atmospheric-Pressure Plasma for Promoting Proliferation of Fibroblast Cells

Yuki HORI (Meijo University), Naoyuki IWATA (Nagoya University), Vladislav GAMALEEV (Nagoya University), Jun-Seok OH, Tomiyasu MURATA (Meijo University), Masaru HORI (Nagoya University), and Masafumi ITO (Meijo University)
Plasma Process Polym. Vol. 18, e2000225 (10 pages) (2021)
To identify the key neutral species from atmospheric-pressure plasma for promoting the proliferation of fibroblast cells, an atmospheric-pressure radical generator was employed. A cell viability assay showed that the proliferation of fibroblasts was significantly promoted through radical treatment, resulting in the highest promotion ratio of 24%. The densities of the neutral radicals supplied by the radical generator were measured via mass spectrometry at atmospheric pressure. To determine an effective factor for the promotion, the dose dependencies of these radicals on the promotion ratio were investigated. The promotion ratio exhibited a strong correlation only with the NO• dose. These results confirmed that NO• is a direct trigger of plasma-enhanced cell proliferation.
DOI: https://doi.org/10.1002/ppap.202000225

Time of Flight Size Control of Carbon Nanoparticles Using Ar+CH₄ Multihollow Discharge Plasma Chemical Vapor Deposition Method

Sung Hwa HWANG (Kyushu University), Kazunori KOGA (Kyushu University), Yuan HAO (Kyushu University), Pankaj ATTRI (Kyushu University), Takamasa OKUMURA (Kyushu University), Kunihiro KAMATAKI (Kyushu University), Naho ITAGAKI(Kyushu University), Masaharu SHIRATANI (Kyushu University), Jun-Seok Oh, Susumu TAKABAYASHI (Ariake College), and Tatsuyuki NAKATANI (Okayama University of Science)
Processes Vol. 9, 2 (10 pages) (2021)
As the application of nanotechnology increases continuously, the need for controlled size nanoparticles also increases. Therefore, in this work, we discussed the growth mechanism of carbon nanoparticles generated in Ar+CH4 multi-hollow discharge plasmas. Using the plasmas, we succeeded in continuous generation of hydrogenated amorphous carbon nanoparticles with controlled size (25–220 nm) by the gas flow. Among the nanoparticle growth processes in plasmas, we confirmed the deposition of carbon-related radicals was the dominant process for the method. The size of nanoparticles was proportional to the gas residence time in holes of the discharge electrode. The radical deposition developed the nucleated nanoparticles during their transport in discharges, and the time of flight in discharges controlled the size of nanoparticles.
DOI: https://doi.org/10.3390/pr9010002

Inactivation Mechanism of Fungal Spores Through Oxygen Radicals in Atmospheric-Pressure Plasma

Masafumi ITO (Meijo University), Hiroshi HASHIZUME (Nagoya University), Jun-Seok OH, Kenji ISHIKAWA (Nagoya University), Takayuki OHTA (Meijo University), Masaru HORI (Nagoya University)
Intl. J. Plasma Environ. Sci. Technol. Vol. 13, 1 (6 pages) (2021)

A brief history of the development of our plasma technology for the disinfection of agricultural harvests is presented in this review. We focused on the influence of reactive oxygen species (ROS), e.g. ground-state oxygen atoms [$O(^3P_j)$], excited-state oxygen molecules [$O_2(^1\Delta_g)$], and ozone (O_3), generated from atmospheric-pressure plasmas on the inactivation of fungal spores under dry conditions. For elucidating the inactivation mechanisms, it is essential to reveal the key ROS. Using some powerful tools, we revealed that the dose of $O(^3P_j)$ strongly correlates with the inactivation of fungal spores when compared to those of another ROS, such as $O_2(^1\Delta_g)$ and O_3. The balance of antioxidants in the spores is possibly modulated by $O(^3P_j)$, leading to oxidation of organelles in spores. Herein, we introduce and discuss how $O(^3P_j)$ contributes to the inactivation of fungal spores associated with in situ diagnostics of plasma generated ROS and in situ intracellular observations of a few fungal spore species.

Simple and Direct Estimation Method for Split-Off Hole Effective Mass from Franz-Keldysh Oscillations Appearing in Photoreflectance Spectra: A Feasibility Study Using GaAs Epitaxial Layer Structures at Room Temperature

Hideo TAKEUCHI (Osaka City University, Sophia University Yotsuya Campus) and Sotaro FUJIWARA

We investigated a feasibility of directly estimating split-off hole effective mass m_{so} from Franz-Keldysh oscillations using non-destructive and non-invasive photoreflectance spectroscopy. We used an undoped/n-type GaAs epitaxial structure and two GaAs p-i-n diode structure. We observed the phenomenon that Franz-Keldysh oscillations, which originate both the E_0 fundamental transition and from the $E_0+\Delta_{so}$ transition energy, appears in the photoreflectance spectra at room temperature. Initially, from the electro-optic constant $\hbar\Theta_{HH}$ of the Franz-Keldysh oscillations originating from the E_0 fundamental transition, we deduced the built-in electric field F in each sample with the use of the relation $\hbar\Theta_{HH} = (e^2\hbar^2F^2/2\mu_{HH})^{1/3}$, where the quantity μ_{HH} is the reduced effective mass of the electron and heavy hole. In the next step, we calculated the reduced effective mass μ_{so} of the electron and split-off hole using the relation $\hbar\Theta_{so} = (e^2\hbar^2F^2/2\mu_{so})^{1/3}$, where the quantity $\hbar\Theta_{so}$ is the electro-optic constant of the Franz-Kelysh oscilations from the $E_0+\Delta_{so}$ transition. Finally, we estimated the split-off hole effective mass m_{so} from the reduced effective mass μ_{so}. The estimated split-off hole effective mass agrees with the reported value obtained experimentally. Thus, we conclude that the split-off hole effective mass is estimatable from analyzing the Franz-Keldysh oscillations in the photoreflectance spectra. We also compare the present hole effective masses to those theoretically known and discuss the appropriateness of the electronic-band calculations.

Selective hydrothermal synthesis of water-soluble CdTe and CdTe/CdS colloidal quantum dots by controlling the Te/Cd molar ratio of the precursor solution

Kunio SHIMURA, TaeGi LEE, Tatsuya ITO, and DaeGwi KIM

During the synthesis of CdTe quantum dots (QDs) by the hydrothermal method, a CdS shell layer is naturally formed by the thermal decomposition of thiol ligands, and CdTe/CdS core/shell QDs are produced. Herein, we investigate the selective synthesis of CdTe and CdTe/CdS QDs to control the thermal decomposition of thiol ligands by changing the Te/Cd molar ratio of the precursor solutions. From the experimental results of X-ray photoelectron spectroscopy and optical properties of absorption and photoluminescence (PL) spectra and PL decay profiles of the synthesized colloidal QDs, it was found that the formation of the CdS shell can be controlled by varying the Te/Cd ratio of the precursor solution. Thus, the selective synthesis of CdTe and CdTe/CdS QDs with the same PL energy but different PL decay times is possible.

Origin of photoluminescence of water-soluble CuInS$_2$ quantum dots prepared via a hydrothermal method

Kazutaka IIDA, Yota UEHIGASHI, and DaeGwi KIM

This study was performed to investigate the origin of the photoluminescence (PL) properties of hydrothermally-synthesized water-soluble CuInS$_2$ (CIS) quantum dots (QDs). The corresponding PL decay profiles, time-resolved PL spectra, and excitation intensity dependence of the PL spectra were evaluated. The decay profiles exhibited a strong dependence on the detection energy, and the peak of the time-resolved PL spectra shifted to lower energies with increasing time. With increasing excitation light intensity, the PL peak shifted to the high-energy side. These experimental results were consistent with the characteristics of donor-

acceptor pair emission. The PL properties of Cu-doped and non-doped CdSe QDs, which show Cu-related and defect-related PL emission, respectively, were compared. Based on these results, it was concluded that donor-acceptor pair emission is the underlying mechanism of the PL of the hydrothermally-synthesized water-soluble CIS QDs.
DOI: 10.1039/d1ra05761h

Water-soluble ZnSe/ZnS:Mn/ZnS quantum dots convert UV to visible light for improved Si solar cell efficiency
Hisaaki NISHIMURA, Takaya MAEKAWA, Kazushi ENOMOTO, Naoteru SHIGEKAWA, Tomomi TAKAGI, Susumu SOBUE, Shoichi KAWAI, and DaeGwi KIM
J. Mater. Chem. C Vol. 9, pp. 693-701 (2021).
The sensitivity of Si solar cells to the UV portion of the solar spectrum is low, and must be increased to further improve their efficiencies. In this study, water-soluble ZnSe/ZnS:Mn/ZnS core/shell/shell quantum dots (QDs) capable of converting UV into visible light were synthesized by a hydrothermal method. A photoluminescence quantum yield of 84% was achieved by carefully investigating and optimizing the QD preparation conditions. Furthermore, we prepared wavelength-conversion glass containing the ZnSe/ZnS:Mn/ZnS QDs dispersed in sol-gel glass and applied it to Si solar cells. As a result, the spectral sensitivity of the Si solar cell at wavelengths shorter than 400 nm was significantly improved, and the amount of power generated (conversion efficiency) was increased by 7.4% compared with that of the cell without the wavelength-conversion glass coating.
DOI: 10.1039/d0tc04580b

Spin injection into vanadium dioxide films from a typical ferromagnetic metal, across the metal–insulator transition of the vanadium dioxide films
Kazuma TAMURA, Teruo KANKI (Osaka Univ.), Shun SHIRAI, Hidekazu TANAKA (Osaka Univ.), Yoshio TEKI (Graduate School of Science, OCU) and Eiji SHIKOH
AIP Advances, Vol.11, pp. 035120-1 ~ 035120-4 (2021).
A vanadium dioxide VO_2 film shows metal-insulator transition (MIT) induced by changing environmental temperature. We report the temperature dependence of electromotive force properties generated in $VO_2/Ni_{80}Fe_{20}$ bilayer junctions under the ferromagnetic resonance (FMR) of the $Ni_{80}Fe_{20}$ layer. An electromotive force generated in a $VO_2/Ni_{80}Fe_{20}$ bilayer junction under the FMR showed a small change across the MIT temperature of the VO_2 film, while the VO_2 film resistance drastically changed. This behavior was not only explained with the temperature dependence of the electromotive force property generated in the $Ni_{80}Fe_{20}$ film itself under the FMR, but also with the generated electromotive forces due to the inverse spin-Hall effect (ISHE) in the VO_2 film under the FMR of the $Ni_{80}Fe_{20}$ film. That is, we successfully demonstrated the spin injection from a $Ni_{80}Fe_{20}$ film into a VO_2 film across the MIT temperature of the VO_2 film.

An energy harvesting technology controlled by ferromagnetic resonance
Yuta NOGI, Yoshio TEKI (Graduate School of Science, OCU) and Eiji SHIKOH
AIP Advances, Vol.11, pp. 085114-1 ~ 085114-5 (2021).
We have successfully demonstrated electrical charging using the electromotive force (EMF) generated in a ferromagnetic metal (FM) film under ferromagnetic resonance (FMR). In the case of $Ni_{80}Fe_{20}$ films, electrical charge due to the EMF generated under FMR can be accumulated in a capacitor; however, the amount of charge is saturated well below the charging limit of the capacitor. Meanwhile in the case of $Co_{50}Fe_{50}$, electrical charge generated under FMR can be accumulated in a capacitor and the amount of charge increases linearly with the FMR duration time. The difference between the $Ni_{80}Fe_{20}$ and $Co_{50}Fe_{50}$ films is due to the respective magnetic field ranges for the FMR excitation. When the FM films were in equivalent thermal states during FMR experiments, $Co_{50}Fe_{50}$ films could maintain FMR in a detuned condition, while $Ni_{80}Fe_{20}$ films were outside the FMR excitation range. The EMF generation phenomenon in an FM film under FMR can be used an energy harvesting technology by appropriately controlling the thermal conditions of the FM film.

Wide Viewing Zone and High-Resolution Autostereoscopic Display with Smooth Motion Parallax Using Crosstalk between Two Viewpoint Images in One Eye
Sho SHIBUYA, Yukiya YAMAGUCHI, Rintaro KUBO, Goro HAMAGISHI, Kayo YOSHIMOTO and Hideya TAKAHASHI
Proc. The International Display Workshops, Vol.27, pp.443-446 (2020).
We propose a high-resolution multi-view display based on an autostereoscopic display that can display motion parallax images according to the viewer's position. Specifically, the motion parallax is realized by displaying binocular images for the left and right eyes according to changes in the eye position. In this proposed method, the crosstalk between the binocular images viewed by the left and right eyes is kept very low. In that state, we generate crosstalk in one eye image by combining adjacent two viewpoint images effectively where the eye is present. In this way, smooth motion parallax instead of fixed viewpoint intervals is realized. In this paper, we made a prototype display and evaluated the proposed method.

Image Quality Improvement of Glasses-Free 3D Display Using Parallax Barrier with Eye Tracking System to Expand Viewing Zone in All Directions
Shion KANEMARU, Yukiya YAMAGUCHI, Rintaro KUBO, Goro HAMAGISHI, Kayo YOSHIMOTO and Hideya TAKAHASHI
Proc. The International Display Workshops, Vol.27, pp.447-450 (2020).
When we expand the viewing zone of glasses-free 3D display, it is effective to divide screen into multiple areas, and control them optimally. While lines that cause uncomfortable viewing occur on all boundaries of the divided areas. We propose a method to erase the control boundary lines by changing the image arrangement of the binocular parallax image smoothly across the divided areas. In this method, we firstly define switch sub-pixels as the sub-pixels that cause a difference in the image arrangement of the binocular parallax images

between the adjacent divided areas. The mixed sub-pixel value of the left-eye image and the right-eye image are displayed on the switch sub-pixels, and the mixing ratios are changed according to the positions of the switch sub-pixels in the divided area. As a result, the binocular parallax image can smoothly switch between each divided area and this method makes the control boundary line invisible. In order to verify the effectiveness of this proposed method, we measure crosstalk at certain viewing distances, and we perform subjective evaluation.

Augmented Reality Support System for Endoscopic Surgery Using Spectral Reflectance Estimation
Sanae DEGUCHI, Kayo YOSHIMOTO, Yosuke TAKAHASHI, Toshihiko SHIBATA and Hideya TAKAHASHI
Proc. SPIE Advanced Biomedical and Clinical Diagnostic and Surgical Guidance Systems XIX, Vol.11631, pp.1163113-1-116113-8 (2021).
In cardiac surgery, a method avoids cutting the sternum and ribs using an endoscope is known as Minimally Invasive Cardiac Surgery (MICS). MICS can be used for mitral valve prolapse. In this surgery, an annuloplasty ring is inserted to form the valve and since each person has a different valve size, an appropriate size must be selected by applying a sizer. We propose a system that supports surgery by superimposing a virtual image of the valve ring on the endoscopic image using Augmented reality (AR) technology. Marker detection needs to be performed for AR display. However, since organ surfaces are similar in color, we use the spectral reflectance of the material to obtain more information than RGB image. To avoid the use of special optics to measure the spectral reflectance, we estimate spectral reflectance from RGB images using principal component analysis. The areas containing the marker are obtained by similarity index and the 3D positions of the markers are determined from center of gravity measurements. Then, we superimpose the AR image onto the endoscope image by perspective transformation to the image plane and masking using estimated 3D position of markers. To evaluate our method, we validated the spectral reflectance estimation and AR display using pig hearts marked with crystal violet. We found that the accuracy of spectral reflectance estimation is sufficient for AR display and the AR image was almost the same as the actual ring size. Therefore, our proposed method is expected to increase the efficiency of the operation.

A Viewing Zone Enlargement Method for Autostereoscopic Display with Eye Tracking for the Viewer Observing at a Large Angle for the Normal Direction of the Display
Rintaro KUBO, Goro HAMAGISHI, Kayo YOSHIMOTO, Kaoru KUSAFUKA (Kyocera Corp.) and Hideya TAKAHASHI
Proc. SPIE Advanced in Display Technologies XI, Vol.11708, pp.117080S-1-117080S-11 (2021).
We have proposed a wide-viewing area autostereoscopic displays using eye tracking system in order to expand the viewing zone of glasses-free stereoscopic displays using a parallax barrier. It was possible to keep the stereoscopic vision by arranging parallax images at geometrically optimal positions based on the viewer's position detected by eye tracking even if the viewer moved. However, due to the expansion of the viewing zone, when the viewer observes a display at a large angle for the normal direction of the display, the influence of the refraction of light rays by the material between the parallax barrier and the display becomes large and the optimum position to arrange parallax images changes. As a result, the crosstalk occurs, and the stereoscopic vision was lost in the areas of large angles. In order to overcome this problem, we propose the image processing method considering the influence of refraction to extremely increase the viewing zone angle. Considering the influence of the refraction, we evaluate the position of the subpixel actually observed by the viewer. Based on the evaluation, we correct the position of the parallax images. To verify the effectiveness of the proposed method, we measured crosstalk at the OVD. When we use the proposed method, the viewing zone angle with a crosstalk rate of 10% or less for the entire display could be expanded to ±30° compared to viewing zone angle ±12.8 without proposed method.

Retinal Projection Type Super Multi-View 3D Head-Mounted Display with the Variable Function Shutter Using a DMD
Takuro OHARA, Kayo YOSHIMOTO and Hideya TAKAHASHI
Proc. SPIE Advanced in Display Technologies XI, Vol.11708, 117080T-1-117080T-8 (2021).
We have previously proposed the retinal projection type super multi-view 3D-HMD which provides the viewer with 3D images by inducing the stimulus of the accommodation of the viewer's eye using the blurring of the

multiple projected retinal images. However, in the previous HMD using a mechanical shutter, since we could not flexibly design the function of the shutter, we could not project the ideal multiple retinal images. To overcome this problem, we propose the improved 3D-HMD with the variable function shutter using a DMD as an optical shutter. In the proposed 3D-HMD, multiple parallax images are displayed by time division, and these images are converged on respective points by the holographic lens. However, the parallax image converges not only on the correct convergent point but also on unnecessary convergent points due to using the multiple exposure holographic lens. Therefore, to pass only one convergent light corresponding to the correct parallax image, we used the DMD shutter synchronized to the display device. To verify the effectiveness of using a DMD as a shutter, we made the prototype 3D-HMD and confirmed that the blur of the image by the prototype 3D-HMD can induce the accommodation. Since the high-speed optical shutter using a DMD realizes the function as a shutter by changing the pinhole image on the DMD, we can flexibly design the number and the alignment of convergent points in the proposed 3D-HMD. Therefore, in the proposed 3D-HMD, we can project the ideal multiple projection retinal image by using the DMD shutter.

Application of supervisory control to secret protection in discrete-event systems
Shoma MATSUI (Queen's Univ.), Kai CAI
Journal of the Society of Instrument and Control Engineers (SICE), Special Issue on Event-Based Control in the IoT Era, Vol.60, pp. 14 ~ 20 (2021).
In this paper we introduce the problem of protecting secret states in the plant with at least m (≥ 1) protections and minimizing protection costs. This problem is formulated as that of finding a protection policy such that every string leading to secret states from the initial state has at least m protectable events, and the protection costs are minimum simultaneously. We present an algorithm to provide a solution of the problem. This algorithm is demonstrated with an illustrating example.

Optimal secret protections in discrete-event systems
Ziyue MA (Xidian Univ.), Kai CAI
IEEE Transactions on Automatic Control, DOI: 10.1109/TAC.2021.3091438 (2021).
In this paper we study a security problem of protecting secrets in discrete-event systems modeled by deterministic finite automata. In the system some states are defined as secrets, each of which is associated with a security level. The problem is to design an event-protecting policy such that any event sequence from the initial state that reaches a secret state contains a number of protected events no less than the required level of security. To solve this secret securing problem, we first develop a layered structure called the security automaton. Then we show that the problem is transformed to a supervisory control problem in the security automaton. We consider two criteria of optimality on protecting policies: (1) disruptiveness, i.e., protecting policies with a minimum degree of disturbance to legal users' normal operations; (2) cost, i.e., protecting policies with a minimal cost. For the optimality on disruptiveness, we prove that a minimally disruptive protecting policy is obtained by using the classical supervisory control theory in the security automaton. For the optimality on cost, we develop a method to obtain a protecting policy with minimal cost by finding a min-cut in the security automaton.

Improvement of Detection Limits for Particle Contamination by Confocal Configuration in X-Ray Fluorescence Microscope
Hitomi NAKANO, Shintaro KOMATANI, Tsugufumi MATSUYAMA, Kouichi TSUJI
Analytical Sciences, Vol. 37, pp. 1447-1451 (2021)
Micro X-ray fluorescence (XRF) enables the non-destructive analysis of particle contamination. In this study, we compared the detection sensitivities and the LLD (lower limit of detection) values of micro-metallic particle contaminations on the plastic detected by micro-XRF and confocal micro-XRF. First, to verify the effectiveness of the confocal micro-XRF, we compared the intensities of different shaping copper samples (plate, thin film and particle). The results demonstrated that confocal micro-XRF is more effective than micro-XRF for the detection of micro particles. Second, to compare the SN ratios of different X-ray energies, several micro-metallic particles (Si, Fe, and Cu) set on the acrylic plate were measured by micro-XRF and confocal micro-XRF. It was found that the SN ratios of the confocal micro-XRF when measuring the Si, Fe, and Cu particles were improved to be approximately 14.7, 21.9, and 43.5 times those of the micro-XRF, respectively. It was determined that confocal micro-XRF was more effective for micro-metallic particles in the higher energy region.

Total Reflection X-ray Fluorescence Analysis of Trace Elements in High-Concentration Matrix Solutions Using a Carbon-Coated Glass Substrate
Tsugufumi MATSUYAMA, Takumi FURUSATO, Hikari TAKAHARA, Kouichi TSUJI
Advances in X-ray Analysis, Vol. 64, pp. 87-93 (2021)
Total reflection X-ray fluorescence (TXRF) analysis is an effective technique to determine the concentration of trace elements present in aqueous samples. In TXRF analysis, a drop (10 µL) of the sample solution is placed and dried on a substrate, such as silicon wafer and quartz slide. The dried residue is then analyzed using a TXRF spectrometer. However, when the sample solution has a high-concentration matrix, the accuracy of the TXRF analysis will impeded because of the significant self-absorption displayed by the sample. Therefore, to overcome this limitation, a thin-film residue could be used while analyzing a solution with a high concentration matrix. In this study, a novel carbon-coated substrate was developed to facilitate the formation of a thin-film residue. The TXRF analysis of a wastewater sample was performed using the developed substrate, and the results were compared to those obtained by using hydrophobic quartz glass and resist-pattern substrates. Because of the use of the carbon-coated substrate, lower relative standard deviation values and better recovery, than those obtained by using the quartz glass slide, were achieved.

Total reflection X-ray fluorescence analysis with a glass substrate treated with a He atmospheric pressure plasma jet
Kouichi TSUJI, Tsugufumi MATSUYAMA, Tsuneo FUKUDA, Soichiro SHIMA, Mayuko TOBA, Jun-Seok Oh, Tatsuru SHIRAFUJI
J. Anal. At. Spectrom., Vol. 36, pp.1873-1878 (2021)
Total reflection X-ray fluorescence (TXRF) is a powerful technique for trace elemental analysis of various liquid samples. A small volume of the liquid sample is dropped onto a flat substrate, and the dried residue is measured using TXRF. Usually, the substrate surface is treated with a silicone solution to make it hydrophobic. Such hydrophobic substrates are useful to concentrate the analyte at a small point, leading to a dot-type residue. However, the solution sample will provide a residue with a height of several tens of mm depending on the matrix of the solution, in which self-absorption is a serious problem. In this paper, the authors applied a He atmospheric pressure plasma jet (APPJ) treatment to a glass substrate to obtain a hydrophilic surface. The chemical properties of the glass substrate surface were drastically changed by the application of the He APPJ. The contact angle of the liquid droplet was 5.2 on the APPJ-treated glass, while it was 88.8 on the glass with a silicone layer. A droplet of the liquid solution smoothly spread over the APPJ-treated glass substrate, leading to a thin film-like residue. The recovery and detection limits for TXRF analysis of a standard solution sample were improved especially for low-Z elements by using the APPJ-treated glass substrates. This new sample preparation technique was also applied for TXRF analysis of a red wine sample. We found that this hydrophilic glass substrate gave a film-like residue from a small droplet of the red wine. Reasonable TXRF quantitative results were obtained by the Ga internal standard method. The preliminary experimental results suggested that the film-type residue produced on the APPJ-treated substrate was effective in decreasing the matrix effect especially for low-Z elements.

Monitoring of life environment by analysis of particles in air on the mask
Koki YAMAGUCHI, Tsugufumi MATSUYAMA, Kouichi TSUJI
Perspective and Topics, 81th Conference on Analytical Chemistry, 9 (2021) (in Japanese)
The particles captured by the mask were analyzed by total reflection X-ray fluorescence (TXRF) method. The piece of the mask with a size of 3 mm x 3mm were put on the flat quartz glass, then it was solved by heating it more than the melting point. This process arrowed the thin-film like sample preparation of the mask, which was suitable for TXRF analysis. We found that the small amount of Cl, K and Cu were included in the particles captured by the mask. This simple technique was useful for monitoring of particulate matters in air.

Monitoring for Corrosion Elution Process of Steel Sheet in NaCl Solution using Total Reflection X-ray Fluorescence Analysis
Koji AKIOKA, Hideki TAKABE, Takashi DOI, Tatsushi YOSHIOKA, Yukiko IMANISHI, Tsugufumi MATSUYAMA, Kouichi TSUJI
Adv. X-Ray. Chem. Anal., Japan, Vol. 52, pp. 151-160 (2021) (in Japanese)
To evaluate the corrosion behavior of steel sheet in a CO2 gas corrosive environment, the total reflection X-ray fluorescence (TXRF) analysis was performed focusing on the solution eluted by corrosion. The solution was continuously collected from near the surface of the corroded steel to generate micro volume droplets that were used for TXRF analysis. The immersion time and temperature dependence of the X-ray fluorescence (XRF) signal derived from Fe ions suggested that a protective film was formed on the surface of the steel sheet. It was also found that it is important to reduce the sampling amount of the solution so as not to affect the reaction environment of corrosion and film formation. From the above, it is considered that the spatial resolution of solution analysis has improved and the diffusion process of Fe ions, which are elution elements, has been observed. This method is useful for detail analysis near the solid-liquid interface, and it is expected to be applied to the analysis of solid-liquid interface reactions.

Development and Evaluation of Confocal Line XRF Instrument with Double Slits System
Shota SONODA, Hitomi NAKANO, Tsugufumi MATSUYAMA, Kouichi TSUJI
Adv. X-Ray. Chem. Anal., Japan, Vol. 52, pp. 55-62 (2021) (in Japanese)
X-ray fluorescence (XRF) analysis offers the great advantage of providing nondestructive elemental analysis at an ambient pressure. However, it is not possible to obtain the 3D elemental image because primary X-rays penetrate deep into the sample. To obtain the 3D elemental image, polycapillary lens are placed in front of an X-ray tube and a detector in confocal micro XRF method. The foci of primary X-ray and XRF are adjusted to be at the same point, which is called the confocal point and confocal micro XRF method obtains XRF spectra in the confocal point. When this method is applied to a sample with layer structure, it is not necessary to obtain the 2D plane imaging. To reduce the measurement time for obtaining the 2D depth profile, we proposed confocal line XRF method. Developed instrument was equipped with an X-ray tube, a detector and limited slits. Limited slits that were placed in front of an X-ray tube and a detector were used to prepare the thin X-ray beams. The focus line between primary X-ray and XRF is adjusted to be at the same line. We called this line "confocal line" and confocal line XRF method obtains XRF spectra in the region. In this study, we evaluated the performances such as a beam size, a spatial resolution and a lower limit of detection in confocal line XRF instrument. Usefulness of the analytical method was shown by measuring a sample with layer structure.

69th Annual Denver X-ray Conference Report
Kouichi TSUJI
Adv. X-Ray. Chem. Anal., Japan, Vol.52, pp. 257-260 (2021) (in Japanese)
69th Denver X-ray conference was held virtually in the period from 3-7 August 2020. The contents included the pre-recorded lectures, oral presentations and poster presentations were opened for registered participants until the end of August. Best Poster Awards in XRF division were given to the following two posters:
1) X-ray Analytical Techniques for Determining Trace Elements in a Single Human Hair and Atmospheric Aerosols, T. Matsuyama, T. Hayakawa, H. Yamaguchi and K. Tsuji, Osaka City University, Japan.
2) Development of Confocal Line X-ray Fluorescence Instrument and Application to Layer Structure Samples, S. Sonoda, T. Matsuyama, K. Tsuji, Osaka City University, Japan, and H. Nakano, Osaka City University and HORIBA Ltd. Research & Development, Japan.

Total reflection X-ray fluorescence analysis of aerosol particles with direct dissolution of the collection filter on a substrate

Tsugufumi MATSUYAMA, Hiroki YAMAGUCHI, Kouichi TSUJI

J. Anal. At. Spectrom., Vol. 36, pp. 570-575 (2021)

Determining the amounts of metallic elements in atmospheric aerosols is important for estimating their origin and evaluating their potential effects on human health. In this study, we developed a new method based on total reflection X-ray fluorescence (TXRF) analysis for the characterization of atmospheric aerosols. The filter used to collect the aerosol was placed on a silicon wafer as a sample carrier and dissolved in an aliquot of acetone. The remaining residue, i.e. the dissolved filter paper, was thin; thus, most of the aerosols collected in the filter paper could be measured by the thin X-ray beam. This approach improved the minimum detection limits of the measured target metals, making it possible to measure trace elements in atmospheric aerosols.

Fundamental research for a new confocal line X-ray spectrometer

Hitomi NAKANO, Shota SONODA, Tsugufumi MATSUYAMA, Shintaro KOMATANI, Kouichi TSUJI

X-Ray Spectrometry, Vol. 50, pp. 224-230 (2021)

Confocal X-ray fluorescence (XRF) spectrometry can be used to perform three-dimensional elemental analysis, which is impossible using general micro XRF spectrometry without any collimating optics in the detection channel. In this study, we designed, for the first time, a new confocal line XRF (C-L-XRF) system that can obtain elemental information of a larger area and higher intensity in XRF analysis than conventional confocal point XRF (C-P-XRF) analysis. We evaluate the basic performance of C-L-XRF, such as XRF intensity and horizontal and depth spatial resolutions. We identified that the spatial resolution of C-L-XRF in the horizontal and depth directions is approximately 2.9 and 2.6 times those of conventional C-P-XRF. However, it is possible to obtain an XRF intensity that is approximately 33 times higher than C-P-XRF intensity. C-L-XRF is expected to be effective for analyzing wide-area samples such as layered samples.

X-ray Fluorescence Analysis

Kouichi TSUJI

Y. Sorin, K. Tsuji, M. Fujiwara, H. Minami (eds.), *Handbook of Instrumental Analysis*, Kagaku Dojin, Vol. 3, pp. 77-93 (2021) (in Japanese)

Fundamental and applications of X-ray Fluorescence (XRF) analysis were introduced for students and beginners of elemental analysis. The topics such as generation of X-rays, principle of XRF analysis, sample preparation, qualitative and quantitative elemental analysis and applications of XRF to environmental, industrial and biological samples were shown. In addition, micro-XRF and total reflection XRF techniques were described with instructive figures.

Efficient Capturing of Hydrogen Peroxide in Dilute Aqueous Solution by Co-crystallisation with Amino Acids

Ryota YAMAGUCHI, Rika TANAKA, Mayu MAETANI, Hiroyasu TABE, Yusuke YAMADA

CrystEngComm, Vol. 23, 5456-5462 (2021).

Hydrogen peroxide (H_2O_2) was efficiently captured by co-crystallization with enantiomeric and racemic amino acids such as L-phenylalanine, DL-phenylalanine, and DL-asparagine in a dilute aqueous solution of H_2O_2 (30%) to unveil the requisites for efficient capturing of H_2O_2. In further dilute solutions of H_2O_2 (0.5–20%), L-Phe provided certain amounts of co-crystals with H_2O_2; however, co-crystals with H_2O_2 were hardly obtained for DL-Phe and DL-Asn. The efficient H_2O_2 capturing with L-Phe can be ascribed to its layered motif involving water molecules. The results obtained here would contribute to the development of an adsorbent that can efficiently capture H_2O_2 produced in environment-friendly H_2O_2-production systems such as photocatalytic systems.

Enhanced Catalytic Stability of Acid Phosphatase Immobilized in the Mesospaces of a SiO$_2$-nanoparticles Assembly for Catalytic Hydrolysis of Organophosphates

Hiroyasu TABE, Hiroyuki OSHIMA, Shusaku IKEYAMA, Yutaka. AMAO, Yusuke YAMADA

Mol. Catal., Vol. 510, , Article No.111669 (8 pages) (2021) .

Acid phosphatase (APase) was immobilized in discrete mesospaces of an assembly of silica nanoparticles (SiO_2NPA) to be used as a heterogeneous catalyst for the hydrolysis of organophosphates often found as pesticide residues in agricultural products. APase immobilized in SiO_2NPA exhibited higher catalytic activity than APase supported on conventional porous supports for the hydrolysis of *p*-nitrophenyl

phosphate (*p*-NPP) with quanti-tative yield of *p*-nitrophenol below pH 5.5 due to the efficient diffusion of substrates in the SiO_2NPA. Especially, a heterogeneous catalyst prepared by the co-accumulation method, in which silica nanoparticles (SiO_2NPs) dispersion containing APase was simply dried to assemble a composite catalyst ($APase/SiO_2NPA$), exhibited four times faster rate for the hydrolysis of *p*-NPP than the catalyst prepared by the equilibrium adsorption of APase in pre-assembled SiO_2NPA. The catalytic stability of immobilized APase above pH 6.0 was enhanced by surface modification of SiO_2NPs with 3-aminopropyltriethoxysilane ($APase/SiO_2NPA-NH_2$) due to the strong electro-static interaction between APase and the protonated amino groups at the pH condition. Such stability enhancement was hardly obtained by cross-linking treatment of SiO_2NPA to improve the robustness. These results suggest that electrostatic interaction between APase and SiO_2NPs is crucial to enhance catalytic stability in the wide range of pH as well as preparation methods for the stable encapsulation.

Single Open Sites on FeII Ions Stabilized by Coupled Metal Ions in CN-Deficient Prussian Blue Analogues for High Catalytic Activity in the Hydrolysis of Organophosphates
Mari YAMANE, Hiroyasu TABE, Masami KAWAKAMI, Hisashi TANAKA, Tohru KAWAMOTO, Yusuke YAMADA
Inorg. Chem. Vol. 59, 16000-16009 (2020).
CN-deficient Prussian blue analogues (PBAs), $[M^N(H_2O)_x]_y[Fe^{II}(CN)_5(NH_3)]$ ($M^N = Cu^{II}$, Co^{II}, or Ga^{III}), were synthesized and examined as a new class of heterogeneous catalysts for hydrolytic decomposition of organophosphates often used as pesticides. The active species of the CN-deficient PBAs were mainly C-bound Fe^{II} ions with only single open sites generated by liberation of the NH_3 ligand during the catalytic reactions. $[Cu^{II}(H_2O)_{8/3}]_{3/2}[Fe^{II}(CN)_5(NH_3)]$ showed higher catalytic activity than $[Co^{II}(H_2O)_{8/3}]_{3/2}[Fe^{II}(CN)_5(NH_3)]$ and $[Ga^{III}(H_2O)][Fe^{II}(CN)_5(NH_3)]$, although N-bound Cu^{II} species has been reported as less active than Co^{II} and Ga^{III} species in conventional PBAs. IR measurements of a series of the CN-deficient PBAs after the catalytic reactions clarified that a part of the NH_3 ligands remained on $[Co^{II}(H_2O)_{8/3}]_{3/2}[Fe^{II}(CN)_5(NH_3)]$ and that hydrogen phosphate formed as a product strongly adsorbed on the Fe^{II} ions of $[Ga^{III}(H_2O)][Fe^{II}(CN)_5(NH_3)]$. Hydrogen phosphate also adsorbed, but weakly, on the Fe^{II} ions of $[Cu^{II}(H_2O)_{8/3}]_{3/2}[Fe^{II}(CN)_5(NH_3)]$. These results suggest that heterogeneous catalysis of the Fe^{II}ions with single open sites were tuned by the M^N ions through metal–metal interaction.

RuO_2 Nanoparticle-Embedded Graphitic Carbon Nitride for Efficient Photocatalytic H_2 Evolution
Yoshihiro SHIMOYAMA, Kenji KOGA, Hiroyasu TABE, Yusuke YAMADA, Yoshihiro KON, and Dachao HONG
ACS Appl. Nano Mater., DOI: 10.1021/acsanm.1c02301 (9 pages) (2021).
Ruthenium oxide nanoparticles (NPs) with an average diameter of 3.5 ± 1.4 nm, embedded in graphitic carbon nitride ($RuO_2/g-C_3N_4$), were successfully prepared using a modified wet impregnation method. The $RuO_2/g-C_3N_4$ nanocomposites were employed as photocatalysts in H_2 evolution with triethanolamine (TEOA) in aqueous media under irradiation with an LED lamp. When a small amount of the RuO_2 NPs (RuO_2: 0.62 wt %) was encapsulated in $g-C_3N_4$, the H_2 evolution rate per catalyst weight (3070 $\mu mol\ h^{-1}$ g^{-1}) under basic pH conditions was remarkably improved, compared to the case with the pristine $g-C_3N_4$. Mechanistic insights into the H_2 evolution were obtained by the kinetic analysis of $RuO_2/g-C_3N_4$ with a series of alkanolamines as substrates and by X-ray photoelectron spectroscopy measurements. The results revealed that the RuO_2 NPs embedded in $g-C_3N_4$ functioned as efficient oxidation sites for converting alkanolamines into the corresponding aldehydes rather than as H_2 evolution sites. The H_2 evolution rates exhibited a saturation behavior dependent on the TEOA concentrations, suggesting the equilibrium adsorption of the hydroxyl group of TEOA on the RuO_2 surface. Conversely, the H_2 evolution on the surface of $g-C_3N_4$ under basic conditions was considered to be the rate determining step as evidenced by the kinetic isotope effects exhibited in D_2O. These results demonstrate that the $RuO_2/g-C_3N_4$ nanocomposites can serve as an effective photocatalyst for H_2 evolution in tandem with selective substrate oxidations.

Pd_2CuCo/C Hybrid with Nanoflower Morphology toward Oxygen Reduction and Formic Acid Oxidation Reactions: Experimental and Computational Studies
Biraj Jyoti BORAH, Chiranjita GOSWAMI, Yusuke YAMADA, Kohei TADA, Shingo TANAKA, Pankaj BHARALI
Energy Fuels, Vol. 35, 11515-11524 (2021).

A unique and novel structural morphology with advantageous surface defects, lattice strain, and a preferentially exposed crystal plane are indispensable criteria for offering superior and durable electrocatalytic performance. However, the design of a single electrocatalyst (EC) with all such splendors is still a challenging task. Here, we successfully developed a one pot, surfactant and organic structure directing agent free alternative EC based on Pd_2CuCo/C hybrid with nanoflower (NF) morphology. The efficacy of electrode is offered by highly open hierarchical nanostructures with a preferentially exposed (111) plane and multiple surface defects. Moreover, the half implanted Pd_2CuCo on a carbon matrix offers high stability and the metal/carbon interface provides faster electron transfer during the fuel cell operation process. Remarkably, Pd_2CuCo/C NF shows significant electrocatalytic activity toward the oxygen reduction reaction (ORR). A current density of 5.5 mA cm^{-2}, an onset potential of -0.018 V (vs Ag/AgCl), and a half-wave potential of -0.138 V were noted for the ORR of Pd_2CuCo/C NF. It delivered good methanol tolerance and enhanced stability with $\sim 80.3\%$ of the retention current, even after 21,600 sec at 1600 rpm, unlike the benchmark Pt/C catalyst. Moreover, computational studies show that Co and Cu doping in Pd_2CuCo/C alloy NF will inhibit the degradation of the electrocatalytic activity caused by strong CO adsorptions. The greater accessible active sites, the strong interfacial interaction between Pd_2CuCo NF and the carbon matrix, and the excellent synergistic interaction between Pd and Cu, Co are the major marvels for such superior electrocatalytic performance. Therefore, the present investigation offers a promising approach of designing high-performance non-Pt ECs.

Enhancing the Electrocatalytic Activity via Hybridization of Cu(I/II) Oxides with Co_3O_4 towards Oxygen Electrode Reactions

Kumar Kashyap HAZARIKA, Yusuke YAMADA, Ekaterina V. MATUS, Mikhail KERZHENTSEV, Pankaj BHARALI

Transition metal oxide based electrocatalysts (ECs) with mixed valence state have gained considerable attention in recent times. Herein, Co_3O_4–$CuO/Cu_2O/C$ nanostructure with mixed valence oxides is reported as an efficient bi-functional EC towards oxygen electrode reactions in alkaline medium. The EC displays higher current density of 6.2 mA cm^{-2} and mass activity of 12.9 mA mg^{-1} compared to that of commercially available Pt/C in 0.1 M KOH solution for oxygen reduction reaction (ORR). Rotating disk electrode measurements are used to understand the kinetics of the reaction and the EC is durable up to 1000 redox cycles. The material is highly stable up to 7000 s by retaining 99% of its initial current. The fast electron transfer is established by the smaller Tafel slope value of 83.6 mV dec^{-1}. In addition, the prepared material is also active for oxygen evolution reaction (OER) in 0.1 M KOH solution. Thus, the nanostructure with different bimetallic active sites is found to be a potential material for oxygen electrocatalysis.

Elucidating the Role of Oxide-Oxide/Carbon Interfaces of CuO_x-CeO_2/C in Boosting Electrocatalytic Performance

Chiranjita GOSWAMI, Yusuke YAMADA, Ekaterina V. MATUS, Ilyas Z. ISMAGILOV, Mikhail KERZHENTSEV, Pankaj BHARALI

Herein, we report the synthesis and bifunctional oxygen reduction reaction (ORR) and oxygen evolution reaction (OER) activities of a CuO_x-CeO_2/C electrocatalyst (EC) with rich oxide-oxide and oxide-carbon interfaces. It not only demonstrates a smaller Tafel slope (65 mV dec^{-1}) and higher limiting current density (-5.03 mA cm^{-2}) but also exhibits an onset potential (-0.10 V vs Ag/AgCl) comparable to that of benchmark Pt/C. Besides undergoing the favorable direct four-electron ORR pathway, it unveils a loss of 23% of its initial current after 6 h of a stability test and a negative shift of 4 mV in the half-wave potential after the accelerated durability test compared to the corresponding current loss of 28% and negative shift of 20 mV for Pt/C. It also reveals remarkable OER activity in an alkaline medium with a low onset potential (0.20 V) and a smaller Tafel slope (177 mV dec^{-1}). The bifunctional ORR/OER activity of CuO_x-CeO_2/C EC can be ascribed to the synergistic effects, its unique structure with enriched oxygen vacancies owing to the presence of Ce^{4+}/Ce^{3+}, robust oxide-oxide and oxide-carbon heterointerfaces, and homogeneous dispersion of oxides over the carbon bed, which facilitates faster electronic conduction.

Save Hydrogen Peroxide!
Yusuke YAMADA
Chemistry, Vol. 76, 68-69 (2021) (in Japanese).
Hydrogen peroxide (H_2O_2) was efficiently captured by co-crystallization with enantiomeric and racemic amino acids such as L-phenylalanine and DL-phenylalanine in a dilute aqueous solution of H_2O_2 (30%) to unveil the requisites for efficient capturing of H_2O_2. In further dilute solutions of H_2O_2 (0.5–20%), L-Phe provided certain amounts of co-crystals with H_2O_2; however, co-crystals with H_2O_2 were hardly obtained for DL-Phe. The efficient H_2O_2 capturing with L-Phe can be ascribed to its layered motif involving water molecules. The results obtained here would contribute to the development of an adsorbent that can efficiently capture H_2O_2 produced in environment-friendly H_2O_2-production systems such as photocatalytic systems.

Differentiating the Rate Capabilities of Lithium-Nickel-Manganese Oxide Li[Ni$_{1/2}$Mn$_{3/2}$]O$_4$ Insertion Materials and Electrodes Using Diluted Electrode Methods
Kingo ARIYOSHI, Jun SUGAWA, Shumpei MASUDA
J. Electrochem. Soc., Vol. 167, Article No. 140517 (5 pages) (2020).
Development of high-power lithium-ion batteries requires the optimization of the electrode kinetics of lithium-insertion materials to improve the rate capability of these devices. The rate capability of lithium-insertion electrodes is controlled by the concentration overvoltages that arise from changes in the Li^+ concentration at the electrode/electrolyte interface. Two distinct rate-capability behaviors prevail depending on whether charge transport is limited by Li-ion mass transfer within the solid particles or within the interstitial spaces of the electrode. In this study, the diluted electrode method is employed to characterize the two types of rate capability behavior exhibited by Li[Ni$_{1/2}$Mn$_{3/2}$]O$_4$ (LiNiMO) electrodes. Low-LiNiMO electrodes exhibit better rate capabilities than high-LiNiMO electrodes indicating that lithium-ion transport is more effective (i.e., much faster) in the solid active material than in liquid electrolyte within the electrode pore. The results provide useful insights for understanding the electrode kinetics of lithium-insertion materials and designing electrodes for high-power lithium-ion batteries.

Impact of Particle Size of Lithium Manganese Oxide on Charge Transfer Resistance and Contact Resistance Evaluated by Electrochemical Impedance Analysis
Kingo ARIYOSHI, Masumi TANIMOTO, Yusuke YAMADA
Electrochim. Acta, Vol 364, Article No. 137292 (6 pages) (2020).
To achieve high-power lithium-ion batteries, resistances of both positive and negative electrodes must be reduced, because these are the main sources of internal resistance of the batteries. It is necessary to elucidate the impact of physicochemical properties of lithium insertion materials on the resistance of electrodes, to reduce the internal resistance of the batteries. The resistance of electrodes consists of charge transfer resistance, R_{ct}, and contact resistance, R_{cont}. The diluted electrode method, in which the amount of active material in an electrode varies but retains the factors related to electrode structure, can distinguish the two resistances, R_{ct} and R_{cont}. As this method does not alter the electrode structure, it is possible to elucidate the relationship between the two resistances and the physicochemical properties of lithium insertion materials. In this study, the impact of the particle size of Li[Li$_{0.1}$Mn$_{1.9}$]O$_4$ (LMO) on the R_{ct} and R_{cont} is revealed using the electrochemical impedance analysis by applying the diluted electrode method. As the particle size of LMO increases, R_{cont} slightly decreases. The R_{ct} more strongly depends on the LMO particle size because of the change in specific surface area as a function of the particle size, although the charge transfer resistance per LMO surface area is constant. From the two resistances determined by the electrochemical impedance spectroscopy, the optimum particle morphology and electrode structure is discussed.

Determination of Solid-State Li Diffusion Coefficient of Lithium Insertion Materials from Rate Capability Tests on Diluted Electrode
Kingo ARIYOSHI, Jun SUGAWA
Electrochemistry, Vol. 89, pp. 157-161 (2021).
To establish the kinetics of the lithium insertion materials used as the electrodes in lithium-ion batteries, it is important to clarify the diffusion phenomena of lithium ions in the solid phase. Since there are two variations of the rate-determining step of a lithium insertion electrode (Li-ion diffusion in solid particles and that in the electrolyte solution), these have to be differentiated in any investigation of the diffusion

phenomena of Li ions in a solid. In this study, we calculated the rate capability of diluted electrodes using a charge–discharge simulation program and proved that the transport of Li ions in the solid phase is the rate-determining step for a diluted electrode with an extremely low active material content. In addition, the solid-state Li-ion diffusion coefficient can be calculated by analyzing the results of the rate capability tests. These results reveal that the diluted electrode method is very useful for elucidating the solid-state Li ion diffusion phenomena of lithium insertion materials. As such, the rate capability tests provide a new means of analyzing the solid-state diffusion coefficient.

Effect of Electronic Conductivity on the Polarization Behavior of Li[Li$_{1/3}$Ti$_{5/3}$]O$_4$ Electrodes

Kingo ARIYOSHI, Takaya INO, Yusuke YAMADA

J. Electrochem. Soc., Vol. 168, Article No. 070555 (7 pages) (2021).

Along with structural factors such as thickness and porosity, the conductive additive in lithium insertion electrodes in lithium-ion batteries influences the rate capability. The addition of a conductive additive improves the electronic conductivity of the electrodes, necessitating the optimization of such additives. However, the relationship of conductive additives to the electronic conductivity and rate capability of an electrode cannot be explained using classical electrochemical theory. The effect of the electronic conductivity of electrodes on polarization was investigated using Li[Li$_{1/3}$Ti$_{5/3}$]O$_4$−pellet electrodes, whose electronic conductivity can be modified using a graphite conductive additive during an oxidation/reduction reaction. Consequently, the polarization behavior of the Li[Li$_{1/3}$Ti$_{5/3}$]O$_4$−pellet electrodes without the conductive additive is asymmetric during the reduction and oxidation reactions, while it is symmetrical in the electrodes with the conductive additive. Furthermore, the polarization voltage is significantly lower in the electrodes with the conductive additive. Herein, we propose a rational explanation for the observed relationship between the electronic conductivity and polarization of electrodes using the formation and disappearance of electron conduction paths. This explanation would help us understand the enhancement of the rate capabilities of electrodes with poor electronic conductivity using conductive additives by the construction of the electron conduction paths.

Intragranular Fracture Mechanism of Highly Crystalline Lithium Manganese Oxide during Lithium Insertion/Extraction Reactions

Kingo ARIYOSHI, Nan UKUMORI

ACS Appl. Energy Mater., Vol. 4, pp. 8142-8149 (2021).

Lithium-ion batteries require long cycle lives for efficient automobile and stationary applications. Therefore, the lithium-insertion materials used as positive and negative electrodes in batteries need to be highly durable. Lithium insertion materials normally change their lattice dimensions during charge and discharge; therefore, particle fracture leading to the deterioration of the materials is one of the greatest hindrances to extending the cycle life. Despite its importance, no one has experimentally elucidated the fracture mechanism in detail. To avoid or suppress particle fracture, it is required to understand the fracture mechanisms, with an emphasis on the relationship between the change in lattice dimensions and the generation/propagation of cracks on the particles. In this study, we examined particle fracture phenomena using single-crystal LiMn$_2$O$_4$ (LMO) having an octahedral shape with a crystal size of ~5 μm. Accelerated cycle tests and overcharge tests revealed that during the lithium extraction reaction of LMO in the 4 V region, cracks are induced along the {111} fracture planes by stress corrosion cracking, wherein the acid generated by the decomposition of the electrolyte accelerates the crack propagation. During the lithium-insertion reaction of LMO in the 3 V region, wherein the structural transformation between the cubic and tetragonal lattices takes place, heavy cracks are caused by strong internal stresses at grain boundaries, {100} fracture planes at the cubic/tetragonal grain boundary, and {110} fracture planes at the tetragonal/tetragonal grain boundary. The results obtained herein suggest that crack patterns are closely related to the change in lattice dimensions for lithium-insertion materials. These findings provide useful insights into the development of lithium-insertion materials having excellent cyclability by designing particle morphology and size.

Synthesis Optimization of Electrochemically Active LiCoMnO$_4$ for High-Voltage Lithium-Ion Batteries

Kingo ARIYOSHI, Hiroya YAMAMOTO, Yusuke YAMADA

Energy Fuels, Vol. 35, pp. 13449-13456 (2021).

Lithium cobalt manganese oxide (LiCoMnO$_4$) with a spinel structure is considered to be a highly

advantageous positive electrode material for lithium-ion batteries, because of its high operating voltage (5 V), which enables it to achieve reversible capacities exceeding 120 mAh g^{-1}; however, oxygen deficiencies during high-temperature synthesis, associated with the reduction of Mn^{4+} ions, compromise the stoichiometric composition of the compound and limit its performance. To develop new strategies for preserving the stoichiometric composition of $LiCoMnO_4$ during synthesis, we analyzed its structural changes and oxygen release/uptake kinetics during the heating and cooling processes in the high-temperature region. At temperatures exceeding 900°C, transformation of the spinel structure into a rock salt like structure was revealed, because of the oxygen release from the crystal lattice. In addition, thermogravimetric analysis verified that the oxidation of $LiCoMnO_{4-\delta}$ was a diffusion-controlled reaction. Interpretation of the oxygen uptake kinetics allow us to optimize the $LiCoMnO_4$ synthetic conditions, where $LiCoMnO_4$ with a stoichiometric composition capable of excellent discharge capacity performance was obtained.

Clarification of Particle Size Dependence on the Rate Capabilities of $Li[Ni_{1/2}Mn_{3/2}]O_4$ Materials and Electrodes by the Dilute Electrode Method

Kingo ARIYOSHI, Jun SUGAWA, Shumpei MASUDA
J. Power Sources, Vol. 509, Article No. 230349 (8 pages) (2021).

Improving the rate capability of lithium insertion electrodes is essential for high-power lithium-ion batteries used in automobile applications. Several approaches have been studied to improve the rate capability of $Li[Ni_{1/2}Mn_{3/2}]O_4$ (LiNiMO); however, no consensus has been reached owing to conflicting results of particle size dependence on rate capability. Rate capability improvement has been obtained previously using nanosized particles as well as micron-sized particles. To solve this contradiction, we examined the dependence of particle size on rate capabilities of LiNiMO materials and electrodes using the diluted electrode method. This method allows us to measure two distinct rate capabilities of lithium insertion materials and electrodes. The rate capability of dilute-LiNiMO electrodes is improved by using nanosized particles, while that of conventional electrodes is improved by using micron-sized particles. This indicates two different rate-determining steps: Li-ion transport in LiNiMO particles for the dilute electrodes, and Li-ion diffusion in the electrolyte for the conventional LiNiMO electrodes. Moreover, the rate capability of the dilute-LiNiMO electrodes is superior to that of the conventional electrodes, indicating that Li-ion transport in LiNiMO particles is faster than Li-ion diffusion in an electrolyte with porous electrodes. These findings provide important insights for designing electrodes with excellent rate capabilities.

Light-Powered Autonomous Flagella-Like Motion of Molecular Crystal Microwires

Fei TONG, Daichi KITAGAWA, Ibraheem BUSHNAK, Rabih O. AL-KAYSI, Christopher J. BARDEEN
Angew. Chem. Int. Ed., Vol. 60(5), pp. 2414-2423 (2021).

The ability to exhibit life-like oscillatory motion fueled by light represents a new capability for stimuli-responsive materials. Although this capability has been demonstrated in soft materials like polymers, it has never been observed in molecular crystals, which are not generally regarded as dynamic objects. In this work, it is shown that molecular crystalline microwires composed of (*Z*)-2-(3-(anthracen-9-yl) allylidene)malononitrile can be continuously actuated when exposed to a combination of ultraviolet and visible light. The photo-induced motion mimics the oscillatory behavior of biological flagella and enables propagation of microwires across a surface and through liquids, with translational speeds up to 7 $\mu m\ s^{-1}$. This is the first example of molecular crystals that show complex oscillatory behavior under continuous irradiation. A model that relates the rotation of the transition dipole moment between reversible $E{\rightarrow}Z$ photoisomerization to the microscopic torque can qualitatively reproduce how the rotational frequency depends on light intensity and polarization.

Fast T-Type Photochromic Crystals of Diarylbenzene

Shota HAMATANI, Daichi KITAGAWA, Seiya KOBATAKE
J. Phys. Chem. C, Vol. 125(8), pp. 4588-4594 (2021).

Photochromic molecules are of great interest as light-driven molecular switches in research fields of material and life sciences. In particular, fast T-type photochromic molecules with half-life times of the thermal back reaction ($t_{1/2}$) on the order of milliseconds can change not only their color but also their physicochemical properties only under photoirradiation. Herein, we report fast T-type photochromic crystals with the $t_{1/2}$ on the order of milliseconds composed of a diarylbenzene by utilizing intramolecular CH−N hydrogen bonding

interactions. Our results would lead to novel photoresponsive crystalline materials whose color and physicochemical properties can be modulated only under photoirradiation.

Anisotropic Bending and Twisting Behaviour of a Twin Crystal Composed of a Diarylethene

Takuya HIGASHIGUCHI, Daichi KITAGAWA, Seiya KOBATAKE

CrystEngComm, Vol. 23, pp. 5795-5800 (2021).

Photomechanical materials efficiently transform light energy directly into mechanical energy even at extremely low temperatures, in water, and under vacuum. In particular, photomechanical crystals have potential to be used as functional actuators driven by photon energy for the next generation. Here, we found that crystals consisting of 1,2-bis(2-methyl-5-(4-undecyloxyphenyl)-3-thienyl)perfluorocyclopentene exhibit unusual photomechanical bending. Upon irradiation with ultraviolet light, the crystal bent toward the incident light, but the velocity of the bending depended on the illumination directions. When irradiated from the left and right sides of the crystal, the velocities of the bending were different from each other. We found that the crystal is a "twin crystal", as confirmed by X-ray crystallography. The bending mechanism of the twin crystal can be interpreted from the content of twin components, the absorption anisotropy of diarylethene molecules and the degree of the crystal twisting.

Light-Driven Rapid Peeling of Photochromic Diarylethene Single Crystals

Masato TAMAOKI, Daichi KITAGAWA, Seiya KOBATAKE

Cryst. Growth Des., Vol. 21(5), pp. 3093-3099 (2021).

Macroscopic transformation such as the molecular motors of biology is brought by transforming the protein using the chemical reaction of molecules by external stimuli. If it is possible to achieve it as machine-like in nanometer to micrometer size in photomechanical phenomena, there is a possibility of the application as driving devices of micro- or nanomachineries that drive without any electrical contact. Since light is useful to operate it without any direct contact as external stimuli and leads to rapid photochemical reactions, the operation at high speed can be expected. Here we newly found that crystals of a photochromic diarylethene exhibit a peeling behavior with astonishingly rapid velocity by photoirradiation to a lateral face in addition to separation behaviors such as jumping and cracking by photoirradiation to a well-developed face. The detail of the rapid photoresponsive peeling was discussed based on the molecular packings and the dependence on crystal size and photoirradiation conditions. These crystals can be potentially applied to macroscopic photomechanical actuators rapidly driven based on molecular machinery.

Rational Design of Photochromic Diarylbenzene with both High Photoreactivity and Fast Thermal Back Reactivity

Rikuto MAEGAWA, Daichi KITAGAWA, Shota HAMATANI, Seiya KOBATAKE

New J. Chem., Vol. 45(40), pp. 18969-18975 (2021).

Recently, diarylbenzenes (DABs) have been developed as a new family of T-type photochromic molecules. In this work, we newly designed and synthesized DABs for the creation of molecules with both high photoreactivity and fast thermal back reactivity. Utilizing the intramolecular CH–N hydrogen bonding and the bulky substituents at the reactive carbons resulted in the enhancement of photoreactivity and the acceleration of the thermal back reaction rate. Furthermore, we demonstrated that the high photoreactivity resulted in much better coloration compared with that of the previously reported DAB even at a lower concentration. These results would not only provide a strategy for molecular design but also be useful for the development of materials with less environmental load.

Photochromism

Seiya KOBATAKE

Progress in the Science of Functional Dyes, Eds.: Y. OOYAMA, S. YAGI, Springer, Singapore, pp. 263-281 (2021)

Photochromic compounds can be divided into two types, T- and P-types. T-type photochromic compounds include azobenzene, spiropyran, hexaarylbiimidazole, spirooxazine, naphthopyran, and the donor-acceptor Stenhouse adduct, as introduced here. In P-type photochromic compounds, there are furylfulgide and diarylethene. Diarylethene derivatives have the most excellent photochromic compounds, such as thermal stability of both isomers, high fatigue-resistance, high response, high sensitivity, high coloration quantum yield, and high reactivity even in the crystalline phase. In this chapter, the photochromic properties of these compounds have been focused.

Microstructure Formation on Poly (Methyl Methacrylate) Film Using Atmospheric Pressure Low-Temperature Plasma
Atsushi SEKIGUCHI, Hiroko MINAMI, and Hideo HORIBE
J. Photopolym. Sci. Technol. 34(4), pp385-392 (2021)
This study targets development of a biomimetic technique for mitigating endoscope surface antifouling. We specifically examined a snail's shuck, which has convexo-concave microstructures, to achieve an antifouling function. Unfortunately, fabricating microstructures on lens surfaces entails large costs because of technical difficulties. As one alternative method, we fabricated microstructures on films with different PMMA concentrations and examined their surface profiles using atmospheric pressure low-temperature plasma. Convex structures on a low (67.4 wt%) PMMA concentration film have a rounded tip at high RF power. When RF power is low, however, structures fabricated on a 67.4 wt% PMMA film surface were more incisive and orderly than those on a 84.4 wt% PMMA film. Microstructures with 200-nm pitch, like a snail's shuck, were fabricated on a 67.4 wt% PMMA film when irradiating plasma at 52 W for 40 s.

Removal of Novolac Photoresist with Various Concentrations of Photo-active Compound Using H_2/O_2 Mixtures Activated on a Tungsten Hot-wire Catalyst
Koki AKITA, Shota SOGO, Ryusei SOGAME, Masashi YAMAMOTO, Shiro NAGAOKA, Hironobu UMEMOTO, and Hideo HORIBE
J. Photopolym. Sci. Technol. 34(5), pp499-504 (2021)
We earlier reported that addition of a small amount of O_2 gas in the atmosphere where H radicals are generated on a high-temperature tungsten filament improves the photoresist removal rate of positive-tone novolac photoresists for i/g lines. This study investigated effects of photo-active compound (PAC) on the photoresist removal. Addition of more than 1.5 sccm of oxygen to 100 sccm of hydrogen gas flow decreased the removal rate. In pure novolac resin, cross-linking of the resin can be one of the causes of this decrease at temperatures higher than 240 °C. The rate of removal with PAC decreased much more than with pure novolac resin over 240 °C. This removal rate decrease might be ascribed to cross-linking not only between the resin and the PAC but also between the resins. OH radicals can be used effectively for photoresist removal by generating sufficient H radicals to prevent such cross-linking.

Development of Bile Direct Stent Having Antifouling Properties by Atmospheric Pressure Low-Temperature Plasma
Atsushi SEKIGUCHI, Masashi YAMAMOTO, Takuya KUMAGAI, Youichiro MORI, Hiroko MINAMI, Kimiyasu AIKAWA, and Hideo HORIBE
J. Photopolym. Sci. Technol. 34(4), pp401-410 (2021)
Biomimetics (or biomimicry) is a field of technologies based on imitating various functions and properties of organisms. Waterproof products, which are inspired by lotus leaves with super-water-repellent fine structures, are a well-known example of biomimetics. The present study examined the surface structure of snail shells, which exhibit oil repellency (oleophobic property). Snail shells have nanoporous structures with nanoholes on the scale of 200–400 nm. When water enters these nanoholes, the surface is covered by thin water films. The oil can be repelled by the water film.   These structures are known as superhydrophilic nanostructures. An earlier report discussed our efforts to create such nanostructures using a nanoimprinting method and assessed the feasibility of application to the inner walls of biliary stents. This involves a labor-consuming two-stage process involving creating nanostructures on a film surface, then rolling the film into a tube. In addition, the nanoimprinting mold made via electron beam lithography is costly and unsuitable for mass production. To overcome these issues, we sought to develop elemental technologies for providing antifouling properties to biliary stents, which are made of polyethylenes (PEs), by forming nanostructures directly on the inner surface, using atmospheric pressure low-temperature plasma. We formed nanostructures on the inner walls of PE tubes of varying diameters under varying plasma conditions. We then examined the resulting structures and effects of the antifouling properties thus imparted.

Improvement of Resist Characteristics by Synthesis of a Novel Dissolution Inhibitor for Chemically Amplified Three-Component Novolac Resist
Sinya AKECHI, and Hideo HORIBE
J. Photopolym. Sci. Technol. 34(5), pp491-494 (2021)

A photosensitive polymer called photoresist is used to create fine circuit patterns on the surface of semiconductors. The aim of this study was to improve the resist function by incorporating a chemical amplification mechanism into the base polymer, novolac resin. The resist is composed of three components: base polymer, dissolution inhibitor (DI), and photoacid generator. The ability to inhibit the dissolution of resist polymer in the unexposed area was improved by increasing the molecular size of DI. The high acidity of deprotected DI with carboxyl groups improved the ability to promote dissolution of resist polymer in the exposed area. The resists containing DIs with large molecular size and high acidity showed improved resolution.

Influence of Glycerol in Developer on Novolak-Type Positive-Tone Resist Solubility

Shunpei KAJITA, Yukiko MIYAJI, and Hideo HORIBE
Photoresist is used for circuit fabrication in semiconductor devices. The material generally used for manufacturing semiconductor devices is the novolak-type positive-tone resist; however, it is necessary to minimize its line width while improving the resolution. To improve the resolution of novolak-type positive-tone resist, in this study, developers containing water-soluble organic solvents or surface-activating agents have been designed for controlling the resist solubility. The addition of glycerol, as a water-soluble organic solvent in the developer, inhibits the dissolution of the novolak resist, particularly in the unexposed area. The developer containing glycerol improves the novolak resist resolution, thereby developing a fine pattern.

Effect of pH on Decomposition of Organic Compounds Using Ozone Microbubble Water

Kazuki TSUJIMOTO, and Hideo HORIBE
Microbubbles are tiny bubbles with a particle size of 1 - 100 μm. Microbubbles have been reported that the gas dissolving ability is excellent and hydroxyl radical generates when microbubbles collapse in water. On the other hand, ozone is a gas with high oxidation power and eventually decomposes into oxygen. So, ozone is environmentally friendly. Therefore, we thought that ozone microbubbles water, in which ozone is dissolved in microbubbles water, could be used to efficiently decompose persistent organic compounds while being environmentally friendly. In this study, we evaluated the decomposition of phenol, an object subject to wastewater regulation, by ozone water and ozone microbubbles water. At a constant dissolved ozone concentration, we could not confirm the effect of microbubbles in decomposing phenol. Also, under the same conditions, when the pH was changed, the effect of microbubbles could not be confirmed. However, under basic conditions, phenol was decomposed the most because of self-decomposition reaction of ozone. Therefore, the effect of microbubbles could not be confirmed in the phenol degradation by ozone microbubbles in this experiment.

Enhanced decomposition of toxic pollutants by underwater pulsed discharge in the presence of hydrogen peroxide and microbubbles

Risako MATSUURA, Noritsugu KOMETANI, Hideo HORIBE, and Tatsuru SHIRAFUJI
The decomposition of phenol and 4-chlorophenol by underwater pulsed discharge has been examined. The addition of hydrogen peroxide improved the decomposition rate of phenol by about 2.5 times and that of 4-chlorophenol by about 1.5 times. Analysis using a fluorescent probe suggested that the addition of hydrogen peroxide enhanced the production of hydroxyl radicals by about 3 times. We have also examined the effect of using microbubbles on the decomposition of phenol. The use of only microbubbles resulted in a slight increase of the decomposition rate, while the use of both microbubbles and hydrogen peroxide led to a remarkable enhancement of the decomposition rate by about 3.5 times with the conversion of phenol reaching 70% at discharge time of 3 hours, which corresponded to the energy yield of 4.39×10^{-9} mol/J.

Thermo- and Photoresponsive Behaviours of Dual-Stimuli-Responsive Organogels Consisting of Homopolymers of Coumarin-Containing Methacrylate

Seidai OKADA and Eriko SATO
Coumarin-containing vinyl homopolymers, such as poly(7-methacryloyloxycoumarin) (**P1a**) and poly(7-(2'-methacryloyloxyethoxy)coumarin) (**P1b**) show a lower critical solution temperature (LCST) in chloroform, which can be controlled by the [2+2] photochemical cycloaddition of the coumarin moiety, and they are

recognized as monofunctional dual-stimuli-responsible polymers. A single functional group of monofunctional dual-stimuli-responsive polymers responds to dual stimuli and can be introduced more uniformly and densely than those of dual-functional dual-stimuli responsive polymers. In this study, considering a wide range of applications, organogels consisting of **P1a** and **P1b**, i.e., **P1a-gel** and **P1b gel**, respectively, were synthesized, and their thermal- and photo-responsive behaviours in chloroform were investigated in detail. **P1a-gel** and **P1b-gel** in a swollen state (transparent) exhibited phase separation (turbid) through a temperature jump and reached a shrunken state (transparent), i.e., an equilibrium state, over time. Moreover, the equilibrium degree of swelling decreased non-linearly with increasing temperature. Furthermore, different thermoresponsive sites were photopatterned on the organogel through the photodimerization of the coumarin unit. The organogels consisting of homopolymers of coumarin-containing methacrylate exhibited unique thermal- and photo-responsivities and behaved as monofunctional dual-stimuli-responsive organogels.

Synthesis and Dissociation Behavior of Degradable Network Polymers Consisting of Epoxides and 9-Anthracene Carboxylic Acid Dimer
Kinuka TANO and Eriko SATO
Chem. Lett., Vol. 50(10), pp. 1787-1790 (2021)
Photodimer of 9-anthracene carboxylic acid was used as crosslinker for bisepoxides and a degradable network polymer was synthesized at 100–110 °C in the presence of a base catalyst. The resulting network polymer was thermally decrosslinked at 150 °C within 30 min and completely solubilized in an organic solvent. Detailed investigation of the thermal dissociation behavior revealed that dissociation of more than 80% of 9-AC dimer unit was required for complete solubilization of the network polymer.

Development of Synthesis Technology of Metal Nanoparticles by Hydrothermal Method
Noritsugu KOMETANI
Synthesis of Metal Nanoparticles / Structural Control, Pasting and Latest Application, R&D Support Center, pp. 57-71 (2021) (in Japanese)

Investigation of OECD 301F ready biodegradability test to evaluate chemical fate in a realistic environment
Saki TAKEKOSHI, Kotaro TAKANO, Yoshihide MATOBA, Masayuki SATO, Akira TACHIBANA
J. Pestic. Sci. Vol.46, pp.143-151. (2021)
The OECD 301F ready biodegradability test has been approved for use under the Japanese Chemical Substances Control Law since 2018. This test uses activated sludge obtained from a sewage treatment plant instead of the standard activated sludge used for the 301C test. In addition, the test is allowed to add an inert support or emulsifying agent, and/or to change the volume of the test medium. In this study, we first confirmed that the standard sludge had lower biodegradation activities than the sludge taken from a sewage treatment plant. Second, we showed that biodegradation percentages were increased by adding suitable amounts of silica gel or Tween 80. Third, we found that the biodegradations were accelerated by only increasing the medium volume under the conditions that concentrations of chemical, silica gel, and sludge were held constant. These findings are expected to contribute to the appropriate evaluation of chemical fate in a realistic environment.

Evaluating β-1,3-glucan synthesis inhibition using emulsion formation as an indicator
Shinsuke NEROME, Naoki YOKOTA, Yoshihiro OJIMA, Masayuki AZUMA
J. Microbiol. Methods, 190: 106327 (2021)
Introduction
The cell wall β-1,3-glucan of fungal pathogen *Candida albicans* is an attractive antifungal target. β-1,3-Glucan is the skeletal structure in the cell wall and the major scaffold for cell wall proteins. In previous studies using *Saccharomyces cerevisiae*, strong emulsification was detected by mixing cell wall proteins with oil. To date, there have been no reports of applying an emulsification phenomenon to assessing β-1,3-glucan synthesis inhibition.
Objective
The aim of this study was to clarify that emulsification is useful as an indicator for evaluating β-1,3-glucan synthesis inhibition in *C. albicans*.
Methods
At first, whether cell wall proteins released from cells by β-1,3-glucanase treatment worked as an effective emulsifier in *C. albicans* was examined. Next, whether emulsification occurred even in the culture supernatant

brought about by treating with bioactive compounds, including β-1,3-glucan synthesis inhibitors, under osmotic protection was investigated. In addition, the release of cell wall proteins into the culture medium by treating with those compounds was examined. Finally, a simpler evaluation method using emulsion formation was examined for application to screening of inhibitors.

Protein engineering of D-succinylase from *Cupriavidus* sp. for D-amino acid synthesis and the structural implications

Yosuke SUMIDA, Masayuki YAMASAKI, Yoshiaki NISHIYA, Shinya KUMAGAI, Toshihide YAMADA, Masayuki AZUMA

Adv. Synth. Catal., Vol. 363, No. 20, pp. 4770-4778 (2021)

D-Amino acids are important chiral building blocks for pharmaceuticals and agrochemicals. Previously, we have used D-Succinylase (DSA) from *Cupriavidus sp*. P4-10-C and *N*-succinyl amino acid racemase (NSAR, EC.4.2.1.113) from *Geobacillus stearothermophilus* NCA1503 to produce D-amino acids via the dynamic kinetic resolution of *N*-succinyl-DL-amino acids. However, the use of this bioconversion system remains challenging for industrial application due to the insufficient enantioselectivity of DSA toward *N*-succinyl-D-amino acids. Therefore, we screened DSA mutants for improved enantioselectivity by directed evolution. Several mutants showed improved enantioseletivity compared to wild-type DSA. L182E mutant had superior enantioselectivity, and the thermal stability was also remarkably improved by this single mutation. We solved the crystal structure of the L182E mutant in complex with succinic acids at a resolution 2.0 Å. The mutated residues in all generated mutants that showed improved enantioselectivity (including the substituted Glu182 in the L182E mutant) are found very close to the active site. The solved crystal structure also provides some rationale to explain the higher thermostability of the L182E mutant compared to wild-type DSA. D-phenylalanine and D-tryptophan were produced in high conversion (approximately 90%) with 98.8% *ee* and 99.6% *ee*, respectively, using coupled L182E DSA and NSAR with the one-pot enzymatic method. These data suggested that L182E DSA may be a useful biocatalyst for industrial D-amino acids production.

Aberrant membrane structures in hypervesiculating *Escherichia coli* strain Δ*mlaE*Δ*nlpI* visualized by electron microscopy

Yoshihiro OJIMA, Tomomi SAWABE, Mao NAKAGAWA, Yuhei O. TAHARA, Makoto MIYATA, Masayuki AZUMA

Front. Microbiol., 12: 706525 (2021)

Escherichia coli produces extracellular vesicles called outer membrane vesicles (OMVs) by releasing part of its outer membrane. We previously reported that the combined deletion of *nlpI* and *mlaE*, related to envelope structure and phospholipid accumulation in the outer leaflet of the outer membrane, respectively, resulted in the synergistic increase of OMV production. In this study, the analysis of Δ*mlaE*Δ*nlpI* cells using quick-freeze, deep-etch electron microscopy (QFDE-EM) revealed that plasmolysis occurred at the tip of the long axis in cells and that OMVs formed from this tip. Plasmolysis was also observed in the single-gene knockout mutants Δ*nlpI* and Δ*mlaE*. This study has demonstrated that plasmolysis was induced in the hypervesiculating mutant *E. coli* cells. Furthermore, intracellular vesicles and multilamellar OMV were observed in the Δ*mlaE*Δ*nlpI* cells. Meanwhile, the secretion of recombinant GFP expressed in the cytosol of the Δ*mlaE*Δ*nlpI* cells was more than 100 times higher than that of WT and Δ*nlpI*, and about 50 times higher than that of Δ*mlaE* in the OMV fraction, suggesting that cytosolic components were incorporated into outer-inner membrane vesicles (OIMVs) and released into the extracellular space. Additionally, QFDE-EM analysis revealed that Δ*mlaE*Δ*nlpI* sacculi contained many holes noticeably larger than the mean radius of the peptidoglycan pores in wild-type *E. coli*. These results suggest that in Δ*mlaE*Δ*nlpI* cells, cytoplasmic membrane materials protrude into the periplasmic space through the peptidoglycan holes and are released as OIMVs.

Carbohydrate 3'-Sialyllactose as a Novel Target for Theranostics in Pancreatic Ductal Adenocarcinoma.

Kiyoshi HIGASHI, Keiko MAEDA, Kaori MIYATA, Saori YOSHIMURA, Keita YAMADA, Daijiro KONNO, Taro TACHIBANA, Koichi SAITO

Tumor Biology, Vol.42, pp.1-9 (2020).

We previously demonstrated that the carbohydrate 3'-sialyllactose is overexpressed in cancer stem-like cells such as metastatic pancreatic and poorly differentiated gastric cancer cells, and undifferentiated human embryonic stem cells. In this study, we investigated the possibility of 3'-sialyllactose as a target for theranostics in cancers using a recombinant mouse monoclonal antibody r3B1E2 that binds to 3'-sialyllactose. Immunohistochemistry analysis confirmed an elevated expression of 3'-sialyllactose in tumors of pancreas,

stomach, and testis, while no expression of 3'-sialyllactose was observed in corresponding normal controls. In addition, a stage-independent expression of 3'-sialyllactose was observed, especially in pancreatic ductal adenocarcinoma (PDAC). The level of serum 3'-sialyllactose in PDAC subjectswas significantly higher than that in healthy controls, providing excellent AUC of 0.88. We next explored the therapeutic potential of r3B1E2 for PDAC in vitro. Treatment of r3B1E2 with 3#-sialyllactose-bearing human PDAC cells exhibited a complement-dependent cytotoxicity, whereas no significant activity of r3B1E2 against 3'-sialyllactose-negative cells was observed. Collectively, these findings raise the possibility of 3#-sialyllactose as a novel target for theranostics in PDAC.

Canopy Homolog 2 as a Novel Molecular Target in Hepatocarcinogenesis.
Anna KAKEHASHI, Shugo SUZUKI, Masayuki SHIOTA, Nina RAYMO, Min GI, Taro TACHIABANA, Vasily STEFANOV, Hideki WANIBUCHI.
Cancers, Vol.13, 3613 (2021).
In the present study, the role of a novel protein involved in neurite development and endoplasmic reticulum (ER) stress, canopy homolog 2 (CNPY2), was investigated in mouse and human hepatocarcinogenesis. Firstly, a sensitive quantitative and qualitative detection of protein expression using QSTAR Elite LC-Ms/Ms was performed for the analysis of lysates of microdissected hepatocellular altered foci (AF), adenomas (HCAs), carcinomas (HCCs) and peri-tumoral livers from C57Bl/6J mice treated with diethylnitrosamine (DEN) and then maintained for 27 or 38 weeks on basal diet. Significant overexpression of 18.5 kDa CNPY2 processed form was demonstrated in AF, HCAs and HCCs, while low expression was observed in the livers of DEN-treated and control mice. Furthermore, CNPY2 elevation in AF and tumors was coordinated with accumulation of numerous cytoskeletal proteins, including cytokeratins 8 and 18, actin, non-muscle myosin and septin 9 and those involved in ER and mitochondrial stresses such as calreticulin, prohibitins 1 and 2 and YME1-like-1. Knockdown of CNPY2 in Huh7 and HepG2 human liver cancer cells resulted in significant suppression of cell survival and invasive potential, inhibition of cyclin D1, induction of p21$^{Waf1/Cip1}$ and suppression of the apoptosis inhibitor Bcl2. In contrast, transfection of a mouse CNPY2 (mCNPY2-Ds-Red) vector plasmid in Huh7 and HepG2 cancer cells, with subsequent accumulation of CNPY2 in the ER, resulted in significant increase in cancer cells survival. Clinicopathological analysis in 90 HCV-positive HCC patients, revealed significant association of CNPY2 overexpression with poor overall ($p = 0.041$) survival. Furthermore, CNPY2 increase was associated with vessel invasion ($p = 0.038$), poor histological differentiation ($p = 0.035$) and advanced clinical stage ($p = 0.016$). In conclusion, CNPY2 is a promising molecular target elevated early in hepatocarcinogenesis and prognostic marker for human HCV-associated HCC. CNPY2 is involved in the processes of ER stress, cell cycle progression, proliferation, survival and invasion of liver tumor cells.

Simultaneous analyses of the rates of photoinduced charge separation and recombination between the excited flavin and tryptophans in some flavoproteins: Molecular dynamics simulation
Kiattisak LUGSANANGARM, Haruhiko TAMAOKI, Yasuzo NISHINA, Masaya KITAMURA, Nadtanet NUNTHABOOT, Fumio TANAKA, Seiji TANIGUCHI, and Haik CHOSROWJAN
AIP Advances, Vol. 10, Article No. 105224 (14 pages) (2020)
Ultrafast transient absorption (TA) spectroscopy has been one of the most powerful experimental tools to study the mechanism of photoinduced electron transfer (ET) as in photosynthetic and flavin photoreceptor systems in plants. However, no work has been reported on their quantitative mechanisms. Apparent rates of charge separation (CS) from tryptophans (Trps) to the excited isoalloxazine (Iso*) and charge recombination (CR) from the produced ion pairs to Trps and Iso in the ground states are reported to be 0.25 ps and 3.2 ps in medium-chain acyl-CoA dehydrogenase (MCAD), and 0.15 ps and 6.6 ps in flavin mononucleotide binding protein (FMN-bp), obtained by an ultrafast TA method. The decays of the CS and CR processes were for the first time simultaneously analyzed with an ET theory and structures obtained by molecular dynamics simulation. MCAD and FMN-bp form a tetramer and dimer, respectively. The CS and CR rates of an individual donor and various related physical quantities were numerically obtained. It was found that both CS and CR rates were fastest from Trp166 among four Trps in MCAD and those from Trp106 among two Trps in FMN-bp. Logarithmic CS rates in MCAD were dependent on the donor–acceptor distance (Rc) with parabolic functions, while those of CR rates linearly decreased with Rc. Reasons why CS rates were faster than CR rates in both MCAD and FMN-bp were elucidated in terms of pre-exponential factors in the theory. The present method could be useful to understand the precise mechanisms of initial steps of biological functions of photoreceptors in plants.

Control of crystal size distribution and polymorphs in the crystallization of organic compounds
Koichi IGARASHI and Hiroshi OOSHIMA
Advances in Organic Crystal Chemistry, Eds.: M. SAKAMOTO, H. UEKUSA, Springer, Singapore, pp. 81-94 (2020)
Many of organic compounds, such as pharmaceuticals and chemicals, are produced as crystals. Controlling the characteristics of these crystal products with good reproducibility is essential for crystallization of organic compounds. There are various characteristics to be controlled, such as grain size and distribution, crystal polymorphism, crystal habit, and purity, but grain size and crystal polymorphism are particularly essential characteristics. In order to control them, the authors have developed several new crystallizers. This chapter highlights some recent crystallizers to produce organic crystals with high quality.

Polymorphic Crystallization Design to Prevent the Degradation of the β-Lactam Structure of a Carbapenem
Shinji MATSUURA, Koichi IGARASHI, Masayuki AZUMA and Hiroshi OOSHIMA
Crystals, 11, 931 (2021)
The cooling crystallization of carbapenem CS-023 was performed at 25 °C in an aqueous solution. Tetrahydrate crystals (form H) were obtained. Hydrate crystals are promising drugs, but there has been problems in manufacturing such crystals. During cooling crystallization, a dissolution process at a high temperature of 70 °C was utilized. The main problem in manufacturing was that the degradation rate of CS-023 at 70 °C was high, as expressed in the half-life period of 2.97 h. Poor solvent crystallization using ethanol was observed at 25 °C. Thus, a different polymorph (Form A) was obtained. Form A comprised CS-023, 5/2 ethanol, and 1/2 H_2O. Form A, containing ethanol, is not suitable as a drug. Form A was then transformed to another polymorph of hydrate crystals or tetrahydrate Form H. Another hydrate polymorph, Form B, was obtained through the solid phase transformation of Form A and further transformed to the tetrahydrate Form H, at high humidity over 80% RH. This process, which proceeded at the low temperature of 25 °C, helped to prevent the degradation of CS-023, thereby avoiding wastage. Furthermore, the solid-phase transition could be controlled with vapor composition.

Mechanism Toward Turn-on of Polysaccharide−Porphyrin Complexes for Fluorescence Probes and Photosensitizers in Photodynamic Therapy in Living Cells
Shodai HINO, Rikushi FUNADA, Kouta SUGIKAWA, Riku KAWASAKI, Kazuya KOUMOTO, Toshio SUZUKI, Takeshi NAGASAKI, Atsushi IKEDA
ChemMedChem, Vol.16, pp. 793-803 (2021).
$β$ -(1,3-1,6)-D-Glucan, λ-carrageenan, tamarind gum, and pullulan can dissolve various porphyrin derivatives via the formation of complexes in water using a high-speed vibration milling method. The aqueous solutions of the resulting complexes exhibit long-term stability. Despite the adverse effects of the self-quenching process, notable fluorescence and improved photodynamic activity of the polysaccharide-complexed porphyrin derivatives were observed in the presence of liposomes, micelles, cyclodextrins, and HeLa cells. It was noted that the type of porphyrins was more important than the type of polysaccharides present in the complex. Porphyrin self-aggregates were monodispersed in the lipid membranes of the liposomes and lysosomes. The polysaccharide-complexed porphyrin derivatives showed increased photodynamic activity toward HeLa cells under photoirradiation between 610 and 740 nm.

Tumor Growth Suppression with Novel Intra-Arterial Chemotherapy Using Epirubicin-Entrapped Water-in-Oil-in-Water Emulsion In Vivo
Hironobu YANAGIE, Takashi FUJINO , Masashi YANAGAWA, Toshimitsu TERAO, Takashi IMAGAWA, Mitsuteru FUJIHARA, Yasuyuki MORISHITA, Ryouji MIZUMACHI, Yuuji MURATA, Novriana DEWI, Yuuya ONO, Ichiro IKUSHIMA, Koji SEKIGUCHI, Masashi NAGATA, Yasumasa NONAKA, Yoshitaka FURUTA, Tomoyuki HISA, Takeshi NAGASAKI, Kazuhiko ARIMORI, Tadao NAKASHIMA, Takumichi SUGIHARA, Kazuhiro KAKIMI, Minoru ONO, Jun NAKAJIMA, Masazumi ERIGUCHI, Shushi HIGASHI, Hiroyuki TAKAHASHI
In Vivo, Vol.35, pp. 239-248 (2021).
A mixture of anticancer agents and iodized poppy seed oil (IPSO) has been widely used for intra-arterial chemotherapy of hepatocellular carcinoma. However, the anticancer agents can easily separate from IPSO, so the therapeutic potential is limited. We developed epirubicin-entrapped water-in-oil-in-water emulsion (WOW-Epi) using a double-membrane emulsification technique. We delivered WOW-Epi through a hepatic

arterial injection to VX2 hepatic tumor rabbit model (1.2 mg/kg). VX2 tumor growth was selectively suppressed in the WOW-Epi-treated group compared with the control treated groups. The accumulation of WOW in nearby cancer cells was confirmed via electron-microscopy. Endocytosis seemed to be the mechanism underlying the uptake of WOW. Conclusion: WOW-Epi led to tumor growth suppression in vivo. WOW does not cause toxicity to arterial vessels. WOW-Epi will be hopefully used for repeated intra-arterial chemotherapy to HCC patients in the near future.

Tumor-Targeting Hyaluronic Acid/Fluorescent Carborane Complex for Boron Neutron Capture Therapy
Keita YAMANA, Riku KAWASAKI, Yu SANADA, Anri TABATA, Kaori BANDO, Kouhei YOSHIKAWA, Yoshinori SAKURAI, Shin-ichiro MASUNAGA, Minoru SUZUKI, Kouta SUGIKAWA, Takeshi NAGASAKI, Atsushi IKEDA
Biochim. Biophys. Res. Commun., Vol.559, pp. 210-216 (2021).
In cancer therapeutics, boron neutron capture therapy (BNCT) requires a platform for selective and efficient 10B delivery into tumor tissues for a successful treatment. However, the use of carborane, a promising candidate with high boron content and biostability, has significant limitations in the biomedical field due to its poor water-solubility and tumor-selectivity. To overcome these hurdles, we present in this study a fluorescent nano complex, combining fluorescent carborane and sodium hya-luronate for high boron concentration and tumor-selectivity. Tumor cells actively internalized the complex through binding hyaluronan to CD44, overexpressed on the tumor cell surface. Furthermore, the subcellular distribution of this complex could also be detected due to its fluorescent properties. More-over, after thermal neutron irradiations, the complex produced excellent cytotoxicity, equal to or greater than that of the clinically-used BPA-fructose. Therefore, this novel complex could be potentially more suitable for BNCT than the boron agent.

Cancer-Targeting Hyaluronic Acid/Carboranyl Pyrene Complex for Boron Neutron Capture Therapy
Keita YAMANA, Riku KAWASAKI, Yu SANADA, Shin-ichiro MASUNAGA, Minoru SUZUKI, Yoshinori SAKURAI, Anri TABATA, Kaori BANDO, Kouhei YOSHIKAWA, Kouta SUGIKAWA, Takeshi NAGASAKI, Atsushi IKEDA
KURNS Progress Report 2020, PR1-4 (2021).

Architecture and Building Engineering

PREDICTION METHOD OF ULTIMATE SEISMIC RESISTANCE CAPACITY LEVEL FOR PORTAL TYPE PLANE LATTICE STRUCTURES A ND CHARACTERIZ A TION FACTOR

Yutaro ARITA and Yoshiya TANIGUCHI
Journal of Structural Engineering, Vol.67B, March 2021, 189–196

This paper focuses on the elasto plastic behavior of static and dynamic responses for portal type plane lattice structures, which are subjected to vertical and horizontal loads. The purpose is to make clear the relationship between seismic responses and static responses and to estimate ultimate seismic resistance capacity levels with the information of static elasto plastic behavior. The static response compared is the relationships between equivalent velocities of energies and displacements. The dynamic response compared is that between earthquake input acceleration PGA and equivalent velocities of strain energies.

EFFECT OF ADDITIONAL HANGER RODS ON SEISMIC RESPONSES FOR CEILING SUSPENDED BY DIAGONAL CABLES

Kentaro MATSUSHITA, Susumu YOSHINAKA and Yoshiya TANIGUCHI
Journal of Structural Engineering, Vol.67B, March 2021, 219–224

In 2011, many conventional suspended ceilings hanged from roofs at high places were fallen by the Great East Japan earthquake and some measures have been required. We proposed a new ceiling suspended by diagonal cables. These cables behave as brace members on the condition that the weight of ceiling board gives cables tensile forces under the gravity load. It was showed that horizontal response of a ceiling suspended by diagonal cables was smaller than that of a conventional suspended ceiling, but vertical response was larger because of non-liner property of cable which cannot resist in compression. Considering these results, we suggest combination of diagonal cables and hanger rods as hanging member. We call this ceiling HC (hanger rods and cables) ceiling. Cables work to reduce horizontal responses and hanger rods arranged 4 edges of a ceiling work to suppress upward responses. The purpose of this paper is to study effects of hanger rods on seismic responses for ceiling suspended by diagonal cables, and study how responses of HC ceiling are different depending on the ratio of a number of hanger rods and cables parameterized by area of a ceiling. We confirmed that vertical acceleration of this ceiling is smaller than that of ceiling suspended by diagonal cables.

SEISMIC REINFORCEMENT OF AN ARCH MODEL USING NON-COMPRESSION ELEMENTS

Susumu YOSHINAKA and Yoshiya TANIGUCHI
Journal of Structural Engineering, Vol.67B, March 2021, 151–159

In recent major earthquakes, there have been many cases of buckling and fracture of substructure braces and diagonal roof braces in gymnasia. This paper proposes a new seismic reinforcement method for an arch model using non-compression elements such as cables. For spatial structures such as beam string structures, cables are generally used to decrease deformation and stress under static loading. In this study, we use cables to suppress deformations and stresses under dynamic loading. This has an advantage over the conventional reinforcement method using braces, because the structural members are slender because buckling does not need to be taken in account. We focus on the specific nonlinear vibration characteristics resulting from the material nonlinearity of the cables. Firstly, we study the basic vibration characteristics of a nonlinear model by a two-degree-of-freedom model including non-compression elements. Next, we propose two reinforcement methods using cables for an arch model and study their influence on seismic response.

Causes and effects of partial cooling use during sleep

Noriko UMEMIYA, Yuhan CHEN and Ikuna FUJIMOTO
Proceedings of the 11th Windsor Conference, Windsor, 1210-1217, 2020.

Causes and effects of partial cooling use during sleep were surveyed during 616 nights based on responses of 142 Osaka apartment residents. 137 nights of partial cooling use and 209 nights of full-time cooling use were compared. Results revealed the following. 1) The thermal environment of the outside air was not related. 2) Heat and cold tolerance of the respondents were not related, but easy perspiration and poor circulation caused partial cooling. 3) Partial cooling users had less stress, lower income, stronger environmental consciousness

and habits of more frequent clothing control. 4) Dwelling units of partial cooling users were less sunny, more efficient in cooling, stronger in thermal insulation, less condensed, and lower on living floors. 5) Bedrooms of partial cooling users had better views, better thermal insulation, and better ventilation, but less glare, less polluted outside air, less annoyance from solar heat and less anxiety about crime. 6) The bedroom humidity ratios were higher; the humidity sensation and perspiration sensation were higher in partial cooling dwelling units. 7) The total sleep quality score and the sleepiness score of morning awakening were better for partial cooling users. No differences were found between sleep maintenance scores, although partial cooling users awakened more frequently during sleep than full-time cooling users did.

Age effects on air-conditioner use in summer
Tatsuki ENDO, Noriko UMEMIYA and Xiaoyong LIN
Abstract book of the 16th Conference of the International Society of Indoor Air Quality & Climate, 2018, No.189, Seoul, Nov 1 - 4, 2020.
Relations between age and electric power use for cooling (AC use) were investigated for 378 family-type apartments in Osaka. The survey respondents were classified into age groups of people in their 30s, 40s, 50s, 60s, and 70s users. Number of family members, air conditioners, and bedrooms were considered. Results are the following: 1) AC use is greatest for 40s users; it decreases with age. 2) AC use for single-person households becomes greater with age. 3) AC use for single-AC households decreases with age. 4) Age differences in AC use decrease as family members and air conditioners increase. 5) Effects of consciousness on AC use are small for 70s users.

Thermal sensation effects evaluated during road traffic, construction site, and railway noise
Noriko UMEMIYA and Naohiro KATADA
Proceedings of the 13th ICBEN Congress on Noise as a Public Health Problem, Karolinska Institutet, Stockholm, Sweden, 14-17 June 2021.
This study examined the relation between noise evaluation and thermal sensation. In an experimental room, 324 students evaluated noises from summer through autumn. They evaluated loudness and impressions of road traffic noise, two railway noises, and three construction site noises, each given for 10 s at three levels of 72 dB, 65 dB, and 58 dB. Participants then recorded their evaluations for 45 s. For each participant, the noise order was set randomly using Latin grid method. Participants also responded to thermal sensations in the experimental room using a seven-point scale. Results show a relation between noise evaluation and thermal sensation. Relations differed by the kind of noise, and with hotter thermal sensations. Road traffic noise was evaluated as louder; construction site noise was evaluated as less loud. Railway noise was evaluated as least loud at points near thermally neutral. These tendencies were more distinct for high sound levels.

Difference of cooling use during sleep between elderly and young people
N. UMEMIYA, K. TARAO and Y. CHEN
Proceedings of the IBPC2021, 2021.
In Japan, nearly 80% of heatstroke occurrences in recent years have involved people older than 65 years old. This study surveyed the actual use of cooling by elderly people at sleep time compared to those found for younger people. Results revealed the followings. 1) Ratios of cooling use at sleep time were 30.8% for elderly people and 57.4% for younger people. The respective ratios of natural ventilation use at sleep time were 39.9% and 32.4%.
2) Average wet bulb globe temperatures (WBGTs) of bed rooms during sleep were 26.9°C for elderly people and 26.4°C for younger people. 3) Elderly people feel warmer than younger people but they feel more thermally comfortable. 4) Sleep scores were 49.7 for elderly people and 48.5 for younger people. No difference was found for the frequency of night waking or the Sleep maintenance score, but the Fatigue recovery score showed the greatest difference between elderly and younger people.

Seasonal variation of sleep quality and thermal control use in summer
Noriko UMEMIYA and Yuhang CHEN
Proceedings of the ICB, 2021.
This study analyzed seasonal variations of thermal control use during sleep. During late summer in 2014–2019 in Osaka, bedroom temperatures in 198 apartments were surveyed at 10 min intervals. 1) All-night AC without

NV or electric fans was 24.1% in the early period and 19.7% later, but partial AC without NV or electric fans was 15.7% in the early period and 9.1% later. Seasonal differences were slight for all-night NV without AC or electric fans, all-night NV with electric fans, and all-night AC with electric fans. 2) Sleep quality scores for 'drowsiness when awakening' were lower for AC than for NV in the later period. 3) Sleep quality scores for 'sleep maintenance' were related to thermal sensations, thermal comfort, and sweating sensations for both AC and NV in the early period. Results were related only to thermal sensations for AC and to thermal sensations, thermal comfort, and SET* for NV in the later period.

Simplified CFD modelling method and accuracy verification of airflow from ceiling-mounted personalized air supply terminal

Tomohiro KOBAYASHI, Hiroki NISHIHORI, Noriko UMEMIYA, Toshio YAMANAKA, Atsushi KASUYA, Yusuke KOBAYASHI and Kazuki WADA

The purpose of this study is to establish a CFD modelling method of the airflow from personal air supply terminal. First, the velocity distribution was measured by the wire anemometer to obtain boundary conditions and true value of CFD. Second, the accuracy of the CFD is verified. To do this CFD, a large number of grid is required, which leads to large computational load and difficulty in analysing a large space. Therefore, to decrease the number of grids without loosing accuracy, the momentum method and P.V. method are applied, and its analysis is presented.

Fundamental Study on the Thermodynamic Non-Equilibrium Freezing Probability Prediction Model Taking into Account the Super Cooling Phenomena in Porous Material

Yoshihiko KISHIMOTO

It is commonly considered that frost damage is caused by sudden freezing of supercooled water, which is a random phenomenon. Therefore, the aims of this study are to establish a prediction model for the probability of freezing until any lowest reached temperature, and to obtain the probability distribution function of the freezing point for the proposed analytical prediction model. First, theoretical prediction model for the probability of the instantaneous increment of ice content when lowest achieving temperature was known was derived based on these assumptions that building structure is an aggregation of small elements. Next, the freezing point measurement was carried out by using saturated mortar samples as the small element. As the results, it could be found that the first freezing due to supercooling occurred from -4 to -11 deg. C and the maximum probability was appeared at -7.5 deg. C. The average increment of ice content at every temperature closed to the 40 % volume of pore water until the thermodynamically-based freezing point. Moreover, the method that can calculate the probability distributions of the instantaneous increment of ice content for any lowest achieving temperature from pore size distribution was proposed. The calculation results of the proposed method had good agreements with the measurement results.

Seismic performance of exterior R/C beam-column joint under varying axial force

Yanbing HU, Yusuke SUZUKI, Kinwoong JIN and Masaki MAEDA

Previous studies have suggested the maximum experimental story shear force of beam-column joint frame does not reach its theoretical value due to beam-column joint failure when the column-to-beam moment capacity ratio was close to 1.0. It was also pointed out that under a certain amount of axial force, an axial collapse and a sudden decrease of lateral load-carrying capacity may occur at the joint. Although increasing joint transverse reinforcement could improve the lateral load-carrying capacity and axial load-carrying capacity of beam-column joint frame, the conditions considering varying axial force were still not well investigated. For this purpose, 7 full-scale specimens with no-axial force and 14 half-scale specimens with varying axial force are designed and subjected to static loading tests. Comparing the experimental results of the two types of specimens, it has indicated that introducing the varying axial force leads to a reduction of the required joint transverse reinforcement ratio which can avoid the beam-column joint failure. For specimens with varying axial force, to prevent beam-column joint failure and axial collapse, the lower limit of joint transverse reinforcement ratio is acquired when given a column-to-beam moment capacity ratio.

Analytical study on the effects of X-shaped reinforcement for RC exterior beam-column joint structural characteristics

Seitaro KAGEYAMA, Yuta TAKASHIMA and Yusuke SUZUKI

In this study, FEM analysis was conducted on elasto-plastic behavior of a RC exterior beam-column joint structure using X-shaped reinforcing bars. The effect of the X-shaped reinforcing bars for the structural performance of the structure was evaluated, and a more rational reinforcement arrangement method was investigated. The analysis results showed that X-shaped reinforcing bars contributes to the reduction of joint shear deformation, concrete crushing in the joints, and the improvement of deformation capacity of structure. The above effects were observed to be more effective for beam-column joint structures with a column-beam strength ratio of 1.8 or higher. It was also found that it is important to place the X-shaped reinforcing bars near the center of the cross section in the joint panel.

Urban Design and Engineering

Site Investigation Results and Verification of Liquefaction Countermeasure Effect by Groundwater Lowering Method at Tsukiji in Amagasaki City
Akihiko OSHIMA, Kengo YASUDA (Kajima Corp.), Suguru YAMADA, Seiji SUWA (Geo-Office SUWA), Shuichi TAKAHASHI (Daiwa House Industry) and Akira FUKAI (Sekisui House)
Journal of the Society of Materials Science, Japan, Vol .69, No.1, pp. 97-104, 2020. (in Japanese)
In the Tsukiji district in Amagasaki city, Hyogo prefecture, Japan, where the extremely severe liquefaction-caused residential damage happened during the 1995 south Hyogo earthquake, the groundwater level has been controlled to keep GL-3.0m as the liquefaction measure by the groundwater lowering method. In this study, various ground investigations were performed at Tukiji area in June 2017 to investigate the effect of liquefaction measure by groundwater lowering as well as the present ground properties in the area where about 20 years have passed since the implementation of the measure to lower groundwater. Additionally, the liquefaction strength of the alluvial sand layer was investigated by laboratory tests using sampling specimens. In the paper, the present ground properties obtained by ground investigations were presented. Further, a result of the verifying the effect of liquefaction measure by the groundwater lowering method was reported. In the verification, liquefaction potential was evaluated for both the ground after and before the groundwater lowering was implemented on the basis of ground investigation results obtained in 2017 and 1995.

Comparison between Results of Swedish Weight Sounding Test Stated in JIS and Weight Sounding Test Stated in ISO
Akira FUKAI (Sekisui House), Akihiko OSHIMA, Kengo YASUDA (Kajima Corp.) and Yuji MATSUTANI (Sekisui House)
Japanese Geotechnical Journal, Vol .15, No.3, pp. 635-642, 2020. (in Japanese)
There are JIS specifications and ISO specifications (Weight sounding) in the Swedish weight sounding (SWS) test. Currently, JIS revision work of SWS test is being carried out, and a consistency with ISO specifications which was enacted in 2017 is required to correspond to internationalization. There are significant differences in shape of screw point (SP) and rod diameter in the two specifications, and it is considered that they may affect the test results. Therefore, we carried out comparative tests at five sites under different terrain and ground conditions. In addition to these conditions, the effects of abrasion were also examined using damaged SP.　In this sounding test, we adopt an automatic testing machine that can automatically control during self-sinking and maintain a constant rotation speed. Test results of JIS and ISO almost agreed. In the case of cohesive soil, the variation in results was particularly small.

Technical Problems for Evaluation of Residential Ground ~ Evaluation Technology of Residential Ground due to Swedish Weight Sounding Test ~
Akihiko Oshima,
Geotechnical Engineering Magazine, Vol .68, No.2, pp. 6-9, 2020. (in Japanese)

Prediction of Ground Settlement on Aquifer Thermal Energy Strage Using Single and Double Aquifer Layers
Hiroshi ICHITANI (Urban Engineering), Akihiko OSHIMA, Shuhei TEMMA (Nippon Koei), Masayoshi NAKAO (Advanced Research Institute), Yauhisa NAKASO (Advanced Research Institute)
Proceedings of the Kansai Geo-Symposium 2020, Vol .9, pp. 31-36, 2020. (in Japanese)

Expansion of 250 m Square Mesh Model and Distribution of Geotechnical Characteristics on Ma12 Layer in Osaka and Kobe Area
Mari KASUGAI (Geo-Research Institute), Tomoya YAMAGUCHI (Urban Engineering), Yuta KASUTANI (Urban Engineering), Akihiko OSHIMA and Teruyuki HAMADA (Geo- Research Institute)
Proceedings of the Kansai Geo-Symposium 2020, Vol .9, pp. 84-89, 2020. (in Japanese)

Leaching Characteristics of Naturally Derived Toxic Elements in the Alluvial Marine Clay Layer beneath the Western Osaka Plain
Hiroko ITO (Geo-Research Institute), Harue MASUDA (Faculty of Science) and Akihiko OSHIMA
Proceedings of the Kansai Geo-Symposium 2020, Vol .9, pp. 191-196, 2020. (in Japanese)

Site Investigation Results and Geotechnical Characteristics of Clay Layers at Nishiiwata in Higashi Osaka City
Akihiko OSHIMA, Yuta KASUTANI (Urban Engineering), Shuichi TAKAHASHI (Daiwa House Industry), Akira FUKAI (Sekisui House) and Masaki KUBO (Osaka Monorail)
Proceedings of the 14th National Symposium on Ground Improvement, the Society of Material Science, pp. 563-570, 2020. (in Japanese)

Site Investigation Results and Geotechnical Properties of Ariake Holocene Clay Layer at Shiraishi-cho in Saga Prefecture
Akihiko OSHIMA, Sachi TANAKA (Kansai Airports), Kodai TAKENO (Urban Engineering), Zhilei DUAN (Urban Engineering), Shuichi TAKAHASHI (Daiwa House Industry) and Akira FUKAI (Sekisui House)
Proceedings of the 14th National Symposium on Ground Improvement, the Society of Material Science, pp. 571-576, 2020. (in Japanese)

A Study on Penetration Mechanism of Heavy Dynamic Cone Penetration Test ~ Correction of Number of Blow based on Driving Efficiency, Measurement of Skin Friction and Measurement of Angle of Driving Hole ~
Sachi Tanaka (Kansai Airports), Shuichi Takahashi (Daiwa House Industry), Akihiko OSHIMA, Tatsuya Sakaguchi (Urban Engineering) and Suguru YAMADA
Proceedings of the 14th National Symposium on Ground Improvement, the Society of Material Science, pp. 645-652, 2020. (in Japanese)

Comparison of Fully Automatic Testing Machine of Swedish Sounding Test and Effect of Screw Point Diameter and Wear
Akira FUKAI (Sekisui House), Akihiko OSHIMA, Yudai HAGIHARA (Urban Engineering) and Yuji MATSUTANI (Sekisui House)
Proceedings of the 14th National Symposium on Ground Improvement, the Society of Material Science, pp. 653-660, 2020. (in Japanese)

Construction of 250m Square Mesh Shallow Subsurface Model in Osaka and Kobe Areas
Mari KASUGAI (Geo-Research Institute), Akihiko OSHIMA
Japanese Geotechnical Journal, Vol .16, No.3, pp. 257-273, 2020. (in Japanese)
In urban areas, excessive groundwater pumping has caused severe ground settlement in the past. As a result, the pumping of groundwater is now regulated, raising the level of groundwater and causing various problems such as the risk of liquefaction. Shallow subsurface model has been well utilized for the evaluation of geo-disasters such as earthquake motion and liquefaction potential. To date, it has been constructed nationwide by various methods. In this study, we constructed shallow subsurface model using Kansai Geo-informatics Database from the surface layer to the engineering basement for every 250m mesh in the Osaka and Kobe areas. We also modeled the grain size characteristics of the sand layer and the geotechnical properties of the clay layer. These results provide basic data for solving geotechnical problems.

Sightseeing Verbal Maps for Visually Impaired by Using Virtual Reality System Specialized in Sound
Hiroko MATSUMOTO, Takashi UCHIDA and Yuta YANAGAWA
Journal of Japan Society of Civil Engineers, Ser. D3, Vol.75, No.6, pp.I_491-I_500 (2020) (in Japanese)
Visually impaired people can walk on the street using a voice AR application that replaces visual in-formation by auditory information. However, there are always some risks. It is difficult for visually im-paired people to use it safely in unfamiliar areas, and to understand voice guidance correctly.
This research tries a virtual reality system that reproduces sound of the city using sound virtual reality in indoor space and uses the voice AR application for the visually impaired people. We improve the re-cording method and reproduction method of environmental sound, and aim for the development to "sightseeing verbal maps."

Utterance Analysis for Evaluating Scenarios of Dialog Robot to Increase Going-out Motivation
Hiroko MATSUMOTO, Takashi UCHIDA and Yuriko YOSHIKANE
Japan Society of Civil Engineers，Proceedings of Infrastructure Planning, No. 61，pp.35_1-7 (2020) (in Japanese)

To support the daily living of visually impaired people, we have been conducting research on pedestrian navigation, mainly audio guidance by "Verbal maps." In collaboration with "Verbal maps," we plan a dialogue robot that can guide a person in a plaza space. As the first step, this study establishes objective indicators based on utterance analysis.

This paper first presents the research background and objectives. Chapter 2 describes the research method. In chapter 3, we consider indicators based on utterance analysis, and chapter 4 illustrates the dialogue experiments. Chapter 5 discusses the validity of indicators based on utterance analysis. Finally, this report provides a summary of the research.

Construction of Unity Virtual Space for Exploring Guide Dog Robot's Avoidance Behaviors

Hironobu TADA and Takashi UCHIDA

Japan Society of Civil Engineers，Proceedings of Infrastructure Planning, No. 63，pp.1025_1-4 (2021) (in Japanese)

We have been studying a walking support system to help visually impaired people walk in a square space using a "guide robot dog" linked to a " verbal map". However, the behavior of the system has not been studied sufficiently, and it is difficult to study the system safely in real space. Therefore, we focused on the virtual space and built an application "SCIBOT_VR" for examining the behavior of a guide robot dog by using the virtual space on Unity to map-model a shopping mall as well as to set the avoidance behavior and avoidance parameters of the guide robot dog. Avoidance behavior and parameters were studied using the application. Then, we clarified the optimal behavior in the virtual space.

Zoom Remote Experiment for Practical Development of Sightseeing Verbal Maps

Masahiro ISHII, Hiroko MATSUMOTO and Takashi UCHIDA

Japan Society of Traffic Engineers, Proceedings of the Conference of Japan Society of Traffic Engineering, No. 41，pp. 127-134 (2021) (in Japanese)

The authors have been conducting research on the application of "verbal maps" that replace visual information with auditory information. In recent years, we have been trying to create a " Sightseeing Verbal Maps " for visually impaired people to enjoy walking to improve their quality of life (QOL). This time, we chose Itami Sky Park and the approach to Kiyomizu Temple Road as the target areas, and we created a map of sightseeing spots by incorporating guideposts, environmental sounds, and sound effects that are closer to reality and motivate people to go out. In addition, due to the influence of the Corona disaster, virtual walking experiments and interviews for the visually impaired, which had been conducted in the laboratory, were conducted online using the teleconference tool Zoom. Through the interviews, we were able to improve the word map, clarify useful environmental sounds and sound effects, and examine the feasibility of the online environment.

Comparative Analysis of Bicycle-Vehicle Conflicts According to Bikeway Setback Distances at Signalized Intersections

Ibuki SAKAI and Nagahiro YOSHIDA

Japan Society of Civil Engineers，Proceedings of the annual meeting in Kansai， 2 pages (CD-ROM) (2020) (in Japanese)

In Japan, most bicycle accidents occur at intersections, so there is a need to make intersection design safer. As a related technical standard, the "Guidelines for Creating a Safe and Comfortable Bicycle Use Environment" was established in 2012, and the development of bicycle riding space is being promoted nationwide. The guideline states that bicycles should use the roadway as a basic rule, and the traffic space should be connected in a straight line even at intersections, and shared lane road markings should be installed on the extension of the roadway edge. However, in the current guideline, there are some problems such as the possibility of bicycles being in the blind spot of large vehicles at intersections and the traffic space being blocked by vehicles waiting to cross. The "protected intersection," which has been introduced in North America in recent years based on the Dutch technical standards, is an intersection structure that enhances the safety of bicycles at intersections. However, it has not been clearly shown how these intersections affect the safety of bicycles and other vehicles. In this study, we will analyze the difference in driving behavior of bicycles and vehicles turning right or left and the degree of complication risk by observing bicycle-vehicle conflicts at signalized intersections with different setback distances of bicycle crossing zones.

A Study on Pedestrian Traffic Flow in Crowd Situation by Using Mobile Tracking Data
Naotaka NISHIMURA and Nagahiro YOSHIDA
Japan Society of Civil Engineers，Proceedings of the annual meeting in Kansai， 2 pages (CD-ROM) (2020) (in Japanese)
In recent years, the number of crowd outbreak situation has been increasing due to an increase in the number of time-intensive events such as sports or concerts, as well as the paralysis of traffic functions during natural disasters. In addition, both domestic and international, there have been crimes under the crowd situations.
On the other hand, with the sophistication of information and communication technology, overseas related studies are being made to simulate pedestrian behavior and analyze crowd conditions using big data. In Japan, there have been predictions of crowd behavior using simulations and analysis of tourist behavior characteristics using the mobile tracking data, but there is still a lack of knowledge about observing crowd behavior in walking spaces and crowd control and response in the event of a disaster. In this study, we will focus on the directionality, walking speed, density, and spatial conditions of crowds, excluding psychological conditions, and use mobile tracking data obtained from smartphones to obtain basic knowledge about pedestrian traffic flow during crowd events.

AN ANALYSIS OF FACTORS AFFECTING VITAL REACTION IN BICYCLE FACILITIES BASED ON DRIVING EXPERIENCE
Katsumasa TATSUNO and Nagahiro YOSHIDA
Japan Society of Civil Engineers, Proceedings of Infrastructure Planning, No. 61, 4 pages (2020) (in Japanese)
There are various types of bicycle lanes on sidewalks and roadways that separate or share the space with other modes of traffic. However, few research examples capture the interaction between rider reaction, fac-tors in the traffic environment, and rider knowledge when examining what makes a traffic lane desirable from the rider point of view. In this study, to obtain essential knowledge regarding the method of meas-uring the relationship between stress factors and reactions related to bicycle use, vital reaction is measured in multiple traffic situations with different driving tasks and stress factors. Then, by conducting a com-parative analysis of the rider reaction in driving experience.

A STUDY ON THE EVALUATION OF COMFORT FOR PEDESTRIANS AND CYCLISTS CONSIDERING USERS' ACTIVITIES － A CASE OF ROAD SPACE REALLOCATION ON MIDOSUJI STREET IN OSAKA －
Haruka KAWACHI and Nagahiro YOSHIDA
Japan Society of Civil Engineers, Proceedings of Infrastructure Planning, No. 61, 4 pages (2020) (in Japanese)
The road space reallocation project in the main street of Osaka, Midosuji has started to realize the con-cept of human-centered urban space. The project has been undertaken in the way of increasing the space for pedestrians and cyclists. In addition, we are pursuing more comfortable road space by installing rest space. While the Level of Service concept was widely employed to evaluate user comfort issues in the transportation field but it is unknown that the LOS concept could apply to these space differences and evaluate the reallocation effect correctly. In this study, we focus rest space and conduct a survey how in-stalling the space affects traffic flow and pedestrians' activities, and how it affects comfort. As a result, separated road space by rest space effects comfort, and they feel comfort when they walk if the road space where they can walk narrow. However, we have to think the well designed.

Development of a Method for Estimating Pedestrian Tracking and Cross-sectional Traffic Volume on Sidewalks using Movie Images
Atsushi TAKIZAWA, Nagahiro YOSHIDA, and Shinpei ITO
Architectural Institute of Japan, Summaries of Technical Papers of Annual Meeting, Summaries of Design Works of Annual Meeting, 2 pages (2020)
Investigating and analyzing the relationship between human behavior and spatial configuration in architecture and urban space is a fundamental task in architectural and urban planning. However, it is difficult to conduct continuous or large-scale surveys because such surveys rely on human labor. In recent years, there has been a remarkable evolution of object detection methods from images based on deep learning. Last year, we proposed and verified a method for detecting pedestrians on a sidewalk and estimating their basic behavior on a street using this object detection method. Since object detection is performed independently for each still frame, it is not possible to determine whether a person detected in different frames is the same person or not. Therefore, it is insufficient for understanding the trajectory of human movement and continuous actions. In this study, we

develop a human tracking method that combines several deep learning methods and apply it to a video of a sidewalk, including a crosswalk, which was shot from a relatively far distance as in the previous year. In addition, we will apply the method to a cross-sectional traffic survey of pedestrians and verify its accuracy.

An Evaluation of Bicycle Class for Preschool Children using Balance Bicycles
Itaru FUJIE and Nagahiro YOSHIDA
Japan Society of Civil Engineers, Proceedings of Infrastructure Planning, No. 62, 4 pages (2020) (in Japanese)
Bicycles are a familiar and convenient means of transportation that everyone can use, but on the other hand, they are also a means of transportation with high risks. For this reason, traffic safety education for bicycles has been conducted in certain places, especially in schools, but little consideration has been given to bicycle education programs for people with disabilities. The authors have practiced through specific activities that people with disabilities may be able to ride bicycles safely by going through appropriate educational processes. In this report, we summarized the conventional idea of developing various bicycle education programs according to the developmental stage, and discussed the learning effects (spontaneity, physical strength, sociality, etc.) and issues through the trial at a special needs school. As a result of developing a program that the teachers themselves could operate on a daily basis and setting up the environment for the program and conducting trials, we were able to confirm various effects. From the results of these activities, we were able to deepen our understanding of inclusive cycling for people with disabilities and identify issues that need to be addressed in order to support the ultimate goal of social independence.

Comparative Analysis of Bicycle-Vehicle Conflicts According to Bikeway Setback Distances at Signalized Intersections
Ibuki SAKAI and Nagahiro YOSHIDA
Japan Society of Civil Engineers, Proceedings of Infrastructure Planning, No. 62, 4 pages (2020) (in Japanese)
In Japan, bicycle traffic space at intersections is supposed to be straight, while in other countries such as North America, there are attempts to increase safety by setting bicycle traffic space far back from the roadway edge. However, it is not clear how the safety of bicycles and motor vehicles is affected by the change in the complicated conditions of bicycles and motor vehicles. In this study, we focused on the position of the bicycle crossing zone at signalized intersections, and analyzed how the behavior of bicycles and automobiles and the degree of complexity risk changed by observing signalized intersections with different setback distances from the roadway edge using video analysis methods.

Study on Pedestrian Traffic Flow in Crowded Conditions Using Mobile Location Data
Naotaka NISHIMURA and Nagahiro YOSHIDA
Osaka City University, Memoirs of the Faculty of Engineering, Vol. 61, pp.XX-XX (2020)
In recent years, in Japan, the number of incidents involving large crowds has been increasing for several reasons, including the increase in the number of such time-intensive events as sports events and concerts, the increase in the number of tourists, and the paralysis of traffic functions caused by natural disasters. However, the increasing sophistication of information and communication technologies and smart phones has increased the technological possibilities and improved crime prediction systems, leading to the development of pedestrian agent simulations and the analysis of crowd conditions using big data. However, there is still a lack of knowledge on crowd control at the micro level of events, such as fireworks displays and disasters. The purpose of this study was to gain new knowledge on how to understand and control crowd behavior at events by analyzing mobile location data obtained from smartphones.

A Comparative Method for Evaluating Ecosystem Services from The Viewpoint of Public Works
Tomonari OKADA, Yugo MITO, Kanae TOKUNAGA, Hiroaki SUGINO, Takahiro KUBO, Yoshihiro B. AKIYAMA, Toru ENDO, Sosuke OTANI, Susumu YAMOCHI, Yasunori KOZUKI, Takayuki KUSAKABE, Koji OTSUKA, Ryoichi YANAGAWA, Takaaki SHIGEMATSU and Tomohiro KUWAE
Ocean and Coastal Management, Volume 212, 105848 (2021)
Nature-based solutions (NbS), such as the implementation of environmental conservation and restoration as public works projects, require accurate and cost-effective assessments of the values related to the projects. The values should represent collective ecosystem services, individual services such as food provision and water purification, and other intangible services. To comprehensively assess such services, we proposed a novel method, which we call the comparative evaluation method. Our method is able to assess the value of each service category of an NbS project from a single questionnaire survey. Survey participants are asked to

compare values of multiple services having anchoring prices. Our method determines the permissible economic value of environmental public works (PEP) in response to the quantity of service. The questionnaire results used for analysis are limited to those from respondents who made their PEP evaluation on the basis of their consideration of the appropriate expenditure of taxes. In addition, the method controls for the effect of the satisfaction that a person experiences from doing good deeds to reduce an overestimation of the values of services. Moreover, PEPs are not influenced by the respondent's annual income, age, sex, or educational background, and are based on personal values. Applying this new method, we surveyed residents of the watersheds of Tokyo Bay and Osaka Bay and evaluated nine ecosystem services. Overall, our new method is shown to be an effective method for evaluating the ecosystem services of NbS projects from the viewpoint of public works.

A Study on Carbon Absorption by Seaweeds in the Artificial Salt Marsh at Osaka-Nanko Bird Sanctusry

Hiroyuki OOKA, Toru ENDO
Journal of Japan Society of Civil Engineers, Ser. B3 (Ocean Engineering), Volume 77, Issue 2, Pages 913-918 (2021) (in Japanese)

To clarify the carbon absorption characteristics of seaweeds growing in the artificial salt marsh at the Osaka-Nanko Bird Sanctuary, we measured the gross photosynthetic rate of *Ulva ohnoi*, *Gracilaria parvispora*, *Ulva prolifera* sampled in the bird sanctuary by laboratory experiments. Furthermore, we examined the annual variation in the photosynthetic activity of each algae in the bird sanctuary after creating equations for estimating the gross production rate under arbitrary environmental conditions. We found that the carbon absorption of *Ulva ohnoi* and *Ulva prolifera* strongly depended on salinity while that of *Gracilaria parvispora* depended on light quantum from the relationship between the gross photosynthetic rate and the light intensity of each alga with respect to water temperature and salinity. A comparison of the monthly changes in the photosynthetic activity of the algae in the aviary during seasonal variations in water quality revealed that the carbon absorption capacity of *Ulva ohnoi* was greater than that of *Gracilaria parvispora*, *Ulva prolifera* throughout the year, indicating that *Ulva ohnoi* contribute significantly to the carbon absorption function of the Osaka-Nanko bird sanctuary.

Contribution of Biological Effects to Carbonate-System Variations and the Air–Water CO2 Flux in Urbanized Bays in Japan

Tatsuki TOKORO, Shin-ichiro NAKAIKA, Shintaro TAKAO, Tomohiro KUWAE, Atsushi KUBO, Toru ENDO and Yukihiro NOJIRI
Journal of Geophysical Research: Oceans, Volume 126, Issue 6, e2020JC016974 (2021)

We evaluated the contribution of net biological effects (photosynthesis + respiration + decomposition) to the carbonate parameters and air–water CO_2 fluxes in Tokyo Bay, Ise Bay, and Osaka Bay in Japan. The carbonate parameters (fugacity of CO_2, total alkalinity, and dissolved inorganic carbon) were measured mainly by cargo ships traveling between Japan and other countries. We used the measurement data from three inner bays and surrounding outer bays in Japan along with reference data from previous studies for complementary analysis. We found that (a) the inner and outer bays in this study were strong annual atmospheric CO_2 sinks, (b) the annual biological effect on the air–water CO_2 fluxes was about 6%–27% of the measured CO_2 fluxes, and it affected the seasonal variation of the CO_2 flux, and (c) the biological effect was largest in Tokyo Bay, and almost the same in Ise and Osaka Bays. The intensity of the biological effect corresponded mainly with nutrient concentrations, which seemed to be controlled by the wastewater treatment in urbanized areas around the bays. Our results suggest that labile carbon/nutrient ratio of wastewater should be a major consideration for evaluating the biological effect on the carbon cycle in urbanized bays, which will continue to expand globally.

Green Port Structures and Their Ecosystem Services in Highly Urbanized Japanese Bays

Tomonari OKADA, Yugo MITO, Yoshihiro B. AKIYAMA, Kanae TOKUNAGA, Hiroaki SUGINO, Takahiro KUBO, Toru ENDO, Sosuke OTANI, Susumu YAMOCHI, Yasunori KOZUKI, Takayuki KUSAKABE, Koji OTSUKA, Ryoichi YAMANAKA, Takaaki SHIGEMATSU & Tomohiro KUWAE
Coastal Engineering Journal: Blue Carbon Engineering, Volume 63, Issue 3, Pages 310-322 (2021)

Green port structures (i.e. green infrastructure in ports and harbors) featuring habitats for marine organisms have been promoted in Japan as part of a comprehensive policy to reduce the environmental impact of ports and carry out habitat conservation, restoration, and creation. In this study, we evaluated the ecosystem services provided by green port structures in two highly urbanized bays (Tokyo Bay and Osaka Bay) in Japan. Our results show that the provision of some ecosystem services can be limited by circumstances particular to ports

and other areas with restricted access. In the case of green port structures that have strong usage restrictions, for example, cultural services can only be provided if relevant authorities are prepared to conduct public events while ensuring participant safety. On the other hand, green port structures with weak usage restrictions are often equipped with incidental facilities such as parking lots and restrooms; these facilities can enhance the provision of cultural services (e.g. recreation and environmental education). Green port structures in highly urbanized bays often have usage restrictions, but their proximity to large populations means that they can potentially provide numerous ecosystem services. However, our study shows that appropriate management goals, such as protecting species and ensuring healthy habitats, are needed to maintain the value of these services in highly urbanized and eutrophic bays.

Spatial Distribution of Dissolved Inorganic Carbon in Yamato River and Its Effect on Carbon Dynamics in the Coastal Estuarine Waters

Noriko HARADA, Toru ENDO, Tomoki SAIKI, Tetsuji OKUDA, Satoshi ASAOKA, Satoshi NAKATA
Journal of Japan Society of Civil Engineers, Ser. B2 (Coastal Engineering), Volume 76, Issue 2, Pages I_931-I_936 (2020) (in Japanese)

Field survey of dissolved inorganic carbon (DIC) was conducted in Yamato river, Japan every season for two years, for the purpose of clarifying the characteristics of DIC distribution in an urban river and the effect of the carbon runoff from the river on the carbon dynamics of the coastal waters. The DIC concentration in Yamato River tended to be lower in summer and rainy day by high flow rate. Furthermore, the DIC concentration almost didn't fluctuate in the lower Yamato river, which is urban area, however the DIC concentration fluctuated in the upper Yamato river due to the effect of sewage treatment water and respiration and decomposition. On the other hand, we found that the 80% of total dissolved carbon discharged to the estuary coastal area was form of DIC, and the discharge amount of DIC in ordinary condition was equivalent to the daily carbon stock of a seagrass ecosystem of about 9,350 ha. Finally, we found that the Yamato River mouth had characteristics as the DIC concentration was higher than that of the other river mouth, but the partial pressure of CO_2 was lower.

Carbon Storage Effect of Urban Coastal Areas Focused on the Residual Organic Carbon and the Inorganic Carbon in Sediments

Toru ENDO, Koki HAYAMITSU, Yutaro KITANO, Shinya NAKASHITA
Journal of Japan Society of Civil Engineers, Ser. B2 (Coastal Engineering), Volume 76, Issue 2, Pages I_1021-I_1026 (2020) (in Japanese)

Residual organic carbon and inorganic carbon in sediment sampled at shallow and harbor area of Osaka Bay were analyzed for the purpose of revealing the carbon storage effect and characteristics of urban coastal areas. As a result of classifying the sediment organic carbon into the biodegradable organic carbon and residual organic carbon by 100 days biodegradability test, we found that 70 to 80 % of sediment organic carbon in tidal flat was residual organic carbon and almost no organic carbon was stored in sandy beach. As a result of classifying sediment carbon into organic carbon and inorganic carbon by burning at 950 °C and 600 °C of sediment, carbon was stored as not only residual organic carbon but also inorganic carbon such as shells in harbor area. We found that harbor area has stored a large amount of carbon and has a carbon storage effect that is about 2.6 times that of tidal flats. Furthermore, as a result of comparison with the reported carbon storage of shallow coastal ecosystem, it was suggested that urban coastal areas such as tidal flats and port waters can be evaluated as new carbon stocks.

Material Flux of Carbon, Nitrogen, Phosphorus and Contribution to Nitrogen Budget of *Corbicula Japonica* in Mud River Tidal Flat

Sosuke OTANI, Tomoya YASHIKI, Kenta UEMURA, Kunihiro TOKUDA, Kohei FUJISHIMA, Toru ENDO
Journal of Japan Society of Civil Engineers, Ser. B2 (Coastal Engineering), Volume 76, Issue 2, Pages I_935-I_930 (2020) (in Japanese)

The object of this study was to reveal material flux of carbon, nitrogen, phosphorus and contribution to nitrogen budget of *Corbicula japonica* at muddy tidal flat in Yodo river, Japan. We carried out 24 hours investigation on the material flux on 2-3 September (neap tide) and 8-9 October (spring tide) in 2018, and we also carried out the laboratory experiment on NH_4 excretion rate by *C. japonica*. According to this study, we concluded that (1) Material flux of DIN and particulate matter showed absorption in tidal flat, (2) Primary producer absorbed DIN about 1.25kg/day during neap tide and 1.04kg/day during spring tide, (3) NH_4-N excretion by *C. japonica* account for 18.1% of the elution during neap tide and 12.2% of the elution during spring tide. This

study suggested that this tidal flat has purification function of DIN and particulate matter. Furthermore, it was thought that *C. japonica* effect on the material circulation in tidal flat.

Experimental Study on Slip Behavior of Single Side Bolted Friction Joints Using New Type Single-Sided Construction Bolts

Yu LANG[†], Takashi YAMAGUCHI, Yasumoto AOKI (Hanshin Expressway Co. Ltd.), Kunio YARIMIZO, Atsushi TAKEDA (Nippon Pop Rivets and Fasteners Ltd.), Kanji SAKODA (Nippon Pop Rivets and Fasteners Ltd.), Mitsuhiro MINAMI (Nippon Pop Rivets and Fasteners Ltd.)

Journal of Structural Engineering, A, Vol.67A, pp.360-373 (2021). (in Japanese)

The authors have developed a new type of high strength single-sided construction bolt for frictional joints that can be fastened from one side at low cost and has excellent workability. For the purpose of collecting basic data for examining the applicability to steel structures, slip test and U-rib steel loading test of single side bolted friction joints using new type single-sided construction bolts were conducted. As a result, slip coefficient of single side bolted friction joints using new type single-sided construction bolts is about 0.44 to 0.51 about 30% to 40% lower than the high strength bolt, because the contact pressure between members is lower than the bolt axial force.

Effect on Strength Improvement of Stiffener on Tensile Type Bolted Joints with Multiple High Strength Bolt Rows

Yuma SUGIMOTO[†], Takashi YAMAGUCHI

Journal of Structural Engineering, A, Vol.67A, pp.309-322 (2021). (in Japanese)

When tensile type bolted joints are used in bridge structures, these joints have multiple bolt rows to resist a large sectional force. However, it is known that strength of tensile type bolted joints with multiple bolt rows are less than the strength for the number of bolts. This study focuses on a stiffener to improve the strength of tensile type joint with multiple bolt rows, and conducted these joints' experiment and FE analysis. The one of the obtained results is that the set of stiffeners is effective in getting the joint proof strength and the joint yield strength for the number of bolts. Additionally, installing the stiffener can improve the strength with less weight rather than increasing the joint flange thickness in tensile joints with multiple bolt rows.

Analytical Study on Patch Plate Repair Method for Steel I-Girder Bridges with Corrosion Damages Considering Its Bridge System Behavior

Ryoga OURA[†], Kentaro ARIMURA (Oriental Consultants Co., Ltd.), Takashi YAMAGUCHI

Journal of Structural Engineering, A, Vol.67A, pp.26-34 (2021). (in Japanese)

Bridges are composed by many structural members which interact with each other to resist against various load combinations. In the present study, full-scale FE analyses have been conducted for a steel I-girder bridge system with corrosion damages which have been repaired. The analysis considered, the structural system behavior, varying the repaired areas. From the analytical results, it was found that, compared to the method in which the damaged portion is completely repaired, the amount of repair can be reduced by considering the bridge system behavior and partially repair both the damaged and the adjacent intact girders.

Effect of Surface Treatment of Countersunk Hole on Slip Strength of Friction Grip Joints with High Strength Countersunk Head Bolts

Yu LANG[†], Gen HAYASHI, Takashi YAMAGUCHI, Hiroki KATO (West Nippon Expressway Consultants Company Limited), Ken ADACHI (West Nippon Expressway Company Limited), Takuji KUMANO (JFE Engineering Co.), Kenji YOSHIDA (Kawada Industries, Inc.)

Journal of Structural Engineering, A, Vol.67A, pp.349-359 (2021). (in Japanese)

In order to improve durability of corrosion, previous studies reported that countersunk head bolts can be applied to high strength bolted friction grip joints. The surface treatment of the countersunk hole is specified to be inorganic zinc rich paint, if blasting of countersunk hole can be omitted in the construction site, the workability will improve. In this research, slipping test was carried out to evaluate the effect of surface treatment without blasting of countersunk hole on slip strength of friction grip joints with high strength countersunk head bolts. As a result, the effect of surface treatment of countersunk hole on slip strength is very small.

Slip Behavior Between Cast Iron Deck Module and A Steel Main Girder Using Tapered High Strength Bolted Frictional Joints with 1° on the Main Plate
Yugo SHIRAI[†], Gen HAYASHI, Takashi YAMAGUCHI, Hironobu TOBINAGA (Hinode Ltd.), Minoru MURAYAMA (Hinode Ltd.),
Journal of Structural Engineering, A, Vol.67A, pp.336-348 (2021). (in Japanese)
The cast iron deck module is a lightweight deck slab with excellent fatigue resistance. High-strength bolt friction joints are used to join cast iron deck modules and main steel girders. In addition, the high strength bolt friction joints between the cast iron deck module and the main steel girder have to be considered because the ribs of the cast iron deck module have a taper of 1°. In this study, we prepared an experimental specimen of a composite structure of a cast iron deck and a main steel girder, and conducted a horizontal loading test and FEM analysis. As a result, the sliding behavior between the cast iron deck and the main girder was clarified.

Analytical Study on Effects by Tight Type Filler Considering Ultimate Limit State of High Strength Bolted Frictional Joints with A Filler Plate
Masaki FUJIWARA[†], Takashi YAMAGUCHI, Senju KOZAI (Takadakiko Co., Ltd.)
Journal of Structural Engineering, A, Vol.67A, pp.296-308 (2021). (in Japanese)
According to the Japanese Specifications for Highway Bridges, in high strength bolted frictional joints, verifications of the resistances in after-slip behavior are required. In bearing type joints, a filler plate is extended beyond splice plates to connect the filler to a member by additional bolts (tight type filler), but there're few examples of high strength bolted frictional joints with it. In this study, effects by tight type filler in serviceability limit state and ultimate limit state of high strength bolted frictional joints are quantitatively examined by FEM analysis. As a result, tight type filler is effective in slip strength and shear strength of bolts, but there's a risk to deterioration of yield strength and breaking strength of connected plate.

Analytical Study on Application Range of Web Bypass Method and Device Geometrical Configuration for Replacement of Lower Splice Plate of Steel I Girder
Shun MATSUI[†], Takashi YAMAGUCHI, Kensuke TODA (MM Bridge Co., Ltd.), Kenji ARAKI (MM Bridge Co., Ltd.), Motoshi YAMAUCHI (MM Bridge Co., Ltd.)
Journal of Structural Engineering, A, Vol.67A, pp.323-335 (2021). (in Japanese)
In the case of replacing the splice plate against corrosion damage of the steel girder joint part, there is a method of installing an attaching additional device and replacing the corrosion damaged portion of the girder with a new member. Previous research has revealed that the web bypass method, in which the bypass device is bolted to the web, is superior in workability and stress transmission. In this study, we focused on the replacement of lower splice plate, analyzed it using the steel I girder shape and the shape of the web bypass device as parameters, and examines the applicable range of the web bypass method and the appropriate geometrical configuration of the web bypass device.

Analytical Study on The Effect of Horizontal Stiffeners on The Ultimate Capacity of Steel Box Girder Bridges
Junichi ADACHI[†], Takashi YAMAGUCHI, Shintaro ARAI (JFE Engineering Co.), Michiaki TAKAO (JFE Engineering Co.)
Journal of Structural Engineering, A, Vol.67A, pp.14-25 (2021). (in Japanese)
Automatic welding robots cannot be applied to welding horizontal stiffeners to the web panel of curved steel box girder bridges due to the manufacturing cost increase. Elimination or reduction of the number of horizontal stiffeners without increasing the web thickness is desirable. In the present study, the influence of the horizontal stiffeners on the ultimate capacity and the collapse process were clarified by FE analysis considering the design sectional forces. From the obtained results, it was concluded that, even if the horizontal stiffeners are eliminated, the ultimate capacity decrease is little since the compression flange of box girders restrains bending buckling of the web panel.

Analytical Study on Estimating Bolt Axial Force of Flush Endplate Connection
Yuma SUGIMOTO[†], Takashi YAMAGUCHI
Journal of Structural Engineering, A, Vol.67A, pp.398-411 (2021). (in Japanese)
Recently, the demands of flush endplate connections have been increased in the field of bridge structures. However, no estimation-methods are proposed of the bolt axial force in such connections. This study proposes a new estimation method of the bolt axial force in flush endplate connections by FE analysis. Firstly, prying

force coefficient and joint stiffness formulas are derived from the analysis of joint elements which can simulate the bolt force increment of flush endplate connections. Secondly, formulas for acting force in lower flange, horizontal stiffener and web are also obtained from girder analysis with a lower flange that has the lowYoung's-modulus-region. Finally, the new estimation method for a bolt axial force is established by these proposed formulas.

Analytical Study on The Effect of Changes in The Number of Main Girders on Load Carrying Capacity of Steel I Girder Bridges with Corrosion

Kentaro ARIMURA (Oriental Consultants Co., Ltd), Ryoga OURA[†], Takashi YAMAGUCHI
The main girders in a steel I girder bridge are connected with the slab, the sway bracing and the cross frame behaving together as a system. Therefore, if a single part of one main girder is corroded, the remaining healthy main girders are supposed to compensate it. In this study, the bridge loading capacity was evaluated using an FEM model of the bridge system assuming some or all girders is corroded. As result, it was observed that in case some girders in a multi-girder bridge system is corroded, some of the remaining healthy main girders compensate it, confirming the bridge system redundancy.

Analytical Study on The Double End Plate Connection Applied to Connection of Uniaxial Loading Member

Yuki MINEYAMA (Komaihaltec Inc.), Hajime TACHIBANA (Komaihaltec Inc.), Tomoyuki TAKAO (Komaihaltec Inc.), Takashi YAMAGUCHI
Recently, infrastructure construction has drawn up an inconvenience that affects the community which is required to minimize as much as possible. To achieve the results, the construction of temporary members must be done quickly. The double end plate connection utilized with high strength bolted tensile joint is considered. The past experiment has confirmed that double end plate connection using high strength bolted can apply to temporary bridge main girder connection with the height from 900mm up to 1,500mm. However, studies for mechanical behavior in low height girders are still unclear. In this study, we have clarified the load transferring mechanism of this connection joint of uniaxial loading member with low height girder by using the analytical results.

Study on Bending Strength and Evaluation of Bolt Axial Force for The Double End Plate Connection with Horizontal Ribs

Yuki MINEYAMA (Komaihaltec Inc.), Yuma SUGIMOTO[†], Takashi YAMAGUCHI
In this study, for shortening erection period of temporary bridges, we propose to use the double end plate connection using high strength bolts at the connection of temporary bridges. The past experiment has confirmed that double end plate connection using high strength bolts can apply to bridge main girder connection. However, the design method is not clear. In this study, we have clarified the bending strength of this connection from the analytical results. Furthermore, in consideration of these results, a simplified calculation method of bolt axial force for this type connection proposed.

Investigation on Residual Axial Force of High-Strength Bolts of Friction Grip Joints in Steel Bridges Under Long-Term Service Conditions and Its Tendency Assessment

Tetsuya IIDA (The Takigami Steel Construction Co., Ltd.), Kunitomo SUGIURA (Kyoto University), Takashi YAMAGUCHI, Yasuo SUZUKI (Toyama University), Hiroo YOSHIZU (Ministry of Land, Infrastructure, Transport and Tourism), Keiji MORITA (Ministry of Land, Infrastructure, Transport and Tourism), Hirotaka ODA (The Takigami Steel Construction Co., Ltd.)
With the aging of civil infrastructures, it is urgent to propose more efficient and simple maintenance and management methods. Higher strength bolts have been known to lose axial force due to relaxation, so that a bolt pre-tension of+ 10% of the designed axial force was introduced at the time of bolt tightening to compensate for the axial force decrease. Therefore, in this research, focus is placed on high strength bolts under long-term service condition. The residual bolt axial force survey of high strength bolts is carried out on steel bridges after 30 to 50 years of construction in order to know whether the bolt's axial force remains in design level as required in the design specification

Influence of Bolt Shape and Dimensions on Mechanical Property of 1700 MPa-Class Ultra-High Strength Bolt

Yuuji KIMURA (National Institute for Materials Science), Hiroshi MASUDA (Utsunomiya University), Takashi YAMAGUCHI, Eiji NAGASAKI, Hitoshi MORIYAMA (Kumamoto University), Kaneaki TSUZAKI (Kyushu University)

1700 MPa-class ultra-high strength bolts were fabricated through quenching and tempering process after cold forming of a prototype steel with a chemical composition of Fe-0.5%C-2%Si-1%Cr-1%Mo (in mass%). Bolt shape and dimensions were optimized to enhance tensile deformation capacity. The developed bolt has a waisted shank and a thread form that are developed for reducing stress concentration at thread roots. Due to its shape and dimensions, the waisted shank precedingly yields and plastically deforms, resulting in higher bolt elongation. The specification of nut was also determined for the 1700 MPa-class shank preceding yield type bolt.

Analytical Study on The Effect of Girder and Connecting Plate Shape on The Moment Sharing Ratio of I Section Girder Connections

Ryo SAKURA[†], Takashi YAMAGUCHI, Yasumoto AOKI (Hanshin Expressway Co. Ltd.)

According to the Japanese specifications for highway bridges, the flange and web joints of the girder connections are designed individually and the applied force in the flange joints is derived from the stress in a flange. On the other hand, it is known that the applied force in the flange joint is determined by both the stress in a flange and the stress in the bearable flange area of a part of the web clearance. Furthermore, the design method adopting the bearable flange area was also proposed under the limited girder shape. In this study, FE analysis was conducted to evaluate the effect of the shape of a girder and connecting plates on the moment sharing ratio and the bearable flange area of a part of the web clearance. It is concluded that the bearable flange area of a web is calculated by the geometrical moment of area, the width of the web joint, and the thickness of the web.

Analytical Study on Bending Buckling Strength of Curved Panel

Junichi ADACHI[†], Takashi YAMAGUCHI, Shintaro ARAI (JFE Engineering Co.), Michiaki TAKAO (JFE Engineering Co.)

In fabricating curved girders, automatic welding robots cannot be applied to welding of horizontal stiffeners to the web panel due to the girder curvature and manufacturing costs increase. Elimination or reduction of the number of horizontal stiffeners is desirable. In this study, FE analysis was carried out varying the curvature and the width-thickness ratio of the web panel. To evaluate the bending buckling strength, the relationship between the bending buckling strength and the curvature has been clarified considering the initial deflection and the residual stress. From the results, it was found that the influence of the curvature on the bending buckling strength of the web panels is small if the radii of curvature are between ∞ and 40m.

Proposal of Yield Strength Formula for High Strength Bolted Split Tee Joints By 3D-FE Model

Yuma SUGIMOTO[†], Takashi YAMAGUCHI

The yield strength of high strength bolted T-stub joint has different definitions depending on design codes. In addition, the stress status at these yield strength points is not clarified. The purpose of this study is that the validation of current design codes is clarified by observing the stress status of joint flange and axial force of high strength bolt by FE analysis. The first result of this study is that the optimal design code is dependent on the joint yield mode. The second result is that the joint yield strength is able to be estimated accurately by combining current design codes.

Analytical Investigation of Patch Plate Flexural Strengthening Effect and Its Required Length for Steel Main Girder with A Field Connection

Takashi MATSUMOTO (CTI Engineering Co., Ltd.), Shunsuke KOBAYASHI (CTI Engineering Co., Ltd.), Takashi YAMAGUCHI

Strengthening of the steel main girder by patch plate is standardly used in redocking. In the case of strengthening across the field connection, patch plate needs processed like a bypass structure, however, strength effect is not clarified. In addition, strength length to achieve sufficient strength effect is not known. Thus, analytical investigation is conducted to clarify the strength effect of bypass structure and, to suggest the required strength length of patch plate. Based on the results, bypass structure decreases nearby panel web's neutral axis, thus it needs to extend more than 1.5 panel from connection. Furthermore, patch plate needs to extend more than 1.5 panel from the end of required strength length to achieve strength effect.

Study on Effect of Bolt's Head Opening Angle on Slip Strength of High Durability Friction Grip Joints with High Strength Countersunk Head Bolts

Yu LANG[†], Takashi YAMAGUCHI, Hitoshi MORIYAMA (Kumamoto University), Misa FUJIBAYASHI (Hanshin Expressway Co. Ltd.), Masayori YOSHIMI (Nippon Steel Bolten Co.)
This study focused on the opening angle of a countersunk head bolt which may have an effect on slip strength. By slip tests and Finite Element Analysis, it was found that as the opening angle increases from 90° to 96°, slip strength was improved. This is because as the opening angle increases, plastic deformation in the vicinity of the countersunk hole can be suppressed. Thereby the reduction in bolt axial force can also be suppressed. However, if the angle is more than 92° the bolt's head will be projecting from the surface of the splice plate. In such a case, the coating failure might be occurred, and corrosion durability will be decreased. Therefore, the optimum angle that can improve both slip strength and corrosion durability is 92°

Experimental Study on High Strength Bolted Frictional Joints with Slotted Hole

Hideyuki KONISHI (Japan Bridge Co., Ltd.), Seiji KAMEZAKI (Oriental Shiraishi Co.), Fumika ASANO[†], Takashi YAMAGUCHI, Izumi HORII[†], Yoshihiro TOKI (West Nippon Expressway Company Limited)
AASHTO shows the slip coefficient of the slotted holes is reduced by 40% from that of the normal holes, while the slip tests that conducted in Japan have shown the slip coefficient of the slotted holes is reduced by 10%. The cause of this difference in the slip coefficient reduction rate has not been clarified. In this study, we conducted the slip test of the high strength bolted frictional joints with slotted holes, focusing on the effect of the slip yield resistance ratio and tightening method of the bolts to verify the past test results. As a result, the slip coefficients of slotted holes were reduced by up to 9%, which were similar to the past results obtained in Japan.

Experimental Study on Mechanical Behavior of High Durability Friction Grip Joints with Long High Strength Countersunk Head Bolts

Yu NAKAMOTO[†], Takashi YAMAGUCHI, Yu LANG[†], Yoshinori HORIOKA (Hanshin Expressway Co. Ltd.), Atsushi SHIBUYA (Miyaji Engineering Co., Ltd.)
The authors focused on a high-strength bolt friction joint with a countersunk head that can smooth the joint surface and prevent functional deterioration due to corrosion. In this study, the slip behavior and maximum resistance of a joint with a long bolt were investigated. It was concluded from the experimental result that the slip coefficient did not change because only a small amount of yielding around the slip coefficient does not change because only a small yielding occurs around the bolt holes when the bolt is long. Although the bolts failed in only one shear plane, there was no significant reduction in maximum bearing capacity compared to the design value of two-plane shear failure.

Analytical Study on Repair Method for Steel I-Girder Bridges with Corrosion Damages Considering Its Structural System Behavior

Ryoga OURA[†], Takashi YAMAGUCHI, Kentaro ARIMURA (Oriental Consultants Co., Ltd.)
Bridges are composed by many structural members which interact with each other to resist against various load combinations. Considering damage repair of one of its structural members, the relationship between the recovery of the individual load-carrying capacity due to the repair of a single member and the improvement of the load-carrying capacity of the structural system is not clear. In the present study, a full-scale FE analysis has

been conducted for a steel I-girder bridge system with corrosion damages which have been repaired. The analysis considered, the structural system behavior, varying the repaired areas and the type of patch members. From the analytical results, it was found that, compared to the method in which the damaged portion is completely repaired, the amount of repair can be reduced by taking into account the structural system behavior and partially repair both the damaged and the adjacent intact girders.

Experimental Study on Mechanical Behavior of Combined Joint Using Adhesives and High Strength Bolts

Takuya KAMINO[†], Takashi FUJIMOTO (Yokogawa Bridge Corp.), Takashi YAMAGUCHI, Yasumoto AOKI (Hanshin Expressway Co. Ltd.), Shinsuke AKAMATSU (Hanshin Expressway Technology Center), Hisakazu HORII (Konishi Co. Ltd.)
Presented at IABSE Congress: *Resilient technologies for sustainable infrastructure*, Christchurch, New Zealand, 3-5 February 2021, published in Resilient technologies for sustainable infrastructure, pp. 1017-1023
As a repair for corrosion damage of a steel bridge, a patch plate-repair using high strength bolts is generally applied. This method requires the surface of the damaged corroded part filled with an epoxy adhesive flat. The load transferring mechanism and slip resistance of such a combined joint with adhesives and high strength frictional bolts aren't clear. Since the shear strength of an adhesive might be increased due to constraint by the bolt axial force, the combined joint's slip resistance would be increased. To clarify the mechanical properties of the combined joint and to propose a new design method for such joints, two experiments have been conducted. The first was a frictional force experiment for adhesive specimens subjected to contact pressure on the surface to evaluate the constraint effect of adhesive on shear strength quantitatively. The last one is a slippage experiment for the combined joints to evaluate its slip coefficient.

One-sided Repair of Corroded Steel Girder End with High-Strength Bolted Doubler Plate and Evaluation of Its Resiliency After the Repair

Hitoshi MORIYAMA (Kumamoto University), Yu LANG[†], Takashi YAMAGUCHI
Presented at IABSE Congress: *Resilient technologies for sustainable infrastructure*, Christchurch, New Zealand, 3-5 February 2021, published in Resilient technologies for sustainable infrastructure, pp. 597-604
Repair of steel girder end is sometimes conducted from one side when work space is restricted or corrosion extent is small. This study focuses on repair with high-strength bolted doubler plate as effective and quick one-sided repair method of corroded girder end. FEA was conducted to evaluate the resistance of intact, corroded and repaired girder and to investigate geometrical dimensions of the doubler plate for enhancing its resiliency. From obtained results, both high repair effect and resiliency can be secured with one-sided bolted and small plate, if the web plate and bearing stiffener is prevented from buckling. As contact force between doubler plate and lower flange is the most important to resisting mechanism, they should be touched with each other. Regarding bolt arrangement, it'd be desirable to reduce the distance between lower flange and end bolt. Finally, the repair work such as jack-up and perforation has almost no influence on the ultimate strength.

Effect of Bolt Hole Diameter of Connected Plate and Thickness Proportion of Joint on Slip Resistance of Frictional Type Bolted Joints with High-Strength Countersunk Head Bolts

Yu LANG[†], Hitoshi MORIYAMA (Kumamoto University), YAMAGUCHI
Proceedings of Constructional Steel Vol.28, pp.137-145, (November 2020). (in Japanese)
Countersunk head bolts can secure thickness of corrosion preventive coating with its flat head and improve anticorrosive properties of bolted connections. In this study, for utilizing its advantages in various type connections, FEA was conducted to investigate effect of bolt hole diameter of connected plate and thickness proportion of the joint with it on frictional slip resistance. From numerical results, it's found that relationship between slip coefficient and slip/yield resistance ratio shows similar tendency in cases of countersunk and hexagonal bolt, and the tendency is evaluated by existing equation of hexagonal bolted joint. Decreasing behavior of bolt tensions is different in two bolt type. The effect of oversized hole is small.

A Study on Reinforcement of Patch Plate Method for Box Section Member with High Strength Stud Bolt

Setsu HOU (FaB-Tec Japan Co.), Qihang SHEN[†], Manabu OKUMURA (FaB-Tec Japan Co.), Takashi YAMAGUCHI, Yuta YAMAMOTO (FaB-Tec Japan Co.)
Proceedings of Constructional Steel Vol.28, pp.561-566, (November 2020). (in Japanese)
Steel members have to be reinforced, as dead load of steel bridge increased by RC Slab Replacement. Reinforcing the member of existing steel truss bridge, repair method by one side patch plate with high strength

stud bolt had been proposed. In this paper, FEM of box section member reinforced with high strength stud bolts (F8T) and high strength bolts (F10T) had been carried out, and their reinforcement effect and stress behavior had been compared and discussed. As a result, the thickness of patch plate with studs is thinner than the one's with bolts, because there is no loss of area by bolt holes. On the other hand, the reinforcement effect would be improved as extend the patch plate to gusset plate.

Experimental Study on Repair Plates of Girder Subjected to Bearing
Ayano MAEHARA (Nagoya Inst. of Technology), Kazutoshi NAGATA (Nagoya Inst. of Technology), Masanari IIDA (Nagoya Inst. of Technology), Takashi YAMAGUCHI, Hitoshi WADA (Takadakiko Co., Ltd.)
Proceedings of Constructional Steel Vol.28, pp.547-553, (November 2020). (in Japanese)
Corrosion is one of the main causes of deterioration of steel structures. One of the repair methods against corrosion is patch plate repair, which is often used especially for the lower flange. However, there are many points that have not been clarified as the current state of patch plate repair, and rational design standards have not been established. In many past studies, analyzes and experiments have been conducted in which only the patch repair part is taken out and uniformly compressed and stretched. Therefore, in this study, a loading experimelt was carried out in which the lower flange was assumed to be corrosion-thinning and the whole girdertepaired with patch plate repair plate was bent, and the load transfer mechanism was examined.

Bonding Splice Behavior and Failure Mode about Damaged GFRP Plate
Akihiko SATO (Kyoto University), Gen HAYASHI, Yasuo KITANE (Kyoto University), Kunitomo SUGIURA (Kyoto University)
Journal of Japan Society of Civil Engineers, Ser. A1 (Structural Engineering & Earthquake Engineering (SE/EE)), Vol.77, No1, pp.13-27 (2021). (In Japanese)
In this study, conducted are a uniaxial tensile test and FE analysis using GFRP plates bonded with repair plates. The tensile test was conducted with two types of GFRP plates that is intact case and damaged case with crack. It is known that the strength of the damaged GFRP plate can be enhanced by bonding repair plate, but it is still lower than the intact GFRP plate. It is also confirmed that bonding repair plate decreases the strength of the GFRP plate even if a GFRP plate has no damage. It is also shown that two types of failure mode classified into debonding of the repair plate and brittle failure of the GFRP plate. FE analysis concluded the reason why the tensile test showed two types of failure mode. FEA showed that bonding repair plate cause stress concentration on the surface of the GFRP plate. This is thought to be the reason why the GFRP plate cause brittle failure before the repair plate cause debonding. Finally, the applicability of failure criteria for composite materials is assessed with respect to the repaired test piece. It is obtained that these criteria underestimated the danger of failure when the fibre failure occurred.

Experimental Investigation on Damage and Wave Propagation of PVB Laminated Glazing Structures under Impact Loading
Amr A. NASSR (Assiut University), Tomomi YAGI (Kyoto University), Takashi MARUYAMA (Kyoto University), Gen HAYASHI
Structures, Vol.29, pp.966-978, (2021).
Experimental investigation on the damage and wave propagation characteristics in PVB laminated glass panels subjected to impact loading was conducted. By applying different impact energies, the effect of two projectile configurations, a wooden post and steel ball, was studied. The effect of impact location was also investigated. The dynamic response of the panels was measured at different locations on the test panels using strain gauges. Damage and transient response and wave propagation characteristics of test panels were reported and compared. The results showed that flexural wave was the predominant wave in the response. In addition, in-plane compressive wave was also observed. It was also shown that while the projectile contact area affected the maximum transient response and crack propagation characteristics, it had a limited effect on the perforation threshold. For panels impacted at the corners, coupled strain waves were created by wave reflection processes when the waves reached the panel boundaries. Moreover, the impact velocity had a pronounced effect on peak strain and strain rates of test panels.

Experimental Study of Change in Load Carrying Capacity and Vibration Characteristics of PC Box Girders with Defective Grout and Failures in Tendons
Kohei TAKEMURA (Kyoto University), Gen HAYASHI, Chul-Woo KIM (Kyoto University), Eiji YOSHIDA (Public Works Research Institute)

Prestressed concrete (PC) bridges account for about 44% of all bridges in Japan, and damage of PC tendons caused by defective grouting has been reported. In order to inspect, repair and maintain the PC bridge efficiently, it is necessary to develop a monitoring technology that can quantitatively and simply evaluate the integrity. This study examines changes in bridge performance and modal parameters of PC box girders due to progressive loading, and defective grouting and failures in PC tendons through the experiment. Static loading test showed that local cracks were dominated around the location of defective grouting and failure of PC tendons. A moderate correlation was observed between the energy-based bending performance and the natural frequency of 1st and 2nd bending modes.

Changes in Frequencies of A Steel Plate Girder Bridge Under Local Damage and Varying Temperatures

Takumi HIROOKA (Kyoto University), Gen HAYASHI, Chul-Woo KIM (Kyoto University)
This study aims to investigate how local damage and varying temperature affect
changes in vibration characteristics and structural behavior of a steel plate girder bridge. A damage experiment on a real bridge was conducted. Observations showed that frequency of each bending frequency changed after introducing damage. Sensitivity analysis showed that frequencies are affected not only by local damage but by changes in characteristics of support, and the 3rd bending frequency was useful to detect the local damage at the edge of the girder. The FE analysis also demonstrated that structural behaviors of supports were affected by stiffness reduction of the girder due to local damage as well as by thermal expansion due to varying temperatures.

Residual Performance of Steel Sheet Pile with Corrosion Damage

Soma ITO (Kyoto University), Gen HAYASHI, Kunitomo SUGIURA (Kyoto University), Yasuo Kitane (Kyoto University)
Steel sheet piles, or larssen sheet piles, were constructed mainly in the 1960s in order to prevent coastal erosion. Corrosion is one of the principal factors that deteriorate steel sheet piles, and determining remaining performance is thus an essential and urgent requirement for the safe maintenance of steel sheet piles with corrosion damage. Hence, the purpose of this study is to comprehend remaining performance of larssen sheet piles with uniform corrosion damage by numerical analysis using Abaqus 6.14. This study concludes that the potextial of a sudden failure caused by buckling occurring before maximum von Mises stress reacties yield stress is a pressing concem in the maintenance of corroded larssen sheet piles.

List of Presentations

at

International Conferences

Mechanical Engineering

Global Convection Characteristics of Conical Taylor-Couette Flow with Shear-thinning Fluids
Hayato MASUDA, Hiroyuki IYOTA and Naoto OHMURA
24th International Congress of Chemical and Process Engineering (CHISA2021 Virtually), on-line, March 13-18, 2021.

Effect of Rheological Properties on Couette-Taylor Flow with Axial Temperature Distribution
Kanta NAKAGAWA[†], Hayato MASUDA and Hiroyuki IYOTA
21st International Couette-Taylor Workshop (ICTW21), on-line, July 5-9, 2021.

The Study on the Viscoelastic Mechanism of Human Cultured Dermis and the Effects of Culture period on Viscoelasticity of Cultured Dermis
Miki YANAGISAWA[†] and Hiroshi KAWAKAMI
18th International Congress on Rheology, on-line, December 12-17, 2020.

Effect of Mesh Interlayer on Interlaminar Shear Strength in Unidirectional CFRP Laminates
Fumikazu KOBAYASHI[†], Hayato NAKATANI and Katsuhiko OSAKA
The 45th International Conference and Expo on Advanced Ceramics and Composites, Virtual Meeting, January 26-31, 2021. (poster).

Interlaminar Fracture Behaviour of UD-CFRP Laminates with Mesh Interlayer
Hayato NAKATANI, Fumikazu KOBAYASHI[†] and Katsuhiko OSAKA
The 45th International Conference and Expo on Advanced Ceramics and Composites, Virtual Meeting, January 26-31, 2021. (invited).

Fatigue Damage Accumulation in Notched Angle-plied CFRP Laminates with Mesh Interlayers
Yuika SAKAMOTO[†] and Hayato NAKATANI
SAMPE China 2021 International Conference, Beijing, China (hybrid event), July 6-9, 2021.

Applied Physics and Electronics

Launching Plasma Bullets from the Surface of a Dielectric Plate
Ryo MATOBA[†], Yudai NISHIMURA[†], Jun-Seok OH, Tatsuru SHIRAFUJI
13th International Symposium on Advanced Plasma Science and its Applications for Nitrides and Nanomaterials / 14th International Conference on Plasma-Nano Technology & Science, Mar. 7-11, 2021, Nagoya, Japan, Online (Oral)

Observation of APPJ Transfer through a Glass Plate - Effects of He-jet Nozzle Distance behind the Glass Plate Irradiated with APPJ
Yudai NISHIMURA[†], Ryo MATOBA[†], Jun-Seok OH, Tatsuru SHIRAFUJI
13th International Symposium on Advanced Plasma Science and its Applications for Nitrides and Nanomaterials / 14th International Conference on Plasma-Nano Technology & Science, Mar. 7-11, 2021, Nagoya, Japan, Online (Poster)

PEDOT Formation from EDOT using DBD Plasma of Ar and He Gases
Shintaro KITAGAWA[†], Ryoga KONISHI[†], Jun-Seok OH, Tatsuru SHIRAFUJI
13th International Symposium on Advanced Plasma Science and its Applications for Nitrides and Nanomaterials / 14th International Conference on Plasma-Nano Technology & Science, Mar. 7-11, 2021, Nagoya, Japan, Online (Poster)

Dependency of Bactericidal Effect in Oxygen-radical-Exposed E. Coli Suspension Containing L-Tryptophan on Its Concentration
Naoyuki IWATA, Kenji ISHIKAWA, Hiroshi HASHIZUME, Hiromasa TANAKA, Jun-Seok OH, Masafumi ITO, Masaru HORI
13th International Symposium on Advanced Plasma Science and its Applications for Nitrides and Nanomaterials / 14th International Conference on Plasma-Nano Technology & Science, Mar. 7-11, 2021, Nagoya, Japan, Online (Oral)

Non-thermal Atmospheric-pressure Plasma for Agricultural Application with Nitrate (NO_3^-) Rich Plasma Activated Water
Jun-Seok OH, Yusuke SASAKI[†], Kenji MAEDA[†], Tatsuru SHIRAFUJI
13th International Symposium on Advanced Plasma Science and its Applications for Nitrides and Nanomaterials / 14th International Conference on Plasma-Nano Technology & Science, Mar. 7-11, 2021, Nagoya, Japan, Online (Oral)

Visualization of Plasma Irradiation on the 3D Printed Mouse Model
Shunya HASHIMOTO[†], Kodai AOKI[†], Tatsuru SHIRAFUJI, Jun-Seok OH
13th International Symposium on Advanced Plasma Science and its Applications for Nitrides and Nanomaterials / 14th International Conference on Plasma-Nano Technology & Science, Mar. 7-11, 2021, Nagoya, Japan, Online (Oral)

Delivery of Plasma Generated Reactive Oxygen and Nitrogen Species (RONS) into Biological Target
Jun-Seok OH, Hideo FUKUHARA, Endre J. SZILI
47th IOP Plasma Physics Conference, Apr. 6-9, 2021, Online (Invited)

Effect of Non-thermal Plasma Irradiation on the Biological Targets; Model Tissue, Culture Dermis, and Live Mouse
Jun-Seok OH, Endre SZILI, Hideo FUKUHARA, Rob SHORT, Akimitsu HATTA, Masafumi ITO, Keiji INOUE
8th International Conference on Plasma Medicine, Aug. 3-6, 2021, Online (Invited)

Contactless Plasma Jet Treatment of a Cancer Tumour
Endre SZILI, Jun-Seok OH, Keiji INOUE, Rob SHORT, Hideo FUKUHARA
8th International Conference on Plasma Medicine, Aug. 3-6, 2021, Online (Invited)

Report on the 1st International Meeting on Plasma Cosmetic Science (IMPCS1)
Jean-Michel POUVESLE, Vittorio COLOMBO, David GRAVES, Catherine GRILLON, Ihn HAN, Jun-Seok OH, Endre SZILI, Thomas VON WOEDTKE, Eric ROBERT
8th International Conference on Plasma Medicine, Aug. 3-6, 2021, Online (Invited)

Visualization of Plasma Treatment on 3D Printed Bone Defect Model
Kodai AOKI[†], Shunya HASHIMOTO[†], Akiyoshi SHIMATANI[†], Hiromitsu TOYODA, Hiroaki NAKAMURA, Tatsuru SHIRAFUJI, Jun-Seok OH
8th International Conference on Plasma Medicine, Aug. 3-6, 2021, Online (Oral)

Spatiotemporal Behavior of Surface Temperature on the Mouse Skin during Plasma Irradiation
Shunya HASHIMOTO[†], Kodai AOKI[†], Tatsuru SHIRAFUJI, Hideo FUKUHARA, Chiaki KAWADA, Keiji INOUE, Masayuki TSUDA, Endre J. SZILI, Jun-Seok OH
8th International Conference on Plasma Medicine, Aug. 3-6, 2021, Online (Oral)

Investigating the Interactions of Plasma with DNA: Towards Safer Plasma Jet Treatments
Nishtha GAUR, Endre SZILI, Hirofumi KURITA, Saki MIYACHIKA, Jun-Seok OH, Masafumi ITO, Akira MIZUNO, Bhagirath GHIMIRE, Sarah ALLINSON, Allison COWIN, Robert SHORT
8th International Conference on Plasma Medicine, Aug. 3-6, 2021, Online (Oral)

Importance of Organic Compounds on Bactericidal Activity of Radical-activated Phenylalanine Solution
Naoyuki IWATA, Hiroshi HASHIZUME, Jun-Seok OH, Masaru HORI, Masafumi ITO
8th International Conference on Plasma Medicine, Aug. 3-6, 2021, Online (Oral)

Hydrophilic Treatments of a 3D-printed Bone-regeneration PLA Scaffold Using Propagation of Plasma Bullets
Tatsuru SHIRAFUJI
The 8th East Asia Joint Symposium on Plasma and Electrostatics Technologies for Environmental Applications, Oct. 18-21, 2021, Xi'an, China / Online (Invited)

Electrical and Information Engineering

Spin Transport Property in Thermally-Evaporated Pigment-Red Films by Using a Dynamical Spin Injection Method
K. NISHIDA[†], Y. TEKI (Graduate School of Science, OCU), and E. SHIKOH
The 65th Annual Conference on Magnetism and Magnetic Materials, (online), November 2-6, 2020 (poster)

Spin Injection Into Vanadium Dioxide Films From a Typical Ferromagnetic Metal, Across the Metal-Insulator Transition of the Vanadium Dioxide Films
K. TAMURA[†], T. KANKI (Osaka Univ.), S. SHIRAI[†], H. TANAKA (Osaka Univ.), Y. TEKI (Graduate School of Science, OCU) and E. SHIKOH
The 65th Annual Conference on Magnetism and Magnetic Materials, (online), November 2-6, 2020 (poster)

Online multi-agent supervisory control for warehouse automation: heterogeneous payloads
M. KASAHARA[†], Kai CAI
The 29th Mediterranean Conference on Control and Automation, (online), June 22-25, 2021 (oral)

Online multi-agent supervisory control for warehouse automation: prioritized tasks
M. KASAHARA[†], Kai CAI
The 17th International Conference on Automation Science and Engineering, (online), August 23-27, 2021 (oral)

Aberrant membrane structures in hypervesiculating *Escherichia coli* strain Δ*mlaE*Δ*nlpI* visualized by quick-freeze deep-etch electron microscopy
Yoshihiro OJIMA, Tomomi SAWABE[†], Mao NAKAGAWA[†], Yuhei O. TAHARA, Makoto MIYATA, Masayuki AZUMA
EMBO Workshop, P-6, Tsukuba, Japan, November 23-26, 2021(poster)

Trace and elemental imaging X-ray fluorescence analysis in the laboratory
K. TSUJI, K. AKIOKA, T. MATSUYAMA
Asian Conference on Analytical Sciences 2020 (ASIANALYSIS 2020), online, 16-18 October 2021. (invited)

Introduction to X-ray Fluorescence
K. TSUJI
1st International Summer School on TXRF, online, 20-24 September 2021. (invited)

Workshop Instructor on "Micro XRF"
K. TSUJI
70th Annual Conference on Applications of X-ray Analysis Denver X-ray Conference, online, 2-6 August 2021. (invited)

Workshop Instructor on "Trace Analysis"
K. TSUJI
70th Annual Conference on Applications of X-ray Analysis Denver X-ray Conference, online, 2-6 August 2021. (invited)

Exploring possibilities and drawbacks in the analysis of Pb loaded reference samples by using TXRF spectrometers
P. CIRELLI, F. BILO, A. ZACCO, K. TSUJI, T. MATSUYAMA, G. SIVIERO, L. PISANI, D. EICHERT, L. E. DEPERO, L. BORGESE
Virtual Conference in X-ray Spectrometry EXSA'S 2021 online event, 21-24 June 2021. (poster)

Sample preparation technique for total reflection X-ray fluorescence analysis using freeze drying method
T. MATSUYAMA, Y. TANAKA[†], M. NAKAE[†], K. TSUJI
70th Annual Conference on Applications of X-ray Analysis Denver X-ray Conference, online, 2-6 August 2021. (oral)

Investigation of the transmission properties of a polycapillary half-lens and their effect on quantification for confocal μXRF
M. IRO, D. INGERLE, K. TSUJI, S. HAMPEL, U. FITTSCHEN, C. STRELI,
70th Annual Conference on Applications of X-ray Analysis Denver X-ray Conference, online, 2-6 August 2021. (poster)

Fundamental study for elemental identification method by X-ray absorption imaging using a secondary target
M. NAKAE[†], T. MATSUYAMA, M. MURAKAMI, Y. YOSHIDA, M. MACHIDA, A. UEDA, T. SASAKI, K. TSUJI
70th Annual Conference on Applications of X-ray Analysis Denver X-ray Conference, online, 2-6 August 2021. (poster)

Total reflection X-ray fluorescence analysis of aerosol particles by simple dissolution of particle collection filter

H. YAMAGUCHI[†], T. MATSUYAMA, K. TSUJI
70th Annual Conference on Applications of X-ray Analysis Denver X-ray Conference, online, 2-6 August 2021. (poster)

Ultra-hydrophilic substrate modified by an atmospheric pressure plasma for TXRF analysis
Y. TANAKA[†], T. MATSUYAMA, J. S. OH, K. TSUJI
70th Annual Conference on Applications of X-ray Analysis Denver X-ray Conference, online, 2-6 August 2021. (poster)

Depth Profiling of Cu in the Deteriorated Polyethylene Materials Using Confocal X-Ray Fluorescence Analysis
T. FUCHITA[†], T. MATSUYAMA, Y. TAKIMOTO, H. HONMA, K. TSUJI
70th Annual Conference on Applications of X-ray Analysis Denver X-ray Conference, online, 2-6 August 2021. (poster)

Photoresponsive Diarylethene Molecular Crystals for Photoactuators
Seiya KOBATAKE
2020 MRS Fall Meeting (Virtual), November 27-December 4, 2020 (Invited)

Photochromic Diarylethene Crystals for Photoresponsive Actuators
Seiya KOBATAKE
The International Chemical Congress of Pacific Basin Societies 2021 (Pacifichem 2021) (Virtual), December 16-21, 2021 (Invited)

Photochromic Molecular Crystals: From Color Change to Photoactuator
Seiya KOBATAKE
The International Chemical Congress of Pacific Basin Societies 2021 (Pacifichem 2021) (Virtual), December 16-21, 2021 (Invited)

Recent Progress in Photomechanical Diarylethene Crystals
Daichi KITAGAWA, Seiya KOBATAKE
The International Chemical Congress of Pacific Basin Societies 2021 (Pacifichem 2021) (Virtual), December 16-21, 2021 (Invited)

Photoinduced Birefringence Change in Photoresponsive Organic Crystals
Kohei MORIMOTO[†], Daichi KITAGAWA, Seiya KOBATAKE
The International Chemical Congress of Pacific Basin Societies 2021 (Pacifichem 2021) (Virtual), December 16-21, 2021 (Poster)

Enhancement of Coloring under Ultraviolet Irradiation in Photochromic Diarylbenzenes
Shota HAMATANI[†], Daichi KITAGAWA, Seiya KOBATAKE
The International Chemical Congress of Pacific Basin Societies 2021 (Pacifichem 2021) (Virtual), December 16-21, 2021 (Poster)

Heterogeneous Catalysis of Polynuclear Cyano-Bridged Metal Complexes
Yusuke YAMADA
International Conference on Materials Chemistry and Catalysis, Tezpur (on-line), India, March 4, 2021 (invited)

Coordination Polymers for Detection and Decomposition of Organophosphates
Yusuke YAMADA
International Conference on Materials Science and Engineering 2021, Brisbane (on-line), Australia, October 11-14, 2021 (invited)

Catalytic Stability of Fe^{III}[Co^{III}(CN)$_6$] Enhanced by Doping Divalent Metal Ions for Hydrolysis of Organophosphates
Yusuke SEKI[†], Hiroyasu TABE, Yusuke YAMADA
18th Japan-Korea Symposium on Catalysis, Osaka (on-line), Japan, November 23-25, 2021

Differentiating the Rate Capabilities of Lithium-Nickel-Manganese Oxide, Li[Ni$_{1/2}$Mn$_{3/2}$]O$_4$, Insertion Materials and Electrodes Using Diluted Electrode Methods
Kingo ARIYOSHI, Shumpei MASUDA[†], and Jun SUGAWA[†]
Pacific Rim Meeting on Electrochemical and Solid-State Science 2020 (PRiME2020), Hawaii, October 4-9, 2020

Determination of Diffusion Coefficient of Li$^+$ Ions in Porous Electrodes from Rate Capability Tests
Rikuya SUZUKI[†], Kingo ARIYOSHI
Pacific Rim Meeting on Electrochemical and Solid-State Science 2020 (PRiME2020), Hawaii, October 4-9, 2020 (Poster)

Solid-State Diffusion Coefficient of Li Ions in Li[Ni$_{1/2}$Mn$_{3/2}$]O$_4$ Determined By the Diluted Electrode Method
Jun SUGAWA[†], Shumpei MASUDA[†], Kingo ARIYOSHI
Pacific Rim Meeting on Electrochemical and Solid-State Science 2020 (PRiME2020), Hawaii, October 4-9, 2020 (Poster)

Enhanced Decomposition of Toxic Pollutants by Underwater Pulsed Discharge in the Presence of Hydrogen Peroxide or Microbubbles
Risako MATSUURA, Noritsugu KOMETANI, Hideo HORIBE and Tatsuru SHIRAFUJI
13th International Symposium on Advanced Plasma Science and its Applications for Nitrides and Nanomaterials (ISPlasma2021), Virtual meeting, March 8-11, 2021

Debondable Adhesives without Decomposition of Cured Adhesive Polymers
Eriko SATO, Seidai OKADA[†], Keita KATAGI[†]
13th European Adhesion Conference (EURADH 2021), Virtual Meeting, October 11-14, 2021

Phase Behavior of Coumarin Containing Polymers and Gels in Non-Hydrogen Bonding Organic Solvents
Eriko SATO
The International Chemical Congress of Pacific Basin Societies 2021 (Pacifichem 2021), Virtual Meeting, December 16-21, 2021 (invited)

High Performance Dismantlable Adhesive Materials Based on Controlled Polymer Reactions
Eriko SATO
The International Chemical Congress of Pacific Basin Societies 2021 (Pacifichem 2021), Virtual Meeting, December 16-21, 2021

Effects of Polymorph Composition of Polypropylene on Heterogeneous Nucleation of L-Alanine
Koichi IGARASHI and Masayoshi TSUSAKI[†]
The 5th Asian Crystallization Technology Symposium (ACTS2021) (Virtual), May 26-28, 2021

Highly Efficient Chiral Resolution of DL-Glutamic Acid by a Preferential Crystallization Combined with an Enzymatic Racemization Reaction
Koichi IGARASHI and Tomono FUJIMURA
The 5th Asian Crystallization Technology Symposium (ACTS2021) (Virtual), May 26-28, 2021